Spectral Image Quality in MARS Scanners

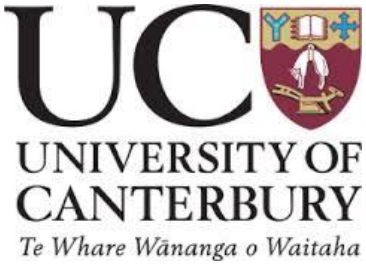

Mohammad Rayhan Uddin
School of Physical and Chemical Sciences
University of Canterbury

A thesis submitted for the degree of
Doctor of Philosophy in Medical Physics
September 18, 2019

Abstract

This thesis reports on contributions to the development of the MARS spectral CT scanner that incorporates the energy resolving photon counting Medipix3RX detector. The key novel feature of this scanner is that it uses the energy information to identify and quantify different materials simultaneously.

The spectral and spatial performance of MARS spectral CT scanners is affected by the various factors. A spectral image library was created using distorted images to display spatial image deteriorations. This work is based on exploiting the vast capacity of the human visual system to process and interpret images to aid investigations into the relationship between geometric information and spectral information and consequent implications in material reconstruction. An important concept investigated in this thesis is that distortion in the spatial dimensions of spectral CT data induces distortion in the energy dimensions.

To reduce the impact of spatial distortion on the reconstructed images, I was then involved in measuring the geometric offset parameters and calibrating the scanner correspondingly. Together with others, I developed a comprehensive geometric calibration method that enables measuring the various geometric parameters from the projection images at the accuracy of the ten-micron level.

Experimental studies in chapter 3, have investigated the inter-scan and intra-scan variability of measured linear attenuation in repeated scans and using several composite and single materials. Chapter 7, studies the variability of photon counts in multiple energy counters. These measurements provide useful insights into the source of variation in the energy information content of MARS spectral CT images and indicate potential areas where future improvements in performance may be made.

Academic contributions

During the course of my doctoral study, I have contributed to the development of the MARS scanner. I have also contributed to the following publications and other forms of dissemination.

- **Accomplishments**

Conferences

1. **M. Rayhan Uddin**, Marzieh Anjomrouz, Raj Kumar Panta, Brian P.Goulter, Stephen T Bell, Michael Walsh, Niels de Ruiter, Anthony P.H. Butler, Philip H. Butler Image., Artifact Library for MARS Spectral CT, Presented to New Zealand Institute of Physics (NZIP) Conference, 2017.
2. **M. Rayhan Uddin**, Marzieh Anjomrouz, Raj Kumar Panta, Brian P.Goulter, Stephen T Bell, Michael Walsh, Niels de Ruiter, Anthony P.H. Butler, Philip H. Butler., An improved geometrical calibration method for MARS spectral scanner, Presented to Physics and Astronomy annual Conference, 2017.
3. **M. Rayhan Uddin** Improving spectral image quality by optimizing geometrical calibration Presented to Physics and Astronomy three minute thesis competition.

MARS team presentations

1. **M. Rayhan Uddin.,** Improving spectral image quality by optimizing geometrical calibration, Presented to University of Canterbury Physics and Astronomy three minute thesis competition
2. **M. Rayhan Uddin.,** Developing a fine geometrical calibration method for MARS scanner, Presented to MARS research group seminar, (13 Sep 2017)

Under preparation

I have been preparing a report on the following task to present in different seminars and conference.

1. A workflow of the spectral image library using MARS scanner.
2. Developing a geometric calibration method for MARS scanner
3. Characterizing the measurement variability of MARS scanner
4. Characterizing the stability of the photon counting detector

MARS text book

I contributed to the different section in following chapters of MARS textbook, Physics volume, October 2017

1. Introduction to MARS geometry.
2. Different coordinate system of MARS scanner.
3. Geometric calibration for MARS spectral CT.

Technical reports

I contributed to three technical reports for unpacking inspection of MARS-15

1. Unpacking inspection of MARS-15
2. Camera assembly and troubleshooting for MARS-15
3. Upgrading MARS-15 to the standard level

Co-author of different papers

1. Aamir et al "Bone and joint imaging with MARS scanners" submitted to 5th Workshop on Medical Applications of Spectroscopic X-ray Detectors to be held at CERN on 13-16 May 2019.

2. Maya Rajeswari Amma et al “Assessment of metal implant induced artefacts using photon counting spectral CT” Proc.SPIE11113, Developmets in X-ray Tomography XII, 10 September 2019.

3. Ali Atharifard et al "Pulse Pileup Models for Spectral X-ray Imaging" submitted to 20th international workshop on radiation imaging detectors.

4. Lieza Vanden Broeke et al "Calibrating MARS Cameras using X-ray Fluorescence" submitted to 20th international workshop on radiation imaging detectors.

5. Anthony Butler et al " First living human images from a MARS photon-counting 8-energy CT" submitted to 2018 IEEE nuclear science symposium and medical imaging conference in Sydney, Australia.

6. Mahdieh Moghiseh et al "Spectral CT of Cancer Cells with Nano-Particles: In-Vitro and In In-Vivo Results" accepted to RSNA 104th Scientific Assembly and Annual Meeting, November 25–December 30, 2018

7. Steven P Gieseg and MARS team collaboration "Identifying indicators of unstable atherosclerotic plaque using MARS spectral imaging" submitted to 2018 IEEE nuclear science symposium and medical imaging conference in Sydney, Australia.

8. Mahdieh Moghiseh et al and MARS team collaboration "Cancer imaging with nanoparticles using MARS spectral scanner" submitted to 2018 IEEE nuclear science symposium and medical imaging conference in Sydney, Australia.

9. Fatemah Asghariomabad et al and MARS team collaboration " Intrinsic respiratory gating for MARS imaging" submitted to 2018 IEEE nuclear science symposium and medical imaging conference in Sydney, Australia.

10. Emily Searle and MARS collaboration"Distingushing iron and calcium using MARS spectral CT" 2018 IEEE nuclear science symposium and medical imaging conference in Sydney, Australia.

11. CD Lowe and MARS Collaboration "Differentiation of Tuberculosis infected and healthy pulmonary tissue using MARS spectral molecular imaging" 2018 IEEE nuclear science symposium and medical imaging conference in Sydney, Australia.

Awards and achievements

1. MARS PhD scholarship from research grant E6302
2. Awarded second prize for University of Canterbury three minute (3MT) PhD thesis competition, 2017.
3. Part-time Scientist MARS Bioimaging Ltd: Systems and Applications Development.

Attending MedTech CoREs doctoral training

I attended two workshops for doctoral training program.

1. **Instrumentation and Design** held on Mon 5 March-Fri 9 March 2018, Auckland Bioengineering Institute, 70 Symonds Street, Auckland.
2. **Computational Physiology** held on Mon 19 March-Fri 23 March 2018, Auckland Bioengineering Institute, 70 Symonds Street, Auckland.

Acknowledgements

Firstly, I would like to express my sincere gratitude to my senior supervisor Prof Phil Butler for supervising my Ph.D study and selecting me to contribute to the MARS project. His guidance and motivation always inspired me all the time of research and writing of this thesis. I am also thankful to my co-supervisor Prof Anthony Butler for his valuable advice and support during my doctoral study. I am also grateful to them for awarding me the doctoral scholarship from MARS bioimaging Ltd.

I would like to thank to Dr Marzieh Anjomrouz for fruitful discussions and corrections on my research proposal and geometric calibration. I also like to convey my thanks to Dr Stephen Bell, Dr Chris Bateman, Dr Muhammad Shamshad, Dr Aamir Raja, Dr Raj Panta, Dr Peter Renaud, Assoc Prof Nigel Anderson, Assoc Prof Steven Gieseg, Dr Niels de Ruiter, Dr Mahdieh Moghiseh, Dr Joe Healy, Dr Ali Atharifard for their interesting discussions.

Thank you to Mr. Brian Goulter for his help to produce the bill of materials and assembly and mounting multi-chip camera. Thank you to Dr Lieza Vanden Brooke for proofreading my thesis. I also thankful to all factory members, in particular, Dr Hannah Prebble, Nerayda Duncan, Jereena Sheeja, Fatemeh Ashgariomobad, Dr Stuart Lansley, Srinidhi Bheesette, Dr Steven Alexander, Dr Mike Walsh, Dr Robert M.N. Doesburg.

I am also grateful to the School of Physical and Chemical Sciences for giving me a resourceful environment. Thank you to Associate Professor Jenni Adams, Prof Mike Reid, Dr Steven Marsh, Dr Orlon Petterson. I also would like to thank Rosalie Reilly, Xuefeng Liu, Sharlene Wilson, Sam Gurney and Mr. Peter Hilton for facilitating my research throughout my Ph.D. study.

Finally, I would like to express my respect and many thanks to my parents and my wife for their endless support during my Ph.D. journey

Dedicated to Professor Philip Butler and MARS team for your commitment, inner voice, and encouragement

Table of contents

Table of Figures

1 Introduction

1.1 Thesis Introduction

This thesis reports on the development of the MARS spectral CT scanner, including: (1) producing a spectral image library; (2) investigating the measurement variation of the x-ray signal through different composite and single materials; (3) developing a new geometric calibration method to reduce spectral image distortion; and (4) Investigating energy domain measurements in repeated scans

MARS is a quantitative color x-ray imaging modality that incorporates the Medipix3RX photon counting detector, developed by the Medipix3 collaboration hosted by the European Organization for Nuclear Research (CERN) [1]. A detailed description of the MARS spectral imaging system is discussed in chapter 2. For diagnostic purposes, there are several imaging modalities such as radiographs (plain film), conventional tomography (CT), ultrasound (US), magnetic resonance imaging (MRI) and are used. Each of imaging modalities have some drawbacks.

Plain film radiographs produces 2D black and white images that are convenient to see bone fracture, however, it does not provide detailed images of the body [2]. Magnetic resonance imaging (MRI) and conventional CT scanners can overcome this problem, but they still have some limitations. MRI is particularly useful for scanning and detection of the abnormalities in soft tissue [3]. Despite MRI having a (2 to 3 mm) spatial resolution to image soft tissue, it does not provide quantitative tissue composition at the histological level. Conventional CT scanners measure the attenuated signal over the entire x-ray spectrum, therefore all materials produce same CT number at a certain concentration. As a result of this it is not possible to separate the materials from each other [4]. Another disadvantage of conventional CT scanner is that it produces a high dose due to use of energy integrating detector [5]

A key benefit of the MARS scanner is improved spatial resolution. The spatial resolution of the MARS scanner is 80 μm; that is six times higher than conventional CT scanner [6]. Due the use of multiple energy bins MARS scanner has better energy resolution than dual energy CT. It will provide quantitative tissue composition, not just the size, shape and location of the anatomy. The MARS scanner can measure the attenuated signal of different materials at different energy bins, and therefore it provides a different CT number for all of the materials simultaneously in a single exposure. It is also able to provide quantitative measurements equivalently in milligrams per milliliter of each material. More detailed discussion of the imaging characteristics and potential applications of MARS scanner are discussed in chapter 2.

The MARS scanner has the ability to collect complete spectroscopic energy information at every location in each image volume, therefore, it is a more informative imaging system than

other conventional imaging modalities. In this thesis, I developed a spectral image library for the MARS scanner. This will allow the user to identify the spatial image error of the MARS scanner.

Initially, a framework was developed to create a spectral image library using the images of multi-contrast phantom. In this image library, I show how the spectral signal is being degraded under the perturbation of multiple geometric parameters. I also observe the impact of the geometric information on the material reconstruction.

The spatial and spectral resolution of the MARS scanner is improved by characterizing the measurement variability. At the beginning of this work I investigated the sources of instabilities in the MARS scanner that have a significant impact on the reconstructed images. The motivation for doing this was to evaluate the inter-scan and intra-scan measurement variation of the spectral signal obtained from different materials. Measurement variations occur because of different sources of instabilities that originate from the geometric misalignment, inter-pixel variation, threshold drifting etc.

The spatial resolution of the MARS scanner is sensitive to geometrical alignment parameters that are related to the gantry, the x-ray source, and the detector. Geometric misalignment causes artifacts in the reconstructed images, which can obscure disease diagnosis. In this thesis, I report on a geometric calibration method which allows us to measure the offset of different geometrical parameters, and can then be corrected in the image reconstruction. The key feature of this method is to systematically measure the geometrical parameters, as well as speeding up the processing time.

Additionally, I studied energy domain measurements to investigate the threshold drifting in existing energy calibration method. Relative count rate capability of each charge summing counter with respect to arbitration counter was measured in this regard.

During the course of my PhD, I was involved in the systems and applications development group to make the bill of materials for different scanner components. As part of this group I also assembled different multi-chip cameras. I was involved in documenting the procedures for the unpacking, and the inspection of the MARS-15 scanner that was returned to the lab after suffering damage. A list of all modifications, at both hardware and software level, were created.

To share my knowledge in the wider science community, I presented my work at several seminars and workshops. My contribution to the MARS project is listed in my Academic Contributions section.

1.2 Thesis goal

The main goal of this thesis was to contribute to the development of the MARS spectral CT system. To achieve this goal, I have completed several inter-related studies that focus on: image library, measurement variability, calibration, and stability of the Medipix3RX detector. This work is motivated to provide knowledge and insights for improving material detection in MARS spectral CT.

1.3 Scope of the study

The MARS group is a world leader in spectral x-ray technology for molecular imaging of models of disease. The MARS project is a collaborative effort between many organizations around the world. The project is led jointly by the University of Canterbury, including the University of Otago (UOC) and Lincoln University. A company called MARS Bioimaging Ltd (MBI) was formed to productize the MARS technology. MBI has been building small animal spectral scanners since 2007. Several MARS scanner are being used for research purposes in different parts of the world, including Mayo Clinic (Rochester, USA); Notre Dame (ND) Integrated Imaging Facility (USA); JINR Dubna (Russia). In 2018, a MARS human scanner was completed and used to scan the body parts of a living human [7, 8].

1.4 Thesis outline

I have structured this thesis in the following way:

Chapter 1 provides an introduction to the thesis as a whole: goals of this Ph.D, scope of this study, advantages of spectral CT over conventional imaging modalities, and a brief description what has been improved during this study and thesis outline.

Chapter 2 provides the background information to the MARS imaging chain. It provides details of MARS spectral imaging, overview of the photon counting Medipix detector, significance and working principle of photon counting detector, different operating mode of Medipix3RX, basic concepts of MARS spectral CT imaging, the different important modules of MARS imaging chain, imaging characteristics, different image quality parameters, and potential applications of MARS scanners.

Chapter 3 reports on a pilot study to investigate the measurement variation in spectral signal from different materials in different MARS scanners. Inter-scan and intra-scan measurement variation of the mass attenuated signal of different materials was evaluated. This chapter focuses on how different instabilities such as geometric misalignment, inter-pixel variation, and threshold drifting produce noise that causes measurement variation in spectral CT. The Bland-Altman method is discussed to measure the proportional bias in measurement.

Chapter 4 provides the information on the scanner geometry. It discusses the relationship between the gantry, x-ray source, and camera. Different axis and coordinate systems related to the geometry of the beam, and how ray passes through the voxel are discussed. The algebraic reconstruction technique also discussed in this chapter. The significance of the geometric parameters in future polychromatic reconstruction is discussed in detail.

Chapter 5 describes the work of making the spectral image library using the image of the multi-contrast phantom. The impact of geometric perturbation on the reconstructed images and how they degrade the spectral signal in different materials at different energy bins is discussed. The impact of geometric information and spectral information, and implications for material reconstruction are discussed. This chapter also focuses on image difference and subtraction from the normal and distorted images. Different anatomical image planes (axial, sagittal and coronal) also illustrate and display the level of image distortion at the different slices and for each energy bin.

Chapter 6 includes a method of geometric calibration that discusses the procedure for measurements of calibration offsets of a MARS scanner.

Chapter 7 provides energy threshold stability measurements of a MARS scanner. Relative count performance of different charge summing counter was evaluated with respect to the arbitration counter to investigate the threshold drifting.

Chapter 8 provides a discussion and summary of the material presented in the experimental chapters in relation to their application to improving spectral CT performance.

2 The MARS scanner

2.1 Introduction

This chapter provides a brief overview of the physical features of the MARS spectral scanner. Section 2.2 outlines the MARS scanner and the Medipix photon counting detector. It includes the significance of the photon counting detectors, the photon counting mechanism, and operation of the modes of the Medipix detector. Section 2.3 reports on the fundamental principle of spectral imaging. Section 2.4 describes the MARS imaging chain and my contribution to it. Sections 2.5 and 2.7 provide imaging characteristics and potential applications of the MARS spectral scanner.

2.2 MARS imaging with the Medipix detector

The detector is a crucial part of computed tomography (CT) systems. The MARS scanner incorporates the state-of-the-art Medipix3RX photon counting detector. The Medipix3RX allows the user to count the number of x-ray photons in each of the energy ranges that passed through materials of the object.

2.2.1 Significance of photon counting detectors

Conventional CT scanners contain energy integrating detectors that absorb the x-rays and convert them into visible light. Such detectors add the x-ray flux over a certain period of time, with a weighting factor proportional to the energy of the absorbed x-ray quanta. As a consequence, the detector does not have energy resolution capabilities. Energy integrating detectors are not able to separate different materials from each other when electron density of the two materials is similar or which they are in fluid at unknown concentrations [9].

Photon counting detectors, on the other hand, are able to measure the energy of individual photons, and by using information about x-ray absorption at different energies, can discriminate several materials simultaneously [10]. Another advantage of photon counting detectors is the reduced x-ray dose to the patient. The reason for this is because energy information is extracted from each individual photon in discrete events. This means there is no background noise in low intensity exposure [9].Photon counting detectors are often use for K-edge imaging [11].

2.2.2 Photon counting mechanism

The detector investigated in this thesis is the Medipix3RX photon counting detector. The Medipix3RX detector converts x-ray information to electrical charge, which then is converted into a digitized number. When radiation is incident on a semiconductor material electron-hole pairs are created inside the semiconductor. Figure 2.2 shows a schematic diagram of the Medipix detector that illustrates this mechanism. The interaction probability between transmitted x-ray spectra, object, and the sensor layer depend on the incident photon and the energy. The electrons and holes drift towards the electrodes via an externally applied bias voltage. This seperation produces an electrical signal. The height of the signal is proportional to the amount of charge reaching the pixel electronics and corresponds to the energy released by the ionizing particle in the sensor. The signal is then amplified by a preamplifier to convert it into a measurable range. If the incoming signal exceeds the lower energy threshold, a counter in the digital part of the chip is incremented in this pixel as shown in Figure 2.2(c) [12, 13]. The Medipix detector is operated in single pixel mode (SPM) or charge summing mode (CSM). The latest version of Medipix detectors have eight counters including the three (SPM), four (CSM) and one arbitation counter. The CSM is a mode of operation designed to correct for the effects of charge sharing [14].

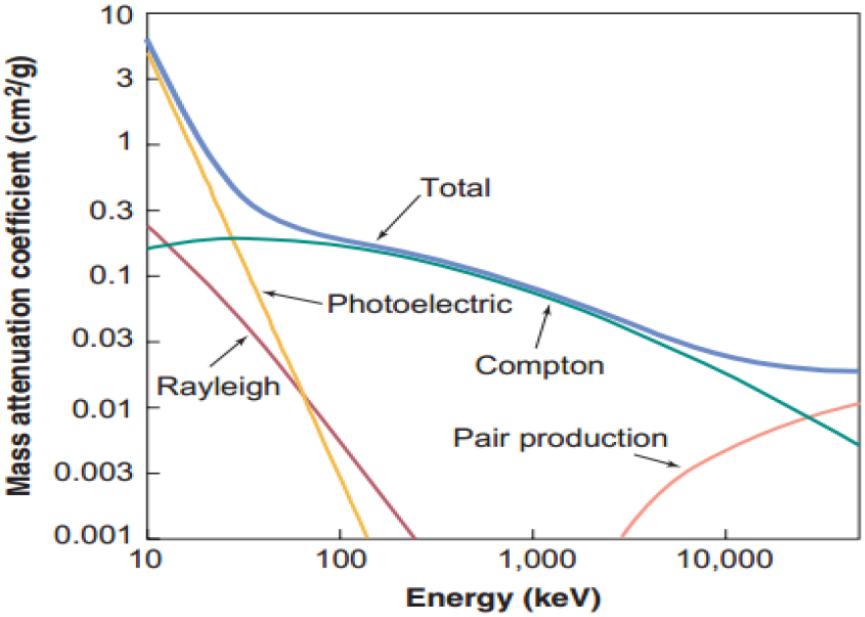

Figure 2.1 Graphical representation of contributions from different types of photon interactions with soft tissue as a function of photon energy. The Compton scattering is a predominant interaction over a wide range of photon energies. Image retrieved from Bushberg [15].

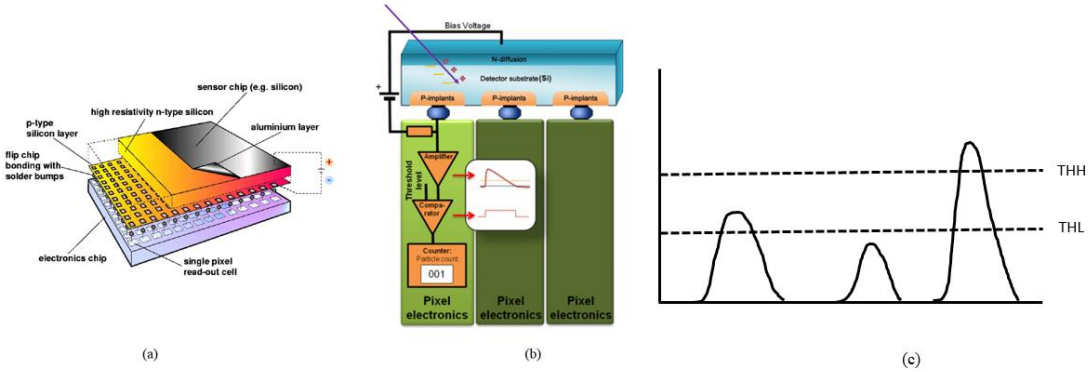

Figure 2.2 (a) A schematic view of photon counting hybrid detector. (b)The radiation generates electron-hole pairs (charge) in the sensor. The charge is collected to the appropriate pixel, amplified and compared with a pre-set comparator level (energy threshold). (c) The counter is increased if the detected pulse is above the lower energy threshold (THL) [12].

2.3 Concept of MARS spectral imaging

MARS spectral imaging provides spectral CT data. This is obtained by counting the number of photons in multiple energy bands, and is often referred to as multi-energy CT. It is this splitting of the x-ray beam into multiple energy bins that gives rise to the term color x-ray imaging. The ability to count individual photons is provided by the Medipix detector (As was discussed in section 2.2). Due to the use of an energy resolving photon counting detector, the MARS scanner can discriminate between and quantify various materials in an object. The concept of MARS spectral imaging is explained in Figure 2.3. The MARS scanner achieves energy dependent information by exploiting the features of x-ray interactions. The MARS scanner produces 3D color images by measuring the x-ray attenuation at different energy bins over the entire x-ray spectrum. Once different materials have been recognized and located, different colors are assigned to each of them, to aid visualization of these materials in 3D images [16].

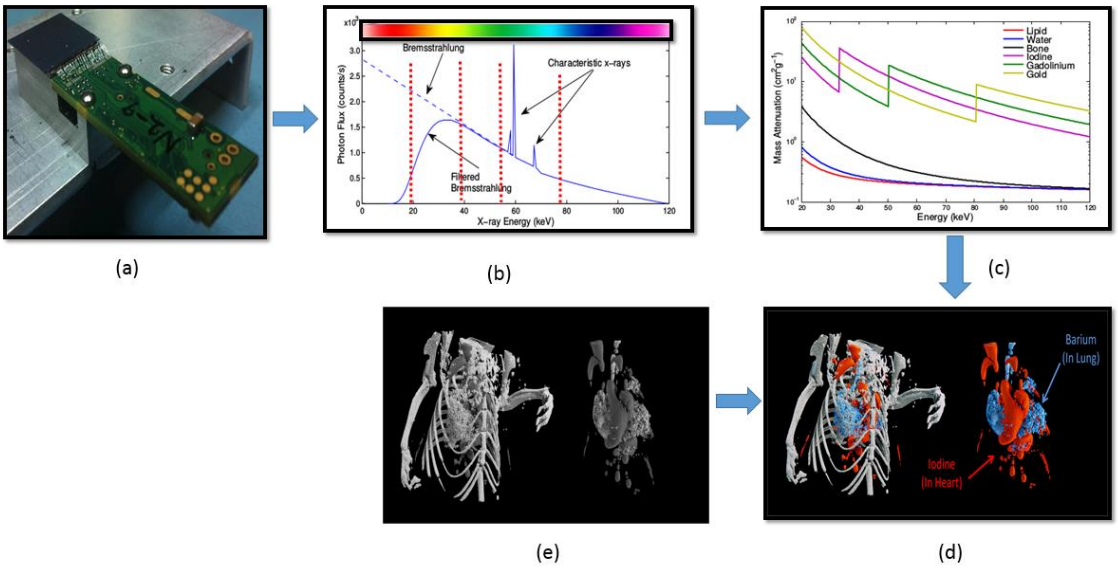

Figure 2.3 Medipix3RX color detector (a) that is bump bonded with the sensor layer to produce an electron-hole pair by interacting with incident radiation and the sensor layer. The charge is then collected to pixel electrodes and via bump bonds conducted to the CMOS electronics layer. Each pixel has a user-defined energy threshold. (b) Those thresholds can be divided in up to eight individual energy thresholds over the entire x-ray spectrum. The red dotted line represents the energy threshold of the spectroscopic charge summing mode in an x-ray spectrum. (c) Due to the spectroscopic nature, it can measure attenuation difference of different materials at different energy threshold and (d) able to identify and quantify different materials in a different color *[17]*. Image courtesy: Christopher Bateman, Alex Chernoglazov and Lieza Vanden Brooke.

2.4 The MARS imaging chain

The MARS imaging chain consists of several systems and sub-systems. The main components of the MARS imaging chain are: the MARS scanner that incorporates the MARS camera, the MARS workstation, and the MARS vision workstation. A brief description of each system, along with my contribution, is presented in the sections below.

2.4.1 Scanner

The MARS scanner is equipped with an x-ray source and camera that can operate at the diagnostic energy range of 20 keV to 120 keV. Figure 2.4 illustrate the parts of a MARS scanner. The scanning unit consists of a rotating gantry that holds the x-ray source and camera. The rotating gantry is pushed by way of a computer-managed stepper motor. A test sample, with maximum field of view of 100 mm diameter and 270 mm length, is positioned in the center and can be moved along the rotation axis. The operation of the scanner after sample insertion is by a Graphical User Interface (GUI). The camera and the source are placed on the gantry on opposite sides. The scanner is designed with the adjustable source to detector distance (SOD) and axis to detector distance (ADD) so that the user can easily alter the magnification [18].

My contribution to this part of the imaging chain was to develop a geometric calibration method for the MARS scanner (it is explained in chapter 6). To this extent, I measured different geometric offset parameters of different scanner components.

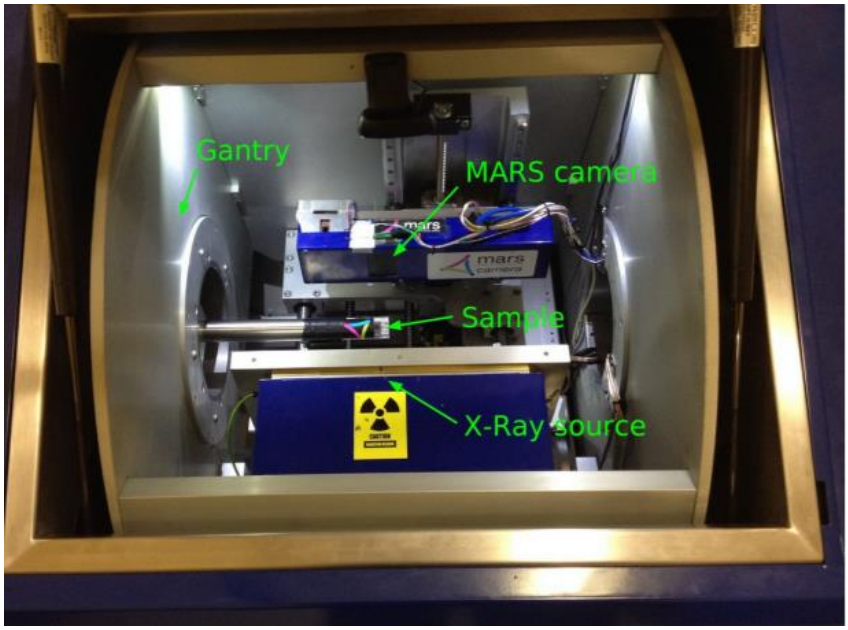

Figure 2.4 The interior part of the MARS scanner (gantry, x-ray source, MARS camera, and sample holder). The predominant geometric parameters are interrelated with the orientation of x-ray source, camera, sample position, and gantry *[19]*. Image courtesy: MARS Bioimaging.

2.4.2 Camera

A MARS camera is equipped with several of Medipix3RX detector chips that are located in the detector mounting assembly. Apart from the chip assembly, there are some other electronic components such as high voltage board, readout board, ASIC circuit, and transition board. The MARS camera can be translated both radially and tangentially to control the object to detector distance and to cover the span of the specimen with a narrow cone beam. Figure 2.5 and Figure 2.6 show the interior of three chip and seven chip MARS camera. I produced the bill of materials of different MARS cameras and assembled a multi-chip MARS camera and calculated the geometric offset to measure the inter-chip gap and chip skewness.

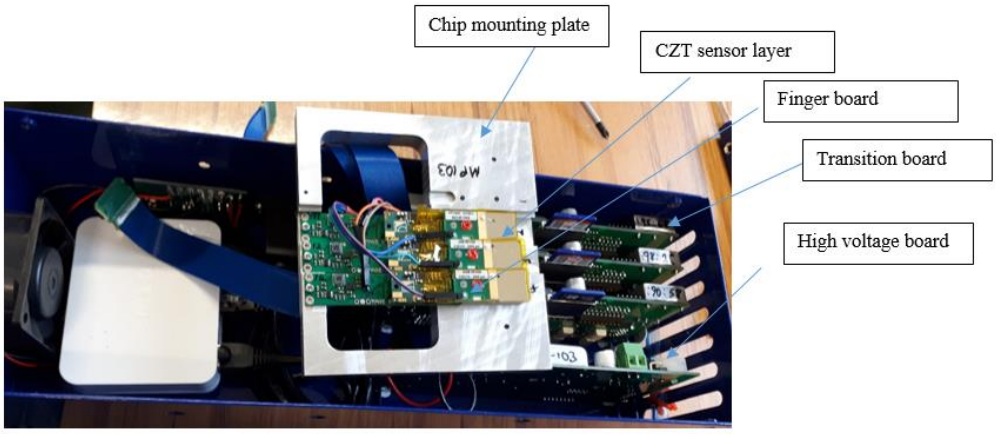

Figure 2.5 Interior image of the three CZT Medipix3rx MARS camera that consists of the detector assembly, readout, and high voltage board.

Figure 2.6 Interior image of the seven chip CdZnTe Medipix3rx MARS camera that consists of the detector assembly, readout, and high voltage board. (Image courtesy:Prof. Anthony Butler)

2.4.3 MARS image processing

The images saved in the MARS console are transferred to an image processing system for pre-processing, image reconstruction and material discrimination. This workstation processes the raw and reconstructed data in DICOM format. These components enable the researcher to analyze the spectral CT data and produce spectral images using different techniques [20].

2.4.4 MARS Vision

The MARS Vision workstation allows the users to visualize reconstructed spectral CT data in a 3D format. MARS vision consists of an interactive data visualization software and a high-speed computer that allows the user to analyze and visualize spectral CT data.

It is pre-installed on a dedicated visualization computer that is supplied alongside the MARS scanner and the data processing server. The user can analyse energy images to display 3D material images. Some of the material images are discussed in the application section in 2.7.

Figure 2.7 MARS vision workstation.(Image courtesy:MARS Bioimaging)

2.5 Characteristics of MARS imaging

MARS scanners use a single exposure to identify and quantify different low-Z and high-Z materials simultaneously, with high spatial and energy resolution. Therefore, using different contrast materials, the MARS scanner provides quantitative tissue information at the histological level. The MARS scanner enhances the contrast of soft tissue imaging by measuring the lipid and water composition. Due to the use of energy resolving Medipix3RX detector, the MARS scanner produces fewer image artifacts in the reconstructed image [9].The MARS scanner creates raw and flatfield data that offer pre-reconstruction and post-reconstruction fascilities. Accurate quantitative tissue information is achievable with a MARS scanner, which fulfils a key requirement in precision medicine [18].

2.6 Image quality metrics for MARS scanner

Different image quality metrics such as line spread function, point spread function, edge spread function, the contrast to noise ratio, uniformity of the image noise, modulation

transfer function and method of spectroscopic calibration were discussed as part of spectral imaging performance.

2.6.1 Spread function

To characterize the image sharpness of CT, point spread function (PSF) and modulation transfer function (MTF) are frequently employed. The PSF and MTF are used in basic studies evaluating the physical performance of a system and are also applied to image simulations of small structures and to image filtering techniques. In all these procedures, it is critical to determine PSF and MTF with high precision and accuracy. To evaluate the image sharpness in the scan plane, MTF measurements are performed by using a phantom such as a point or line. Methods that use these phantoms, such as a thin wire or a microbead, are most widely utilized for CT systems as they are conceptually simple and relatively easy to implement [21, 22, 23, 24, 25].

2.6.2 Image noise

Image noise is visualized as the random variation of brightness or color information in images. When a uniform material is imaged on a CT scanner, examination of the CT values for individual pixels in a localized area shows that the CT numbers are not all the same, but fluctuate around a mean value. This random variation is known as image noise and is due primarily to the statistical nature of x-ray production and interaction with matter. In other words, the standard deviation of Hounsfield numbers within a region of interest (ROI) is also known as image noise [26, 27].

$$\sigma \propto \frac{\exp^{-\mu d}}{D.b^2.W.T} \tag{2.1}$$

where μ is the linear attenuation coefficient, d is the thickness of the object with attenuation μ, $\exp^{\mu d}$ is the attenuation of the object, D is the CT dose index $CTDI_{vol}$, b^2 is the sampling distance at the rotation center (pixel size), W is the beam collimation, and T is the slice thickness. The image noise dependence on dose can be expanded by taking into account that the dose varies linearly with tube current and with exposure time. In addition, image noise dependence on tube peak voltage can be introduced since the radiation dose varies as equation (2.2).

$$D \propto kVp^n \tag{2.2}$$

where kVp is the peak voltage and n is a kilovoltage dependency factor. The value n depends on the radiation quality of the beam, tube output, and detector response. Equation (2.1) can be rewritten by inserting the tube voltage (kVp), tube current (mA), and exposure time (s) dependences on dose, yielding

$$\sigma \propto \frac{\exp^{-\mu d}}{mA.s.kVp^n.b^2.W.T} \tag{2.3}$$

2.6.3 Contrast to noise ratio

The ability to distinguish between materials depends upon their contrast and also upon the measurement noise of the system. Poor counting statistics can render two materials indistinguishable regardless of the differences in their attenuation values. While the image noise in a uniform material is usually a good indicator of the ability to visualize small contrast differences in diagnostic images, a more versatile measure is that of CNR [26].The contrast-to-noise ratio CNR quantifies contrast relative to random pixel noise. The SNR is a measure of the average value of a signal relative to its background noise. A thicker tissue will decrease the SNR because the x-rays have to travel through a greater thickness and give a greater attenuation. These factors reduce the CNR of the image. The value of CNR has been used to interpret the overall quality of the CT image, or how well a given image shows low contrast objects. The CNR is defined as:

$$CNR = \frac{\mu_{\text{det ails}} - \mu_{background}}{\sqrt{\sigma^2_{\text{det ails}} - \sigma^2_{background}}} \tag{2.4}$$

where $\mu_{details}$ and $\mu_{background}$ are the attenuation coefficients for the detail (material) and the background. $\sigma_{details}$ and $\sigma_{background}$ are the corresponding standard deviation for the detail and the background. CNR is also known as the difference in SNR between two different materials.

2.6.4 Uniformity of image noise and CT number

A scan of a water-filled phantom should give a CT image with similar pixel values, and similar amounts of noise, across the whole field of view. However, in practice, scans of uniform phantoms often show gradual variations of CT number and noise values across the image. These variations may be particularly noticeable when the uniform phantom is surrounded by a high contrast material, such as cortical bone substitute material. Variation is also noticeable at the extremities of large phantoms, particularly when an exceptionally large phantom is used to investigate the extended fields of view. If a phantom, or patient, is not centered at the isocenter, a more pronounced variation of CT number and image noise is also likely to be observed. The uniformity of CT number is of importance when the scanner is used for quantitative assessment of CT values, particularly for radiotherapy [26].

2.6.5 Spatial resolution

Spatial resolution in CT is the ability to distinguish between object or structures that differ in density. A high spatial resolution is important for one to discriminate between structures that are located within a small proximity to each other, and for small structure. Factors affecting CT spatial resolution are the field of view, pixel size, focal spot size, magnification, the motion of the patient, pitch, kernel, slice thickness, and detector size [28]. The determination of spatial resolution can be made through the use of a high contrast test object through visual inspection or computation to compute the modulation transfer function (MTF) or with the use of an appropriate test object to compute the MTF. The MTF is commonly derived from the image of a bead or wire to give a point spread function (or of an edge to give an edge spread function). Standard methods are then used to compute the MTF from either the point spread function or the edge spread [26].

2.7 Potential applications of MARS scanner

The MARS scanner plays an important role in different pre-clinical applications. The current small bore MARS scanner has contributed in different pre-clinical areas such as monitoring the biomarker for cancer imaging, identifying unstable atherosclerosis plaque and its treatment, characterizing cartilage to identify osteoarthritis, and applications in the meat industry. The recent breakthrough is the application of a human-sized to image live human patients MARS scanner.

- **Monitoring atherosclerosis plaque disease**

Conventional CT scanners are unable to monitor and quantify the composition of the unstable atherosclerosis plaque. The MARS scanner enables imaging and distinguishing pathological features of cardiovascular disease at high spatial resolution (for example, the components of atherosclerotic plaque). MARS has the capacity to characterize and monitor the unstable atherosclerosis plaque. It affords information non-invasively about tissue composition indicating healthy and unhealthy tissues. Figure 2.8 shows a MARS image of the different components of an excised human carotid plaque. In this way the MARS scanner can identify unstable plaque before an individual has a coronary heart attack or stroke [20].

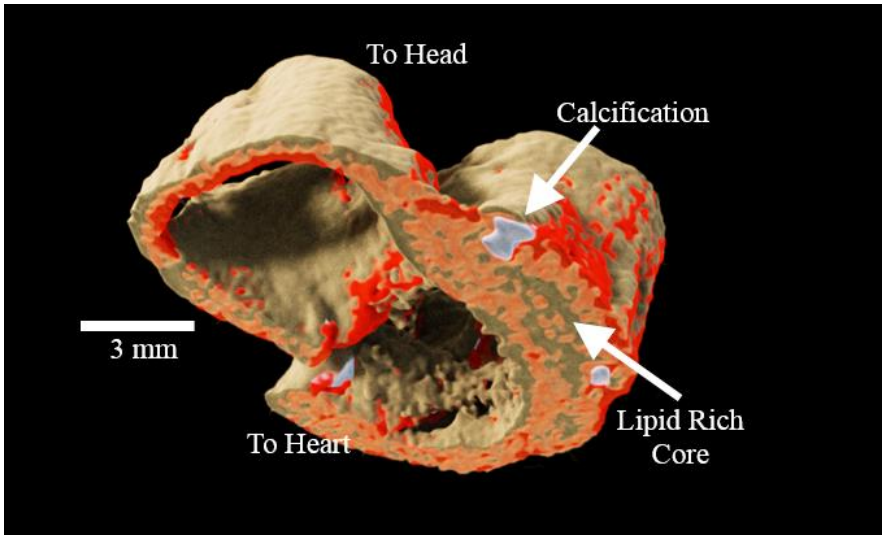

Figure 2.8 MARS image of atherosclerosis plaque that shows the soft tissue in red, white in calcification and gray in lipid core. (Image courtesy: MARS Bioimaging)

- **Identification and quantification of contrast agent**

Conventional CT exam have traditionally been confined to the use of a single contrast agent per scan. MARS spectral CT offers the researcher a tool that can identify and quantify a range of contrast agent as well as intrinsic markers such as lipid bone and soft tissue. MARS also has the capacity to discriminate among low atomic number materials, and from a range of concentrations of heavy atoms. Figure 2.9 shows a MARS image of the differentiation and quantification of different contrast substances such as gold, gadolinium, iodine, hydroxyapatite, lipid and water with in a multi-contrast phantom. Quantitative information of every material can be measured in (mg/ml). Figure 2.10 shows a 3D MARS image of a mouse that was injected with two contrast agents and the different colors represent distinct contrast agents in the specific organ of interest [4, 29].

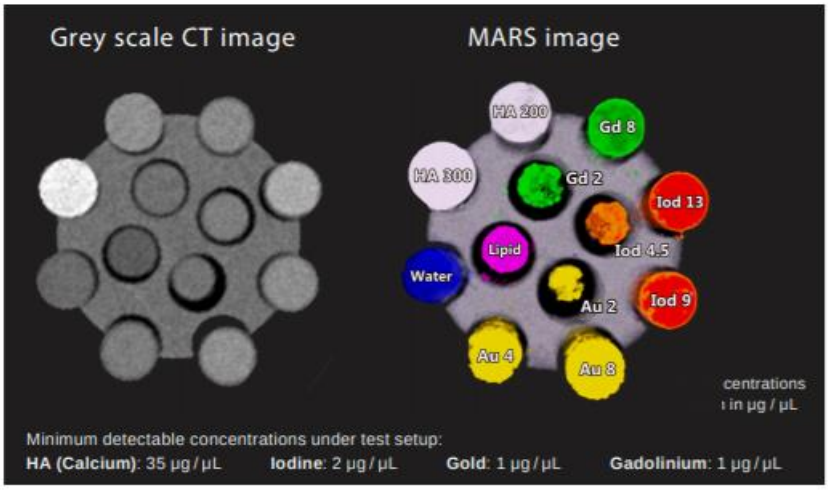

Figure 2.9 MARS image of multi-contrast phantom including different high-Z materials that can be identified and quantify simultaneously in the different color.(Image courtesy:MARS Biomaging)

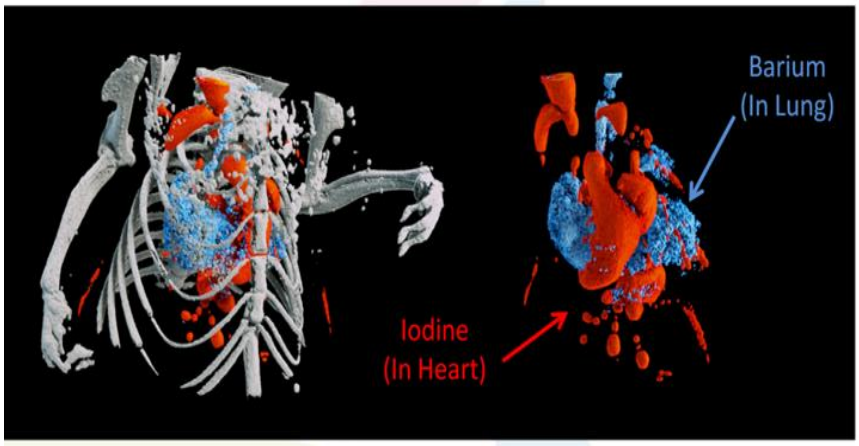

Figure 2.10 A mouse containing the different contrast agent that was once imaged via MARS scanner to be aware of the quantitative tissue information.(Image courtesy: MARS Biomaging)

- **Nanoparticle guided drug delivery for cancer imaging**

The MARS system opens the door to targeted imaging probes on CT. Knowing whether or not an antibody-based treatment has reached its target tissue is inherently difficult. MARS spectral CT affords an approach to track nanoparticles, permitting preclinical researchers to have confidence that their drug has reached it target cells. Medipix3RX based MARS scanner has potential to visualize tumor response to the use of nanoparticle guided drug delivery. This has the ability to describe markers of disease activity and response to therapy in one scan, also eliminating the need for biopsy. Due to the benefit of spectroscopic imaging, MARS can accelerate future drug development for most cancers and inflammatory disease [4].

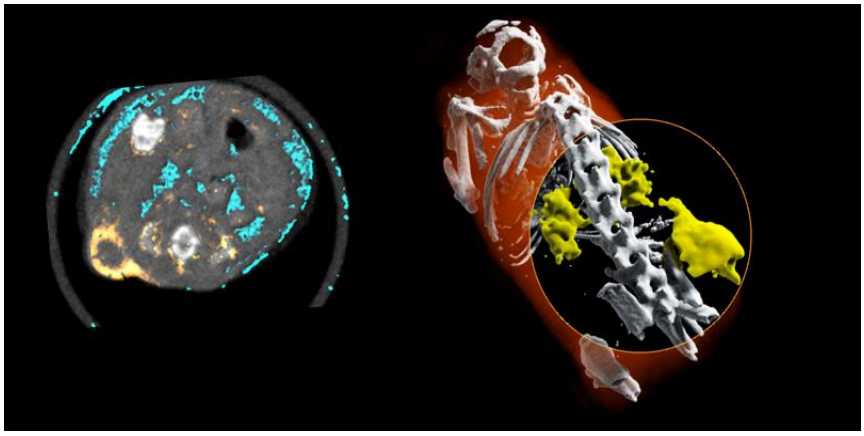

Figure 2.11 Gold-nano probes within a murine mouse model of lung cancer, with a 2D magic lens, used to enhance the view of the region of interest. (Image courtesy: Mahdieh Moghiseh).

- **Characterization of osteoporosis and cartilage health**

Another essential application of spectral CT is to characterize joint health. The MARS scanner allows for non-invasive measurement of cartilage fitness in joints. In this way, it can supply earlier prognosis and better treatment options. It can consider the deterioration of cartilage health that occurs throughout osteoarthritis due to the depletion of glycosaminoglycans (GAG) in the extracellular matrix of articular cartilage. Spectral CT has the potential to quantify contrast media for cartilage evaluation as well [30].

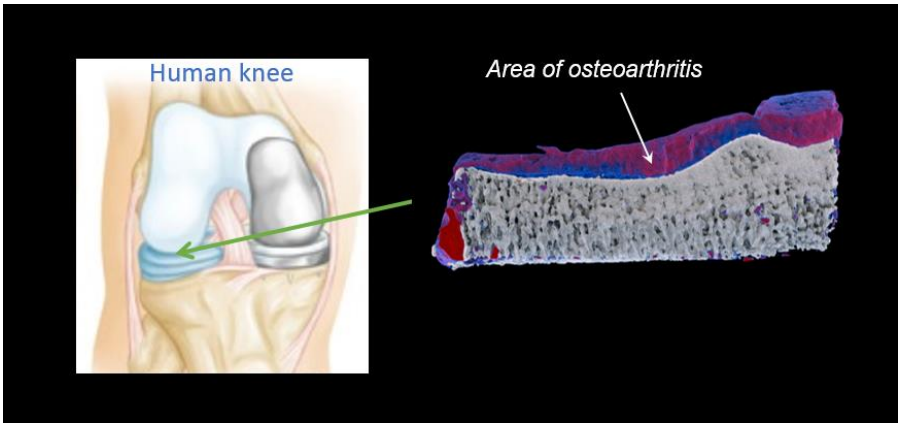

Figure 2.12 The right image shows a 3D view of a lateral tibial plateau sample with simultaneous display of calcium and iodine material. The gradient of colors (blue to red) describes the amount of iodine (inversely related to GAG) present in the cartilage.(Image courtesy:MARS Biomaging)

- **Industrial application**

The MARS scanner can characterize meat quality and can potentially make contributions in livestock research. Figure 2.13 shows the lamb tissue with fat, muscles, meat and bone. High soft tissue sensitivity is also pleasing for the meat industry to make accurate portioning and figuring out low and high-fat regions. It additionally can pick out and quantify the thin layer of the fat from muscle [31].

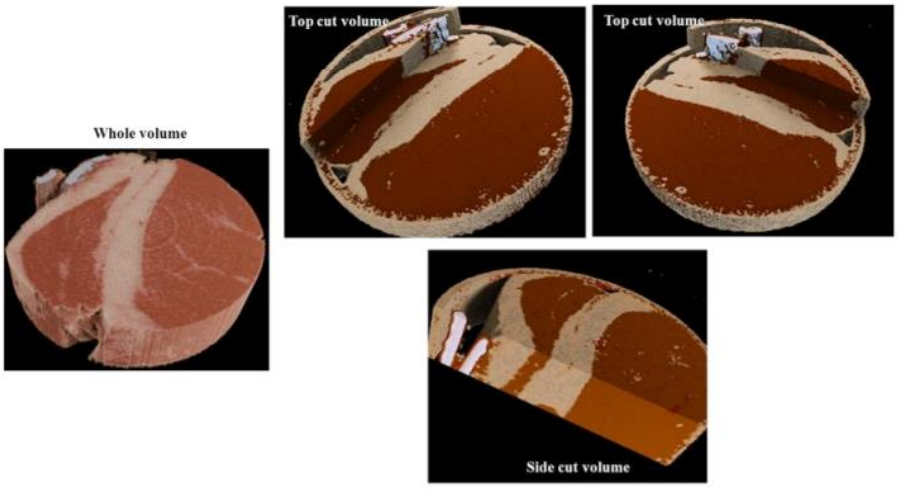

Figure 2.13 3D volume rendering of lamb meat the use of the MARS system. A clear separation within the meat shape between fats (off-white colour scheme), meat (reddish), fat marbling and bone (showing calcium in white) can be seen.

- **First human imaging using MARS scanner**

The MARS scanner has been translated from preclinical to human imaging. Our team developed a large bore human scanner using Medipix photon counting detectors that are capable of scanning body parts of a human subject. The first human images of living human the use of MARS spectral scanner were published in July 2018. Figure 2.14 shows these image. This enables high-resolution, high-contrast, very reliable images, making it unique for several imaging functions medical imaging [32, 33, 34].

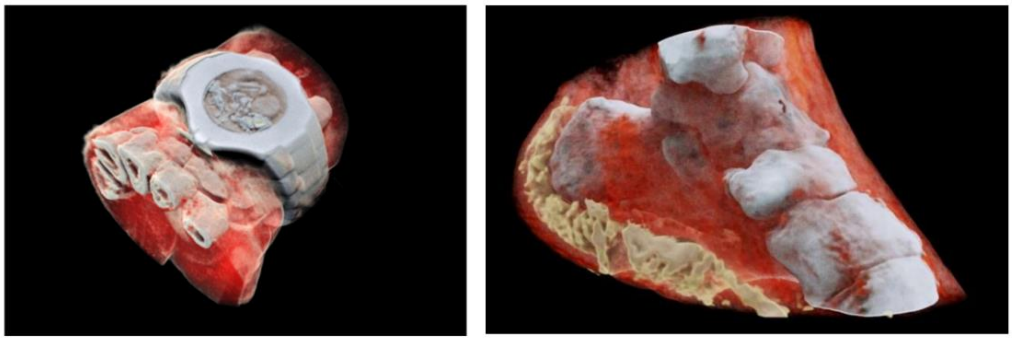

(a) (b)

Figure 2.14 First human image of (a) wrist with the watch and (b) ankle imaged with MARS spectral scanner that can clearly identify bone, soft tissue, and blood.(Image courtesy:MARS Biomaging)

2.8 Summary

- The MARS spectral scanner is equipped with Medipix photon counting detector that can produce the high spatial 3D color image.

- Medipix is a semiconductor photon counting detector has high spatial and spectral resolution. It has user defined energy thresholds that can be divided in up to eight energy thresholds over the entire x-ray spectrum to measure attenuation difference.

- Due to the photon counting Medipix detector, MARS can overcome conventional imaging modalities with respect to low contrast material identification, and contrast agent quantification.

- The main characteristics of MARS spectral imaging is that it can identify and quantify different material simultaneously.

- The main component of the MARS imaging chain are a scanner, camera, workstation, and vision.

- MARS scanner play an important role in different pre-clinical studies such as monitoring the biomarkers of cancer and its treatment; identifying and monitoring unstable atherosclerotic plaques; inflammatory diseases; cartilage characterization for early diagnosis of osteoarthritis

- Currently MARS human scanner able to scan different body parts of living human.

3 Characterization of measurement variability

3.1 Introduction

This chapter investigates measurement variation in the MARS scanner. A systematic procedure was established to quantify and characterize the different types of variability during protocol commissioning. A pilot study was conducted to evaluate the measurement variation in MARS scanner. Section 3.2 reports experimental design and the multicontrast phantom used to characterize this variability. The inter-scan and intra-scan measurement variation of mass attenuation of different materials were assessed using the relative standard error. The Bland-Altman method was applied to measure the proportional bias of different measurements.

Characterizing the sources of measurement variability is very important to obtain better image quality and higher sensitivity for detecting different materials. Toru Kobayashi et al. evaluated the accuracy of linear attenuation coefficients using a photon counting CT system [35]. It was found that the linear attenuation coefficient of single materials agreed with the theoretical values better than the composites materials. Tyler E. Curtis et al. investigated the spatial and quantitative accuracy of material decomposition for mixed contrast agents [36]. They also showed that quantitative errors in material decomposition was low. It was found that the value of root mean square (RMSE) was less than 12% of the maximum signal for each material in mixed compositions.

If we correct and optimize the scanner parameters on the basis of finding variability, it would serve to stabilize the operation of MARS scanner. There are many factors which lead to observable variations in MARS system. Examples of this include mechanical misalignment, inter-pixel differences, changes in detector temperature, detector instabilities, and drift in energy thresholds. These variations can severely degrade the measured spectral signal. Inter-pixel variation reduces the energy resolution [37]. Geometric misalignment produces image blurring (as explained in chapter 6). Temperature variation and detector instability affect the energy response of the Medipix detector and causes threshold drifting. Variations such as these, if unaccounted for, result in image artifacts in the spectrally reconstructed data. Characterization of these variables, and their effects on the measured spectral signal, improve the validity and reproducibility of the spectral data obtained with MARS scanner.

In this study, a framework was established to quantify the measurement error of the mass attenuation coefficient of different materials and showed the effects of different experimental noise level in the measured spectral signal in different materials.

3.2 Materials and methods

In this section, the materials and methods are presented to perform different experiments

3.2.1 Experimental setup

Three sets of experiments were performed on the MARS-4, MARS-10, and MARS-11 scanners to quantify the inter-scan and intra-scan measurement variation. In this section, the details of the experimental setup and a description of the multicontrast phantom are presented.

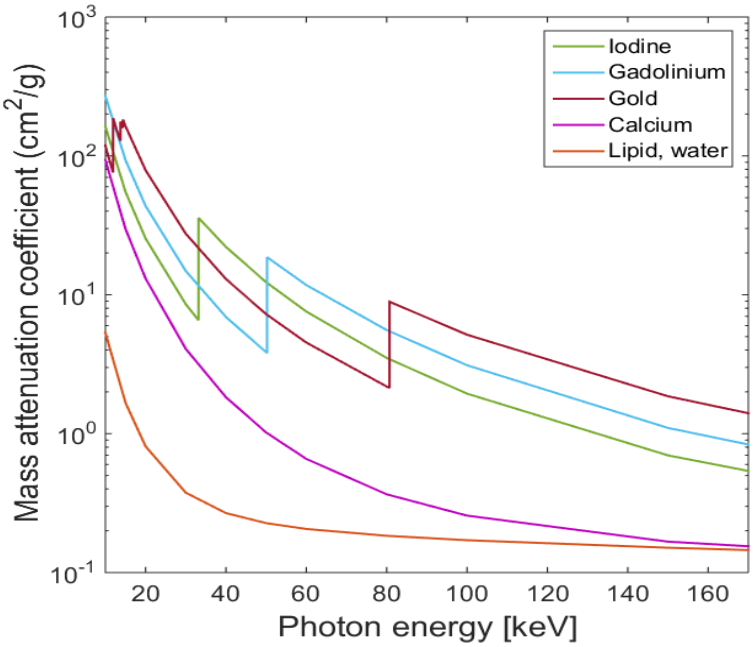

Figure 3.1 Comparison of mass attenuation coefficients for iodine, gadolinium, gold, calcium, lipid and water over the x-ray spectrum of 20-120 keV.

3.2.2 Multicontrast phantom

Two different types of multicontrast phantoms were used in these experiments. Both phantoms were circular with diameter of 31 mm. Nine vials including different materials were used and the diameter of each vial was 6 mm. The vials of these phantoms were filled

with water and lipid as single materials and calcium, gadolinium, iodine, and gold as composite materials. The composite materials are also divided into two categories of non-K-edge materials such as calcium which does not have K-edge in the diagnostic energy range. Gold, gadolinium, and iodine which has K-edge properties, as shown in Figure 3.1. K-edge materials are often used as contrast agents as they enhance the visibility of fluid or structures of tissue in the body. The multi-contrast QA phantom consists of different material concentrations of lipid, water, 8 mg/ml and 2 mg/ml of gold, 8 mg/ml and 2 mg/ml of gadolinium, 18 mg/ml of iodine and 240 mg/ml of calcium. The composition of GdI phantom are lipid, water, 8 mg/ml, 4 mg/ml, 2mg/ml, 1 mg/ml of gadolinium and 2.25 mg/ml, 4.5 mg/ml and 9 mg/ml of iodine.

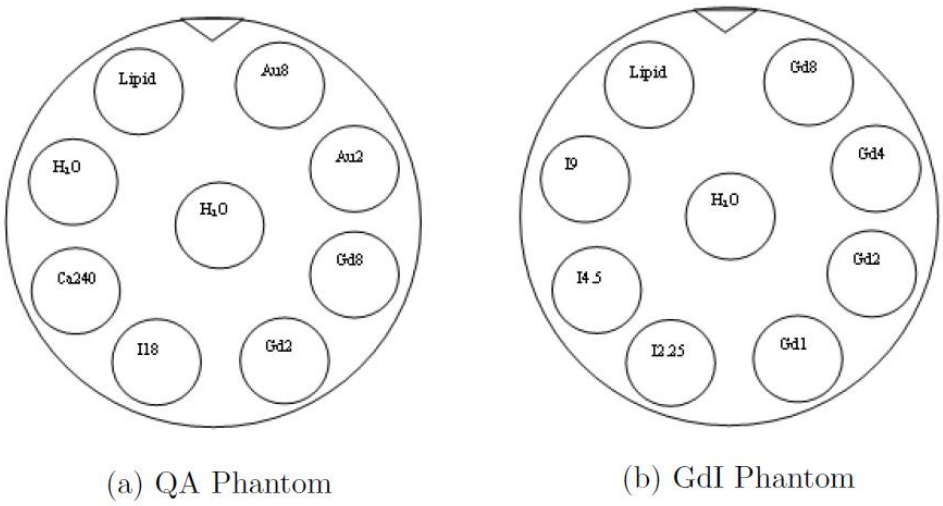

(a) QA Phantom (b) GdI Phantom

Figure 3.2 Schematic diagram of multi contrast QA phantom (left) and GdI phantom (Right) with various concentrations (mg/ml).

3.2.3 Preliminary study of inter-scan and intra-scan variation

A preliminary study was performed to evaluate the inter-scan and intra-scan measurement variation in the MARS scanner. In this investigation, three different experiments were performed on different days in different MARS scanners using different protocols and different phantoms. Initially, inter-scan and intra-scan measurement variation of the detected mass attenuated signal from different composite materials were found. Two multi-contrast phantoms were used in these measurements. In general, the variation between the spectral signals of gold, gadolinium, iodine, and calcium which are composite materials, was significantly higher compared to the single materials (lipid and water). Such measurement

variation originates from different instabilities in MARS scanner. The results of each experiment are presented in section 3.5.

3.2.4 Experimental setup for study 1

The first set of experiments was performed by MARS-4 with a predefined protocol. The scan parameters of this protocol included the tube voltage of 80 kVp, tube current of 13μA, exposure time of 300 ms, and 3.1mm aluminum filtration. Source to object distance (SOD), Object to detector distance (ODD) and the source to detector distance (SDD) was 131.8 mm, 55 mm and 186.8 mm, respectively. The camera used in this scanner was a Medipix3RX detector flip-bonded to 2 mm CZT. Three back-to-back scans were performed using the same protocol and same multi-contrast phantom on the same day. Four energy bins were set to 18-30 keV, 30-45 keV, 45-57 keV, 57-78 keV in charge summing mode (CSM) so that these energy ranges identified of the K-edge materials. The K-edge of gadolinium (50.24 keV) is in the third energy bin, K-edge of iodine (33.17 keV) is in the second energy bin. K-edge of gold (80.72 keV) may also be identified at 57-78 keV energy bin.

3.2.5 Experimental setup for study 2

The second series of measurements was obtained from MARS-4 with the same scan protocol as study1 while using the GaAs-Medipix3RX camera. Three back to back scans were performed using the same protocol setting on the same day. In this study, the GdI sensitivity phantom was scanned.

3.2.6 Experimental setup for study 3

The third set of measurements were performed using MARS-11 with a predefined protocol. The scan parameters of this protocol included the tube voltage of 120 kVp, tube current of 13 μA, and exposure time of 300 ms, and 3.1 mm aluminum filtration. The SOD, ODD, and SDD were 200 mm, 50 mm and 250 mm, respectively. The camera used in this scanner was a Medipix3RX detector flip-bonded to 2 mm CZT. Five back-to-back scans of the multi-contrast phantom were taken using the same protocol. Four energy bins were set to 7-18 keV, 18-30 keV, 30-45 keV, 45-75 keV and 75-120 keV in CSM mode.

3.3 Data analysis

3.3.1 Region of interest selection

To process each set of the reconstructed images, ImageJ (an image processing software) was used. To obtain the average measurement for each energy bin, a stack of each image dataset was processed through “Z Project”, which provided one image per energy bin (i.e. the start and the stop slices were 100 and 110 in the stacked images).

The same circular ROI was selected for each material from the averaged images. The area of ROI was 15 mm^2. Figure 3.3 shows the selected ROIs for a QA phantom in the first energy bin. Next, the average of the linear attenuation coefficient of each material was calculated for the corresponding ROI of the averaged image.

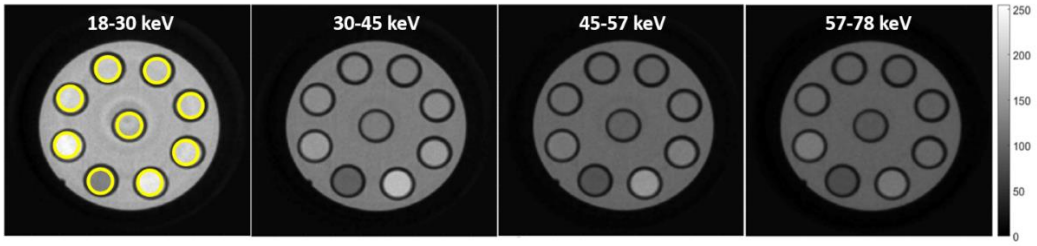

Figure 3.3 Reconstructed images of a QA phantom obtained by MARS-4 with GaAs-Medipix3RX detector in four energy bins. In the first image from the left, selected ROIs are also demonstrated.

3.3.2 Calculation of mass attenuation coefficient

To analyze the measured data, the mass attenuation coefficient of material was used because it is an energy-specific feature of a material, and therefore is independent of density. The mass attenuation coefficients of material can be extracted from equation (3.1).

$$\mu = \sum_{m}^{material} \rho_m \left(\frac{\mu}{\rho}\right)_m \tag{3.1}$$

Where, μ is the linear attenuation of material that can be obtained by the reconstruction algorithm from the measured data in a spectral CT system. ρ_m is the concentration or density of m as a material of interest and μ/ρ is the mass attenuation for material of m. Linear attenuation and mass attenuation coefficients vary with energy. For lipid and water, which are not the composite materials, their mass attenuation coefficients are easily obtained by substitution of their densities in equation (3.1). For instance, the mass attenuation of lipid with density of 0.9 g/ml is calculated by equation (3.2)

$$\mu_{lipid} = 0.9 \times \left(\frac{\mu}{\rho}\right)_{lipid} \tag{3.2}$$

For the composite materials such as calcium solution, equation (3.1) is extended as the following equation.

$$\mu = \rho_w \left(\frac{\mu}{\rho}\right)_w + \rho_m \left(\frac{\mu}{\rho}\right)_m \tag{3.3}$$

Where w denotes water and μ_c denotes the composite attenuation which includes water used for making a solution. In a multicontrast phantom, several concentration of the composite materials are typically used. For each concentration of a composite, a system of equations can be formulated equation (3.4). In the second line of this system of equations, ρ_m is the known concentration for the material such as calcium or gold in the solution, and this parameter is zero which is representing pure water [30].

$$\begin{aligned} \mu_c &= \rho_w \left(\frac{\mu}{\rho}\right)_w + \rho_m \left(\frac{\mu}{\rho}\right)_m \\ \mu_w &= \rho_w \left(\frac{\mu}{\rho}\right)_w + 0. \times \left(\frac{\mu}{\rho}\right)_m \end{aligned} \tag{3.4}$$

The mass attenuation coefficients of a composite material with different concentrations are calculated by solving the overdetermined system of equations and finding the regression average of the system. For instance, the following equation represents the linear system for the mass attenuation coefficient of gold in a given energy bin [38].

$$\begin{pmatrix} \rho_{gold1} \\ \rho_{gold2} \end{pmatrix} \left(\frac{\mu}{\rho}\right)_{gold} = \begin{pmatrix} \mu_{gold1} - \mu_{water} \\ \mu_{gold2} - \mu_{water} \end{pmatrix} \tag{3.5}$$

The regression fit can be performed through the $\mathrm{X} = \mathrm{lsqnoneg}(\mathrm{A}, \mathrm{B})$ function in MATLAB. X is the mass attenuation coefficient, A is the density of the material and b is linear attenuation of the material.

3.3.3 Statistical analysis

3.3.3.1 Relative standard error

The variation of the mass attenuation coefficients between different scans was assessed by calculation of relative standard error (RSE). For this calculation, the standard error of the mean of mass attenuation coefficient was calculated by the following equation,

$$SE = \frac{S}{\sqrt{n}} \tag{3.6}$$

where, S is the standard deviation calculated for each material across different measurements at each energy bin and *n* is the number of measurements. The next step is the substitution of SE in equation (3.7) to obtain the RSE value for each material. The RSE is expressed in percent.

$$RSE = \frac{SE}{\overline{X}} \times 100 \tag{3.7}$$

Where, $\overline{X}$ is the mean of mass attenuation coefficients of each material across different scans within a set of measurements at each energy bin.

3.3.3.2 Bland-Altman method

The Bland-Altman (mean-difference or limits of agreement) plot and analysis is used to compare two measurements of the same variable. It is a method for comparison technique. In clinical imaging, it is common to verify the agreement between two quantitative techniques of measurements. Bland-Altman (BA) proposed an alternative analysis, based on the quantification of the agreement between two quantitative measurements by studying the mean difference and constructing limits of agreement. The limits of inter examination agreement were defined as the mean difference ±1.96*the standard deviation (SD). The (BA) plot analysis is a simple way to evaluate the proportional bias and to estimate an agreement interval, within which 95% of the differences of the second method agree when compared to the first one [39, 40].

In this study, the Bland-Altman method was applied to measure the proportional bias between two measurements of different back-to-back measurements (scans). The linear attenuation coefficients of each voxel corresponding to each material within the region of

interest (ROI) were calculated to draw (BA) plot. The attenuation difference of different materials were plotted against the average of linear attenuation between two measurements. Limit of agreement between two measurements for each material was evaluated using (BA) method. Figure 3.14 to Figure 3.18 illustrate the (BA) plot for different materials at lower energy bin.

3.4 Inverse problem

An inverse problem is defined as the process of calculating the casual factors that produced measurements variations. The inverse problem will use a model to reconstruct an input from the corresponding output. Inverse problems are encountered typically in situations where one makes the indirect observations of a quantity of interest. It is called an inverse problem because it starts with the results and then calculates the causes [41].

Many problems in the physical sciences are highly sensitive to changes in their input. These include medical imaging, remote sensing, image restoration, and astronomy. These mathematical model can be expressed as a linear system of the equation as

$$Ax = b \tag{3.8}$$

In this system the matrix $A\epsilon\mathbb{R}^{m\times n}$ with $m \geq n$ describe the model. The input is some vector $x\epsilon\mathbb{R}^{n}$ and the output is presented in the vector $b\mathcal{E}\mathbb{R}^{m}$. The inverse problem associated with this model computes the input x given some output b and the known model [42]. The approximate solution to the linear least square minimization problem associated with the linear system of equation (3.8).

$$\|Ax - b\|_2^2 \tag{3.9}$$

Where $\|.\|$ is the Euclidean norm. The value of x is very sensitive to changes in the data b. This sensitivity is important to consider when an error may contaminate the data. If the available data is not exact, then even a small error may enough perturb the solution by an enormous amount.

Let us consider the available data is contaminated with an error that is the available data can be written as

$$b = \tilde{b} + \varepsilon \tag{3.10}$$

Where the vector $\tilde{b}$ is the exact data and the error in the data is contaminated by the vector ε. Now the desired solution of x is the solution to the linear system of equations containing the error-free data

$$Ax = \tilde{b} \tag{3.11}$$

Since the problem is so sensitive to change in the data, even a small error may distort the computed solution considerably. The computed solution may be very different from the desired solution and ultimately meaningless.

There are different factors in spectral CT that can impact the solution. These include threshold drifting, detector instability, geometric misalignment, statistical noise and beam hardening. The reconstructed images obtained on several MARS scanner affected by these types of distortion that produce measurement variation.

If experimental noise ε from threshold drifting, statistical noise, and beam hardening, etc is added up to b term and the sample preparation uncertainty (E) is added up to A, then equation (3.8) become

$$(b + \varepsilon) = (A + E)x \tag{3.12}$$

Equation (3.12) can be rewritten as

$$x = (A + E)^{-1} b + Noiseterm \tag{3.13}$$

The mass attenuation coefficient of composite materials can be expressed as

$$\begin{bmatrix} \left(\frac{\mu}{\rho}\right)_{ca} \\ \left(\frac{\mu}{\rho}\right)_{w} \end{bmatrix} = \left(\begin{bmatrix} \rho_{ca}^{1} & \rho_{w}^{1} \\ \rho_{ca}^{2} & \rho_{w}^{2} \end{bmatrix} \right)^{-1} \begin{bmatrix} \mu_{ca}^{conc1} \\ \mu_{w}^{conc2} \end{bmatrix} \quad (3.14)$$

Where, $x = \begin{bmatrix} \left(\frac{\mu}{\rho}\right)_{ca} \\ \left(\frac{\mu}{\rho}\right)_{w} \end{bmatrix}$, $A^{-1} = \left(\begin{bmatrix} \rho_{ca}^{1} & \rho_{w}^{1} \\ \rho_{ca}^{2} & \rho_{w}^{2} \end{bmatrix} \right)^{-1}$ and $b = \begin{bmatrix} \mu_{ca}^{conc1} \\ \mu_{w}^{conc2} \end{bmatrix}$

Therefore, small noise in the forward form of equations (3.13) and (3.14) is magnified in the inverse form in which A^{-1} maps b to x. This is called "inverse noise amplification" and it becomes more significant when a composite material is used because it involves the all sources of noise that were mentioned above for each component. In the case of K-edge materials, small changes in threshold drifting results in a large change in reconstructed images that produces measurement variation.

3.5 Results

In this section, the results of each study are presented.

3.5.1 Study 1, using MARS-4 with CZT-Medipix3RX

Figure 3.4 shows the results of study1 that represents the mass attenuation profiles of different materials in different energy bins for three repeated measurements. The value of mass attenuation in scan-1 is clearly far from scan-2 and scan-3 and it means that there exist variation in the measurements for gold, gadolinium, and iodine. It is also clear that the second, third and fourth energy bin have significant variation of mass attenuation in all composite materials. On the other hand, water and calcium have less variation in all energy bins of different scans. Scan-2 shows slight variation in the second energy bin for lipid. The variation of mass attenuation of different materials was assessed by measuring the relative standard error (RSE). Figure 3.5 represent the bar graph of (RSE) of mass attenuation of different material at different energy bins. It appears that all composite materials have a higher value in RSE at third energy bin. Maximum RSE was found and it is about 11.2% in case of gadolinium at third energy bin. On the other hand, lipid and water have minimum variation compared to the all composite materials in all energy bins. Figure 3.6 represents the box plot of all materials at different energy bins.

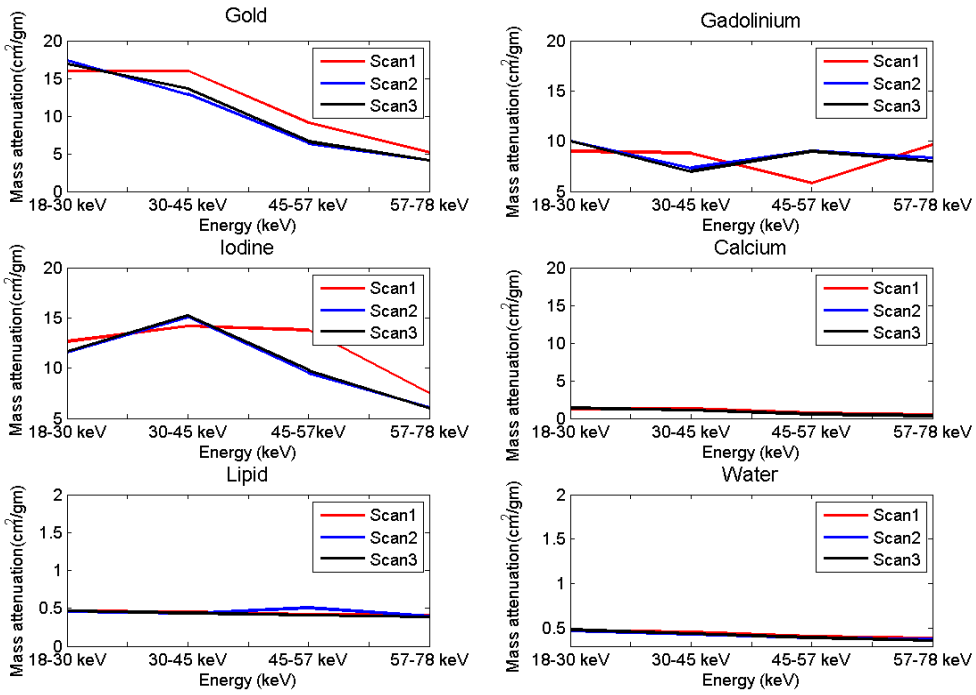

Figure 3.4 Mass attenuation profiles of gold, gadolinium, iodine, calcium, lipid, and water that used QA phantom scanned by MARS-4 with CZT-Medipix3RX detector. The mass attenuation coefficients of lipid and water are approximately the same but all composite materials show significant variation in each energy bins.

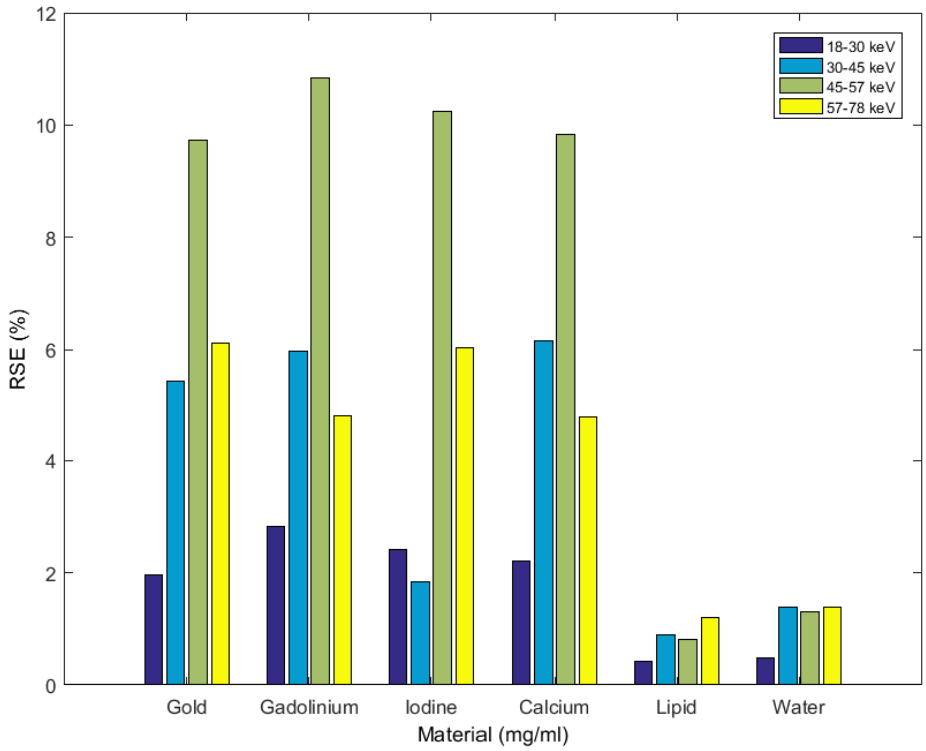

Figure 3.5 RSE of mass attenuation calculated for different materials of the phantom scanned by MARS-4 with CZT-Medipix3RX in different energy bins. Gold, gadolinium, iodine, and calcium show the maximum value of RSE of mass attenuation at third energy bin. Lipid and water have the lower RSE than the composite material.

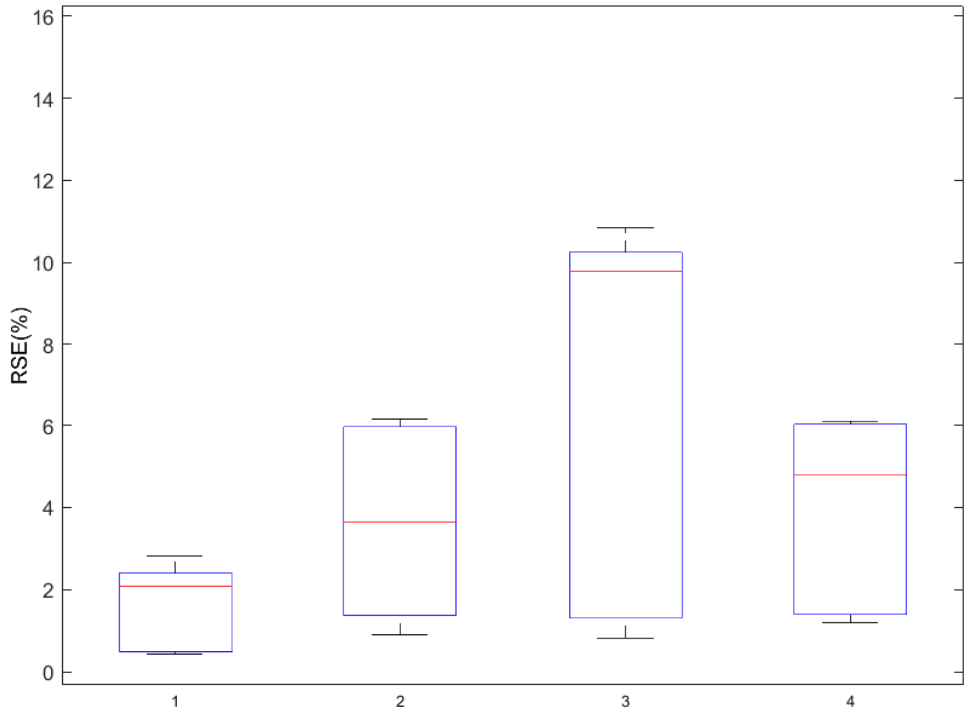

Figure 3.6 Boxplot of the relative standard error of mass attenuation for each energy bins.

3.5.2 Study 2, using MARS-4 with CZT-Medipix3RX

The results of study 2 (performed on MARS-4 with GaAs-Medipix3RX) are shown in Figure 3.7. This result represents the variation of mass attenuation of different materials such as gadolinium, iodine, lipid and water at different energy bins of three back-to-back scans. It is observed that the value of mass attenuation of lipid and water are the same in all scans. In contrast, composite materials have slight variation of mass attenuation at 18-30 keV, 30-45 keV and 45-57 keV. The variation of the mass attenuation was quantified by measuring the relative standard error (RSE) in Figure 3.8. The RSE values for iodine are also noticeably higher at 57-78 keV 30-45 keV that is (2.1% and 1.6%, respectively). The high RSE values for gadolinium occur at 18-30 keV, and 57-78 keV with the value of 1.7% and 1.8%. On the other hand, lipid and water have lower RSE values at all energies in all scans than gadolinium

and iodine. The attenuation variations of all materials are illustrated in Figure 3.9. The IQR is noticeable higher for the first energy bin than second and third energy bin. In this case, the minimum value of IQR at the fourth energy bin. The value of the median is higher at 18-30 keV whereas the value of the first quartile closely same at 30-45 keV, 45-57 keV.

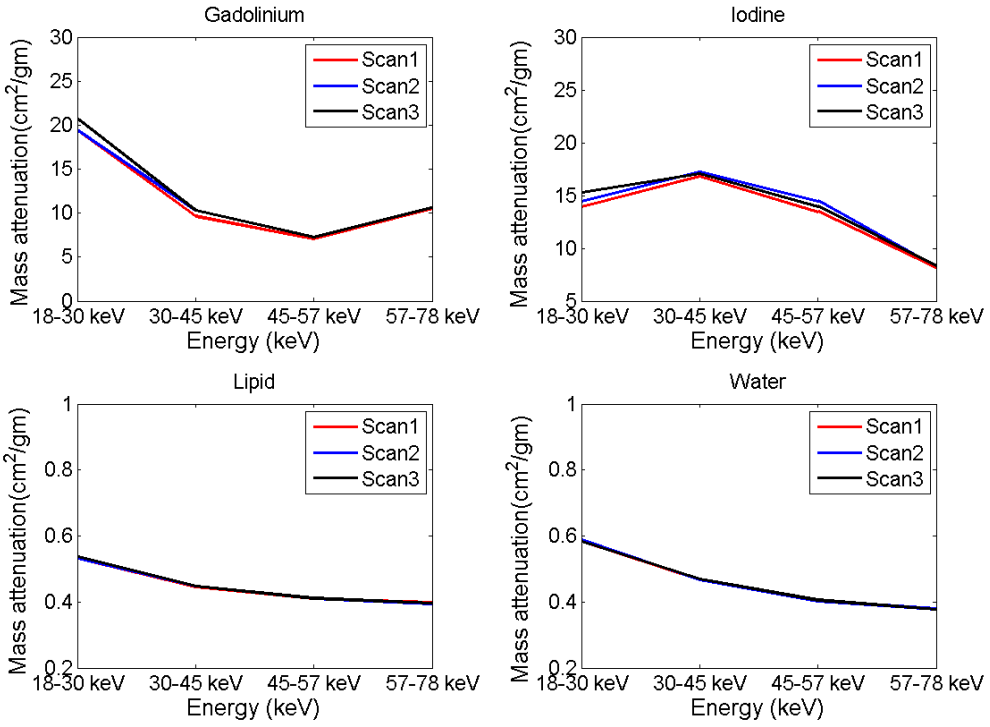

Figure 3.7 Mass attenuation profiles of gadolinium, iodine, lipid, and water that used GdI sensitivity phantom scanned by MARS-4 with GaAs-Medipix3RX detector. Mass attenuation coefficient of lipid and water are matched and for composite materials show a slight variation in the first three energy bins.

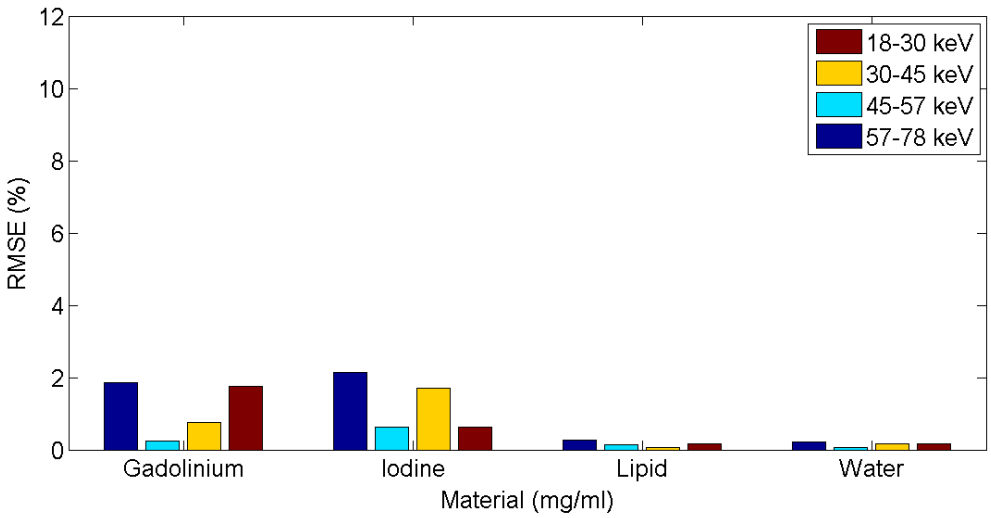

Figure 3.8 RSE of the mass attenuation coefficients for different materials of a GdI sensitivity phantom scanned by MARS-4 using GaAs-Medipix3RX detector. First and fourth energy bin shows the higher value of RSE in case of gadolinium whereas second and fourth energy bin shows the higher value of mass attenuation of iodine. Lipid and water have less RSE than all composite materials in each energy bins.

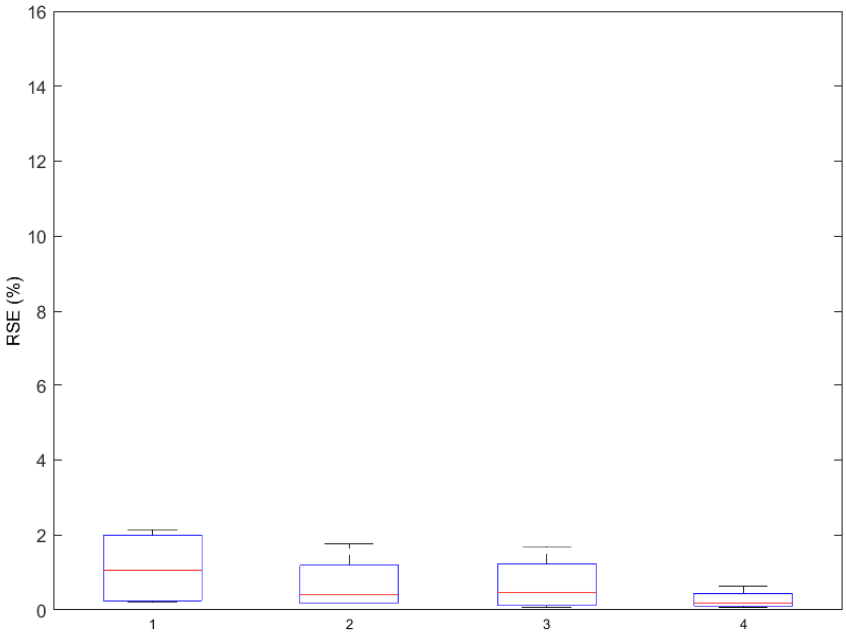

Figure 3.9 Boxplot of the relative standard error of study-2 that was performed by GaAs-Medipix3RX.

3.5.3 Study 3, using MARS-4 with CZT-Medipix3RX

The third study was conducted on MARS-11. In this study, five back to back scans were performed using the same protocol, the same multi-contrast phantom on the same day. Inter-scan and intra-scan measurement variations were observed in mass attenuation. The limit of

agreement between two measurements were evaluated using the Bland-Altman method to investigate the proportional bias in between two measurements. Figure 3.10 displays the mass attenuation profile of different materials at different energy bins for different scans. Figure 3.11 illustrates the intra-scan measurement variation of mass attenuation of different materials in different energy bins. Gold, gadolinium, iodine, calcium shows a higher variation of RSE than lipid and water and significant variation has appeared in the higher energy bins. Figure 3.12 represent the inter-scan measurement variation of mass attenuation of different materials in different energy bin in each scan. Scan 4 and 5 have higher variation in case of gold and calcium whears higher RSE appeared in scan 5 of iodine. In the case of gadolinium, all measurement in each scan have higher variation. While lipid and water have the same RSE value across all scan and in each energy bins.

The measurement error of different materials across the five scans is illustrated in Figure 3.13 Each high-Z material shows significant outliers above the box plot, indicates existence of variability in the measurement or experimental error. Therefore, the high-Z materials have a significant measurement error in the attenuated signal.

The Bland-Altman (BA) method was applied to evaluate the proportional bias as well as the limit of agreement between different scans. Linear attenuation coefficients of each voxel were calculated corresponding to the ROI for 8 mg/ml gold, gadolinium and 18 mg/ml iodine, lipid and water at lower energy bin to produce the BA plot. The linear attenuation difference of each voxel between two back-to-back scans was plotted against the average of linear attenuation of two scans for each material. The 95% limit of agreement between two measurements was evaluated by the upper limit and lower limit. From Figure 3.14, Figure 3.15 and Figure 3.16 , it is clear that in case of gold, gadolinium, and iodine there are some measurement points out the limit of agreement that should be noted to identify the measurement variation. In the case of lipid and water [Figure 3.17 and Figure 3.18] there is fewer points outside the limit of agreement. All measurement points of composite materials are less concentrated at the middle of the mean than lipid and water. From the point of limit of agreement, this indicate that all composite materials have higher measurement instability than lipid and water due to the effect of inverse noise amplification.

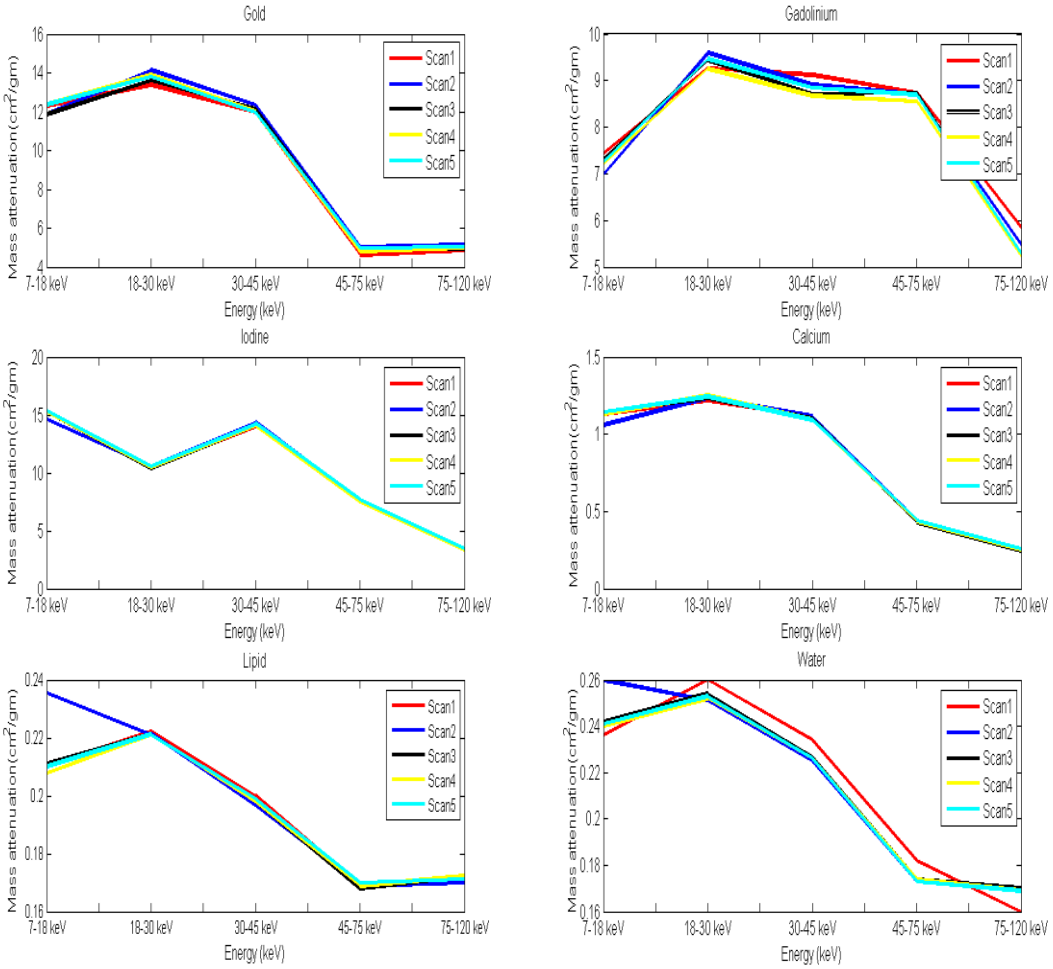

Figure 3.10 Mass attenuation profiles of gold, gadolinium, iodine, calcium, lipid, and water that used QA phantom with CZT-Medipix3RX detector. Mass attenuation value of lipid and water in scan-2 is slightly higher at 7-18 KeV but scan-1 is far from than other scans in case of water.

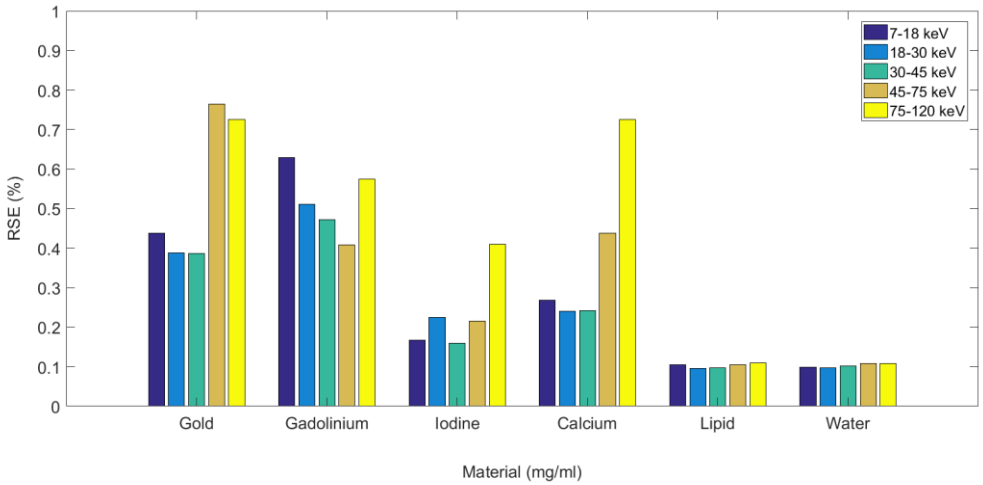

Figure 3.11 The intra-scan variation of mass attenuation of different materials at different energy bins within any particular scan. Fourth and fifth energy bins show the higher value of RSE of gold, gadolinium, iodine, and calcium than lipid and water.

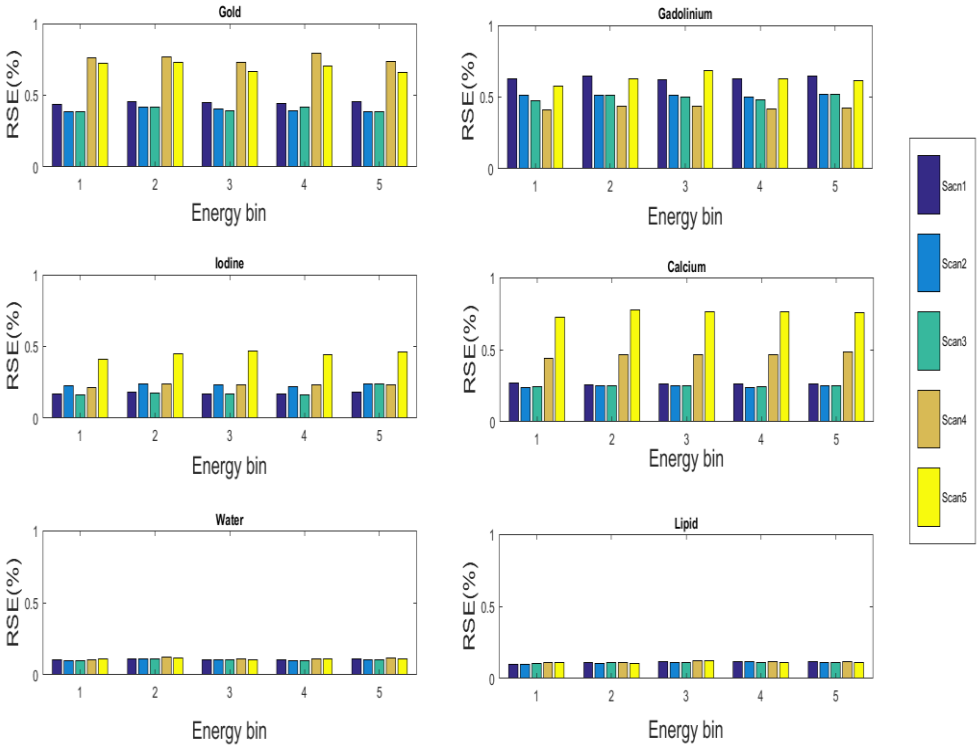

Figure 3.12 Inter-scan variation of mass attenuation of different materials at different energy bins in the different scan.

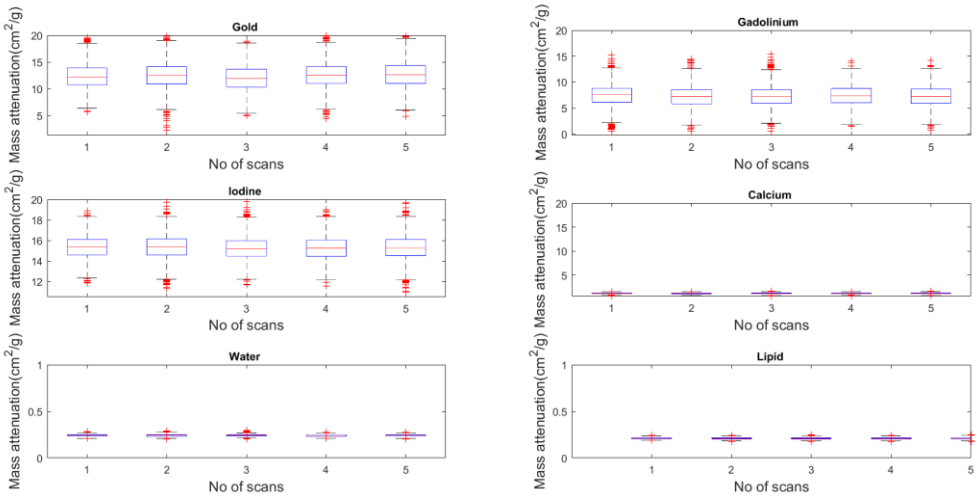

Figure 3.13 Boxplot of the mass attenuation coefficient of different materials in each energy bins of different back to back scan. Legend: inside the box, the red line represents the median (50th percentile). Gold, gadolinium, and iodine show the significant outlier at the top and bottom of each box plot that represents the error due to changes in system behavior, instrument error or simply through natural deviations in populations. Hence, composite materials show significant outlier in each scan than lipid and water.

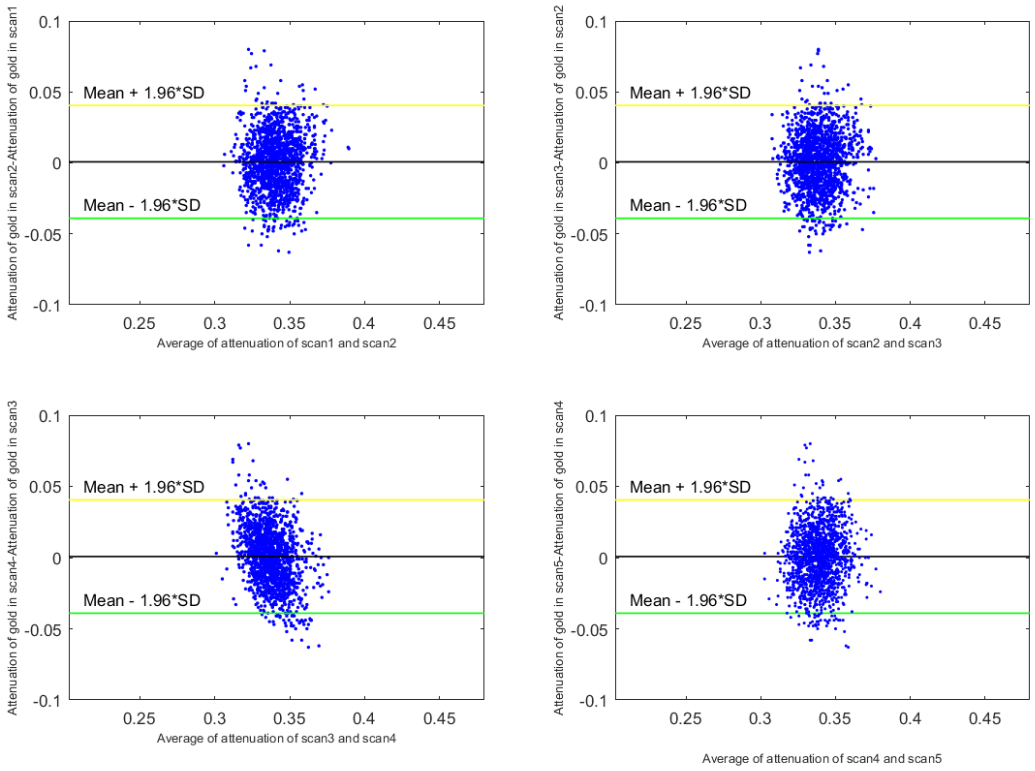

Figure 3.14 Bland Altman plot for gold in the different scan at lower energy bin.

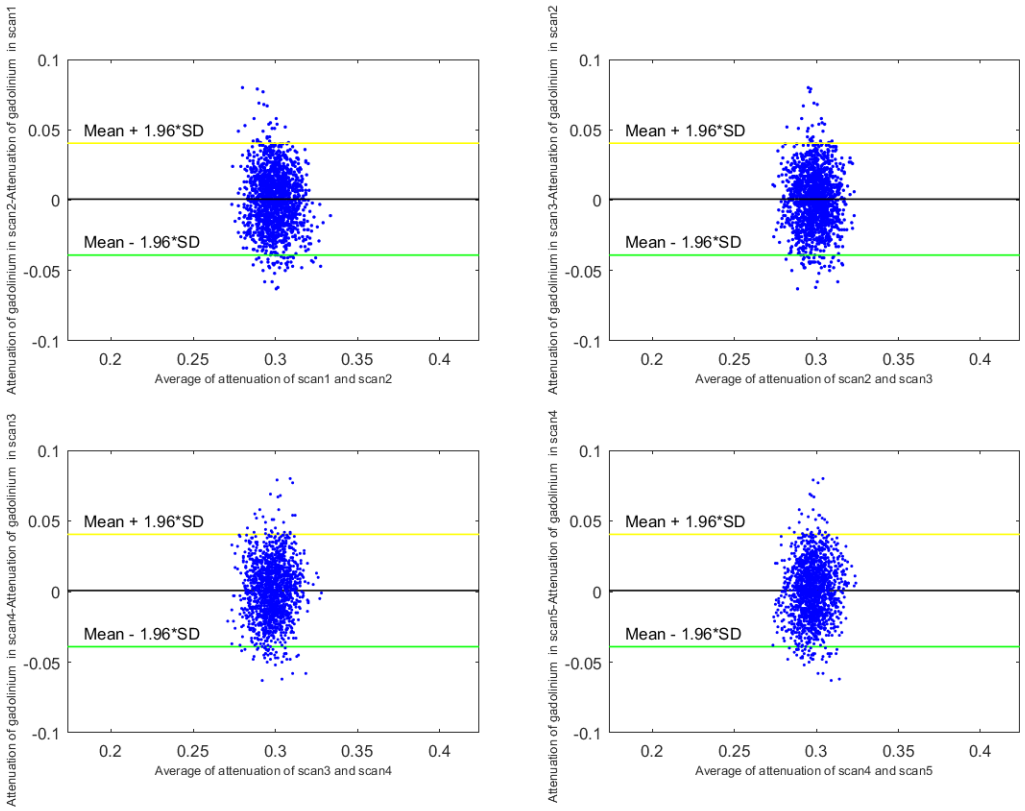

Figure 3.15 Bland Altman plot for gadolinium in the different scan at lower energy bin.

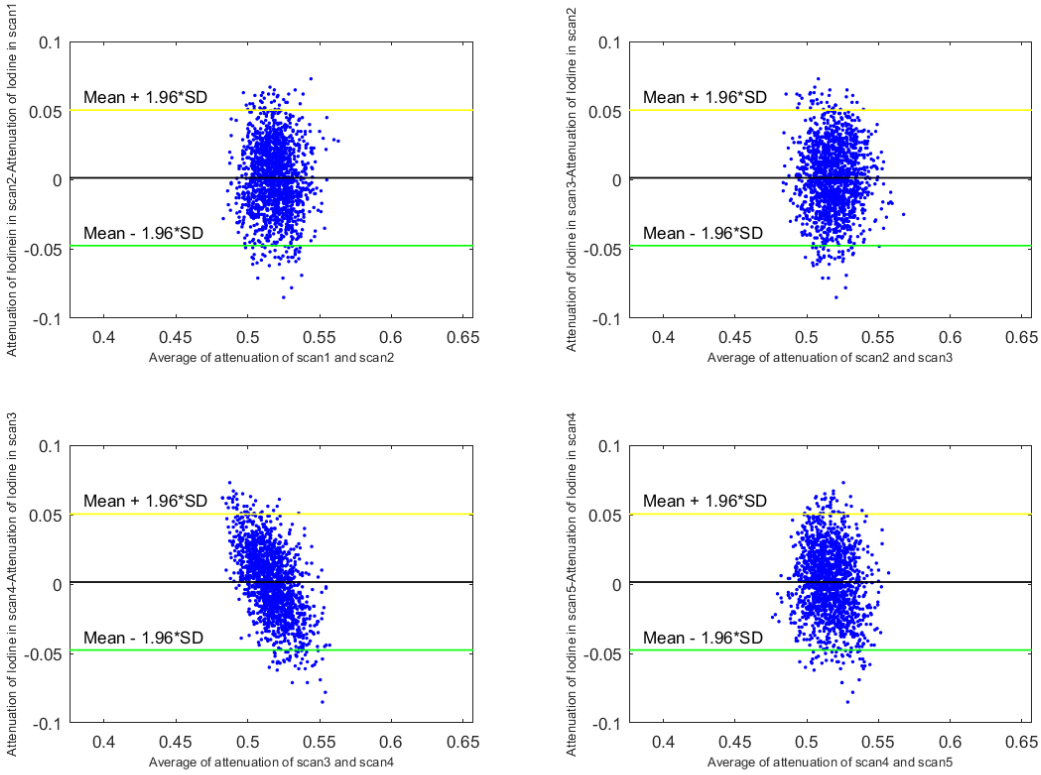

Figure 3.16 Bland Altman plot for iodine in different scan at lower energy bin.

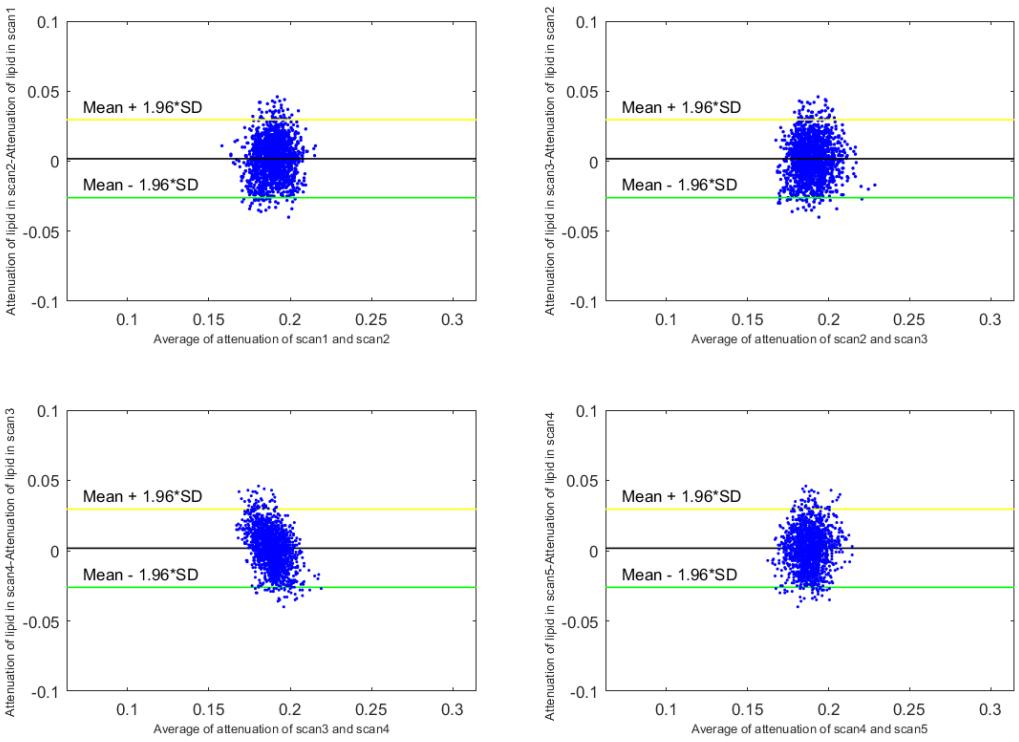

Figure 3.17 Bland Altman plot for lipid in the different scan at lower energy bin.

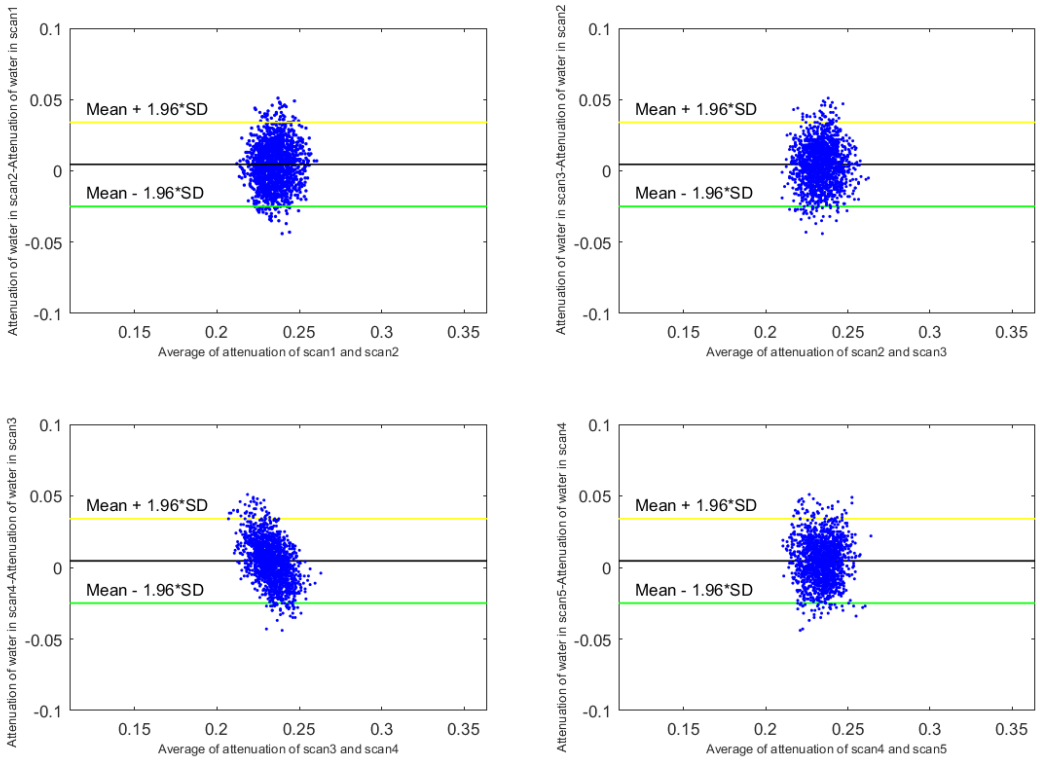

Figure 3.18 Bland Altman plot for water in different scan at lower energy bin.

3.6 Discussion

This study demonstrates the characterization of intra-scan and inter-scan measurement variation of the measured spectral signals from different composite and single materials using different protocols and different MARS cameras. Three experimental studies were performed to monitor the variation of the mass attenuation coefficient of composite materials such as gold, gadolinium, iodine and calcium and single materials which are lipid and water.

The variation of mass attenuation coefficient was assessed by the relative standard error. In general, the results of the study show that the mass attenuation coefficients of lipid and water have less variations as compared to calcium, gadolinium, iodine, and gold. For the composite materials, the measurement of the mass attenuation profile is influenced by the inverse noise amplification as compared to the single materials. The noise involved in the calculation of mass attenuation coefficients ($x = A^{-1}b$), originates from the uncertainties of the scan measurements, inaccurate threshold setting between the K-edge, geometric misalignment etc. The uncertainties of the measurements include statistical noise, beam hardening, the artifact from material reconstruction algorithms, output variation of the x-ray source, and energy threshold drifting in the detector. The superposition of such uncertainties from each material in a solution such as water and gold caused higher variation of mass attenuation coefficient in a composite material than water or lipid.

The higher variation of the K-edge materials is thought to be due to energy threshold drifting. In the worst case scenario, the K-edge may be captured in the adjacent energy bin which is more likely when a large threshold variation exists in the detector's channel. Comparison of the RSE values across all studies also indicated that the measurement variation of the first study is higher than the second and the third study. This study also showed once the same materials were scanned under the same protocol, but using the GaAs-Medipix3RX camera, the measurement variation at each energy bin significantly decreased (i.e. the maximum RSE values of 11.2% in the first study dropped to approximately 2% in the second study). This results can imply that the MARS camera used GaAs sensor layer behaved more consistently during the measurements as compared to the camera using CZT.

The results of the third study expressed less variation in measurement as compared to the first and second study. In this set of measurements, the same QA phantom was scanned while using a different scanner (MARS-11) equipped with CZT-Medipix3RX with the higher tube voltage (120 kVp). This resulted in producing more photons and reducing the statistical noise in the measurement as compared to the results of the first and second study.

In addition, the maximum measurement variation is seen in the last energy bin of the third experiment (75-120 keV). This could be due to the low photon count in this energy range and as a consequence, more statistical noise. The temperature is also one of the effective parameters on the measurement variation which need more investigation in future.

The important challenge in the development of photon-counting spectral CT is that the location of the energy thresholds tends to vary among detector elements. Threshold variation or drifting leads to ring artifact in the reconstructed images. Inhomogeneity of the detector element is another challenge of photon-counting spectral CT. It is not feasible to produce readout electronics with completely identical components in different readout channels,

meaning that there will be variation between detector elements. The result of these effects is that the energy thresholds vary between detector elements. Some detector elements count more photon than others and photons with the same energy are registered in different energy bins in different detector elements due to the threshold variation [43].

In general, all high-Z materials have significant K-edge properties and therefore, are sensitive to select appropriate energy threshold above or below the K-edge. K-edge image contrast with spectral CT depends on the specifications of the two energy bins on both sides of a K-edge in the attenuation profile of a relatively high atomic number material [44, 45]. Due to the misadjustment of energy threshold especially for K-edge materials might lead to inverse noise amplification that produces significant measurement error in case of all K-edge materials.

In conclusion, this study established and investigated the method to evaluate the systematic measurement variation in different MARS scanner during repeated scan. Such inter and intra-scan variation needs to be investigated on material decomposition algorithm in future. To control the measurement variation and identify the level of the error for our spectral CT system, geometric calibration and the impact of geometric parameters on the reconstructed images were investigated which is covered in chapter 5 to 6.

3.7 Summary

- The studies reported in this chapter utilized in different MARS scanners to characterize the intra and inter-scan variation of mass attenuation of different materials from the reconstructed image using different protocol setting and a multi-contrast phantom.

- Characterization of measurement variability is necessary to determine the sources of instability in MARS scanners to understand abilities and limitations with regard to image quality and material identification and quantification.

- Several factors contribute to the variation in measured spectral signal of materials. Examples of these include geometrical misalignment of scanner components, inter-pixels difference, changes in detector temperature, energy threshold drifting and

detector instabilities. These types of instabilities can severely degrade image quality that produces measurement variation.

- The inter and intra-scan measurement variation of mass attenuation of different materials was assessed via the relative standard error. The Bland-Altman method was applied to measure the proportional bias during different back-to-back scans.

- The results of all studies show that measurement variation was more likely for composite materials such as gold, gadolinium, and iodine this is due to the inverse noise amplification that occurs with these materials.

- The limit of agreement was measured to determine proportional bias in different measurement by the Bland-Altman method. Lipid and water show between agreements than composite materials in different measurements.

4 Geometry of MARS scanner

4.1 Introduction

This chapter explains the geometry of the MARS scanner. The aim of this chapter is to understand the geometry of the key components such as the gantry, x-ray source, and camera. The optimal imaging performance of the MARS spectral scanner is achievable when its geometric parameters are accurately characterized and correctly incorporated into image reconstruction software, resulting in maintaining the spatial fidelity of the images and improving material quantification. Section 4.2 explains the main components of the MARS scanner. Section 4.3 introduces the required coordinate system of MARS scanner to simplify the geometric analysis in a systematic way. The geometry of the beam is explained in section 4.4. The path ray through voxels is explained in section 4.5. The algebraic reconstruction technique is explained in section 4.6. A detailed description of the polychromatic forward model is discussed in section 4.7.

4.2 MARS scanner components

The current version of the MARS scanner is manufactured for small animals and human excised specimens. The maximum field of view is 100 mm in diameter and 270 mm in length. Two MARS components are an x-ray tube to generate a narrow cone beam, and a camera to detect the photons passed through the subject (e.g., an object, an excised specimen, a live or plasticized animal, or human). These components are mounted in a mechanical housing called a gantry which rotates around the subject on a fixed axis. The subject is mounted on a holder that is translated perpendicular to the gantry rotation to cover part or all of the subject during a scan (Figure 4.1). The camera includes an array of fingerboard Medipix3RX chips, each of which is attached to a transition board and a readout board in (Figure 2.5). The camera can be translated along the tangential axis of the gantry to cover samples with large diameters. The gantry and sample holder have two independent systems, resulting in minimization of their negative influence on each other such as vibration between the two systems. Additionally, the x-ray tube and camera have two separate magnification tracks (Figure 4.2) which make geometrical alignment of the scanner more complex.

The x-ray source and camera can be translated radially to adjust the distance from the source to axis distance (SAD), and distance from the rotational axis to the detector distance (ADD), respectively. In the ideal case, the camera and x-ray source are aligned and the central ray passes through the rotational axis. However, the orientation of the x-ray tube and camera as well as each chip in the detector array, may tilt or skew, which are sources of geometric

manufacturing error [20]. It is necessary to accurately calibrate the geometric offset parameters through a systematic way.

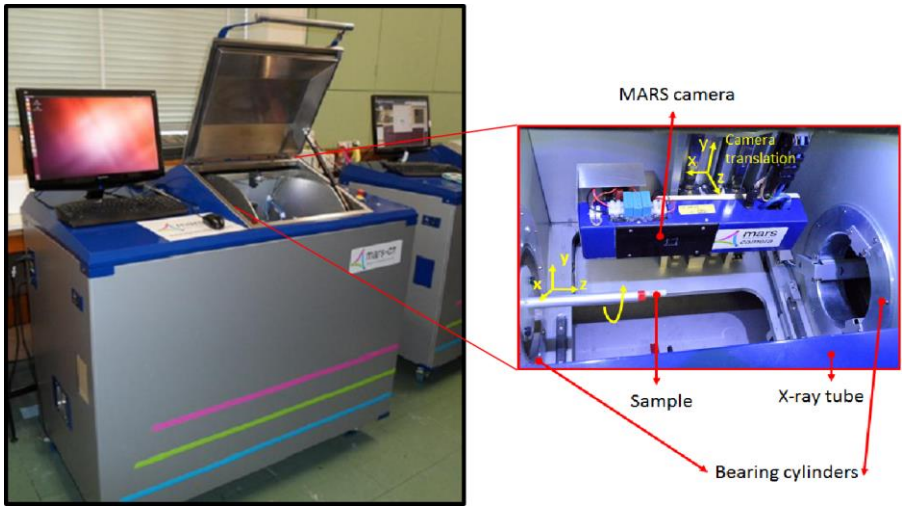

Figure 4.1 A small bore MARS spectral scanner. The magnified image (right) shows the x-ray tube, camera, and sample inside the gantry. The x-ray source and camera are mounted on the gantry that rotates around the subject *[46]*.

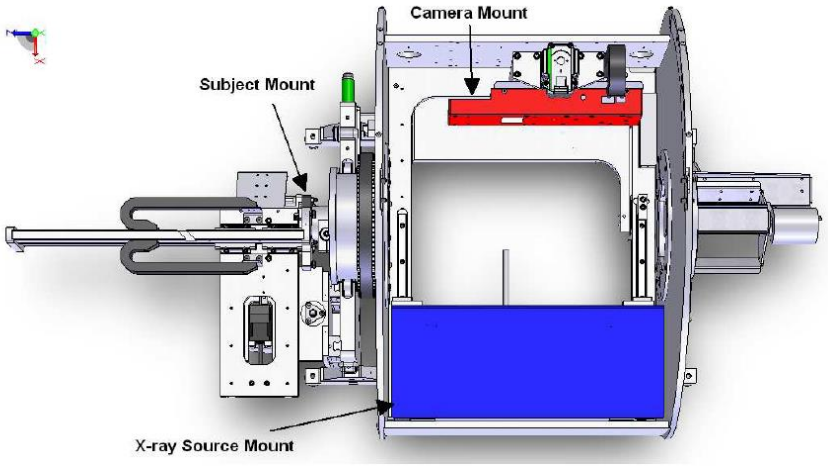

Figure 4.2 A schematic view of the gantry showing the subject, x-ray tube, and camera mounts [47].

4.3 Coordinate system of MARS scanner

The MARS scanner involves different sub-system associated with the x-ray source, subject or sample, and the MARS camera. For each sub-system, it is helpful to define a set of independent axes, referred to the coordinate system of the sub-system. The parameters measured with respect to the coordinate system are then passed to the image reconstruction algorithm. Incorporation of accurate geometric parameters into the reconstruction improves spatial resolution. In this section, the definition of the coordinate system for the whole MARS system in the laboratory frame of reference is established before moving to the gantry frame of reference. Afterward, this a system further split to the subsystems to define their corresponding coordinate references. These subsystems are the subject and subject bed, the x-ray source, camera, detector mounting plate and Medipix chip as demonstrated in Figure 4.3.

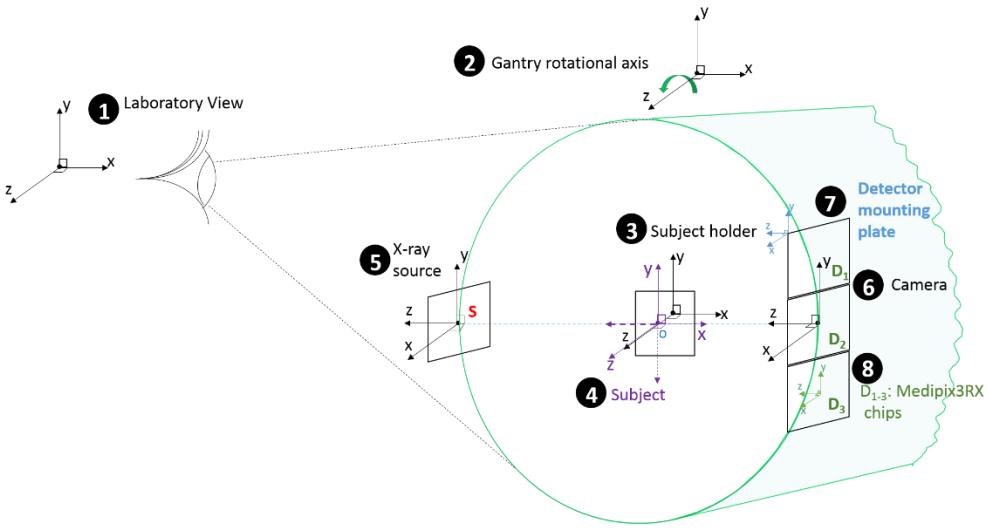

Figure 4.3 Schematic diagram of all corresponding coordinate system of MARS scanner. (Image courtesy: Dr Marzieh Anjomrouz)

4.3.1 Laboratory coordinate system

The laboratory frame of reference or the scanner coordinate system is defined in which the whole system is seen the user's point of view and all measurements are performed in this frame of reference. For a user standing in front of the MARS scanner with the lid open and the rotating gantry in its load position, the laboratory coordinate system is the right-handed coordinate system and the origin is located at the left-hand side bearing cylinder (Figure 4.4 and Figure 4.5). The x-axis is horizontal and increases as a point moving away from the operator. The y-axis increases vertically, and the z-axis increases to the operator's right. The z-axis is also known as the rotation axis [17].

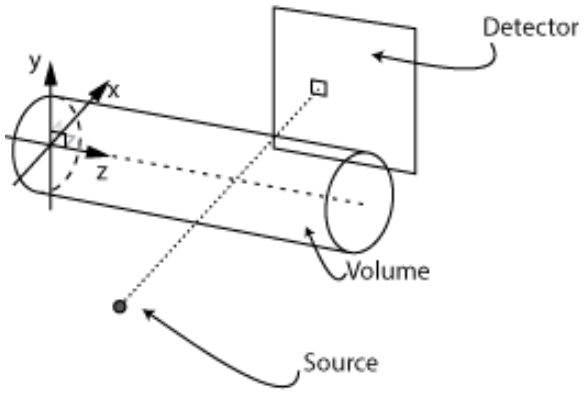

Figure 4.4 The lab or scanner system axis with right-handed (x,y,z) coordinates and an origin at the center of the rotating gantry. This coordinate system does not move relative to the lab.(Image courtesy: MARS Bioimaging)

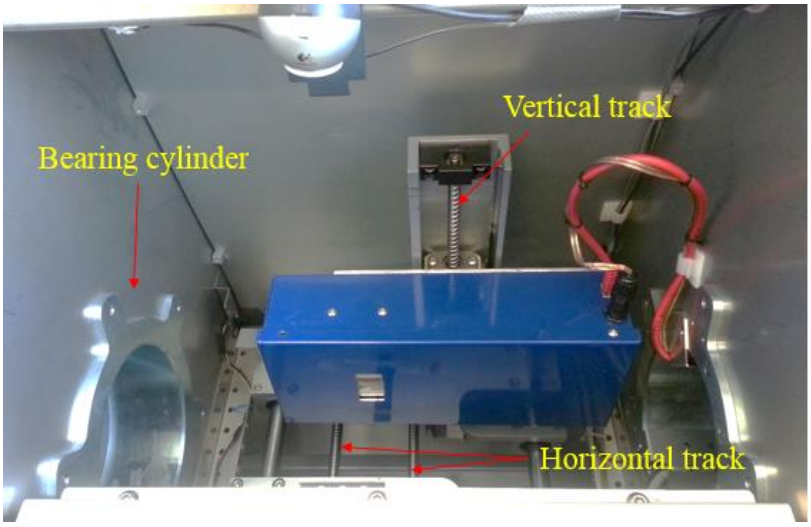

Figure 4.5 Bearing cylinder and moving track of gantry and camera.

4.3.2 Gantry coordinate system

The gantry coordinate system describes the relative positions of source and camera that are movable but fixed to the gantry. The origin of this coordinate system is on the left-hand side bearing cylinder which is the same as the lab coordinate system. Its z-axis is also is the same as the lab coordinate systems, but its x and y axes are only the same if the bottom tracks are positioned horizontally (i.e. parallel to the floor) as shown in Figure 4.5.These tracks are used to control the radial distance of the camera and the x-ray source with respect to the rotational axis. During the gantry rotation, the x and y axes rotate so that the source remains on the -x-axis, and the camera remains in the +x direction.

The subject moves horizontally along the z-axis during a spiral scan, while both the x-ray source and camera rotating around it. This cartesian coordinate system of the gantry is shown in Figure 4.6a. The gantry which has a cylindrical shape is also adapted in the cylindrical coordinates system as shown Figure 4.6b.

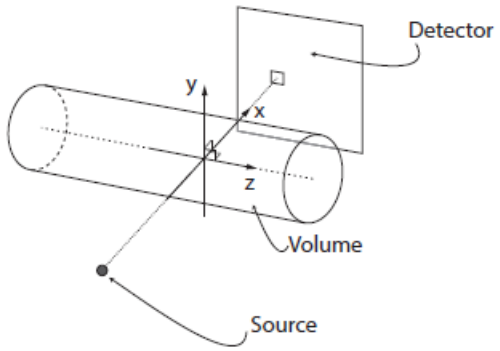

(a) Cartesian coordinates, right-handed (x, y, z) axes

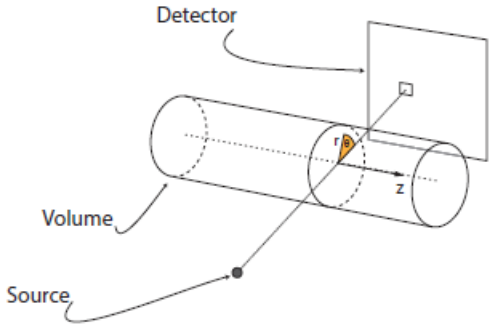

(b) Cylindrical coordinates using (angle, radius, z)

Figure 4.6 Gantry view in the Cartesian and cylindrical coordinate systems. (Image courtesy: MARS Bioimaging)

4.3.3 Subject coordinate system

Many subjects such as multi-contrast phantoms, mice, and excised human or tissue etc have natural and conventional orientations. In the case of the multi-contrast phantom, which is attached to the subject holder, moves along the z axis and perpendicular to the x-y plane (Figure 4.1).

The mouse coordinates are used at very last stage of the reconstruction and material decomposition of a scan, resulting in an image that is presented to the user in the conventional orientation for standard dicom viewers. Figure 4.7 shows the direction of the axis depends on which end the mouse's head is, and whether the mouse is face up or down. In all situation, the z-axis is cosidered at the mouse's tail and move in the positive direction towards the mouse's head. The x-axis will be positive in the direction of the mouse's right arm and the y-axis is positive moving away from the mouse's chest. The origin is set near the mouse's tail. The software can be informed of the mouse's orientation with stick figure drawing that the user selects to match the orientation of the mouse. The change from volume coordinate to mouse coordinate is implemented after reconstruction [17].

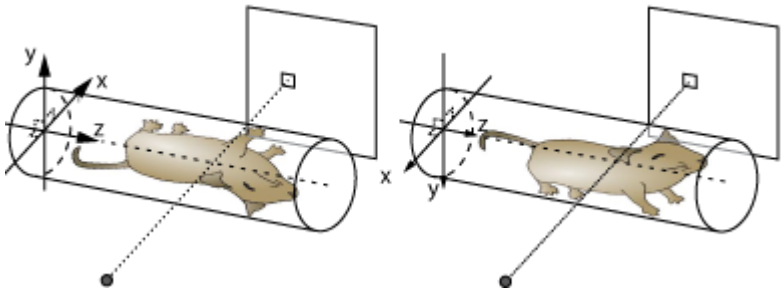

Figure 4.7 Mouse axes with (x, y, z) coordinates. The origin is near the tail of the mouse, the x-axis the right side the y-axis from the chest and the z-axis points towards the head. (Image courtesy:MARS Bioimaging)

4.3.4 Subject bed coordinate system

This coordinate system is similar to the lab coordinate system, in which the origin is at the left-hand side bearing cylinder. The sample bed moves along the z-axis. In this system, the subject remains stationary as the bed is moved during a spiral scan, while the camera and source rotate around the z-axis in Figure 4.8.

4.3.5 X-ray source coordinate system

The x-ray tube is located in a cubic box which is mounted on the gantry (-x-axis) while moving radially towards the rotational axis. The radial axis of the source is along z-axis which is parallel to the camera (Figure 4.9). The origin of the x-ray source coordinate system is assumed to be at the focal spot on the anode when the source box is located at its maximum distance with respect to the subject and the camera in which the source box touches inside of the gantry cylinder. The y-axis is the same as the subject y-axis. However, its x- and z-axes are inverse to the subject coordinate system.

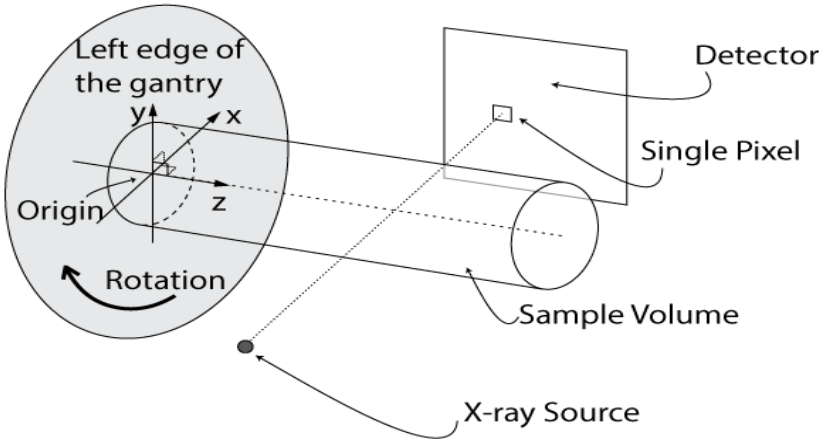

Figure 4.8 The axes for the subject bed with right-handed (x, y, z) coordinates.(Image courtesy:MARS Bioimaging)

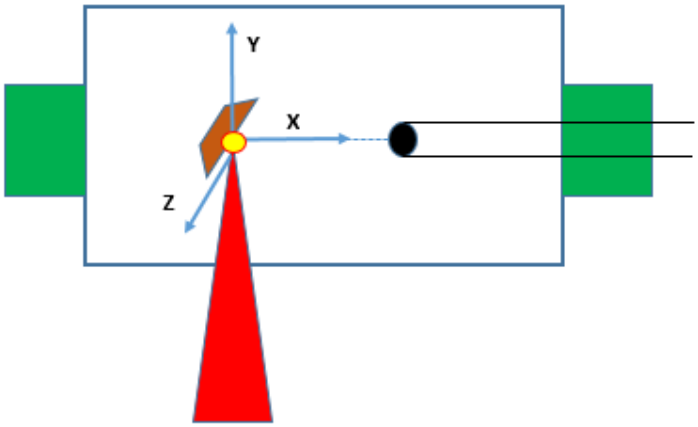

Figure 4.9 X-ray tube coordinate system.

4.3.6 Camera coordinate system

The Medipix detector array along with the corresponding transition boards and readout chips are located in a cubic box which is mounted on the gantry (+x-axis) while moving radially perpendicular to the rotational axis and tangentially around the rotational axis. The radial movement of the camera is along the z-axis and its tangential movement are along y-axis. The axes of the camera coordinate system are parallel to the coordinate axes of the x-ray source. Figure 4.10 shows the origin of the camera coordinate system, which is assumed to be at the camera window when the camera box is located at its maximum distance with respect to the subject and the source box in which the camera box touches inside of the gantry cylinder.

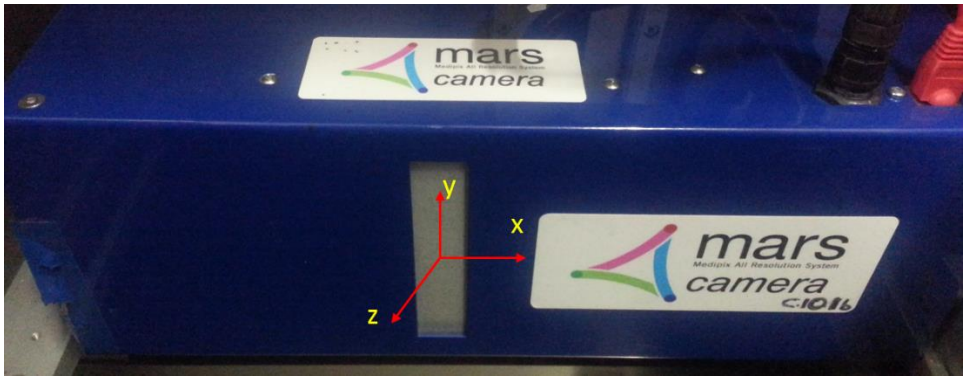

Figure 4.10 MARS camera coordinate.

4.3.7 Detector mounting plate coordinate system

The MARS camera box includes either a single detector chip or multiple detector chips. The coordinate system used to control the alignment of each chip in the detector array is located at the top left corner of the top chip as shown in Figure 4.11 on a flat field image acquired from a MARS camera with three CZT-Medipix3RX chips.

One of the detector mounting plates designed for a three-chip camera is shown in Figure 4.13. The chips are mounted on an uneven mounting plate due to manufacturing limitation at that time (i.e. to make enough space for corresponding transition boards). For such a mounting plate, the initial position of z is, therefore, set to each chip specifically. As example an three-chip camera in which the z value of the central chip is set to 0 and z values of the top and the bottom chips are set to $\pm 3.5\ mm$, respectively as shown in Figure 4.12. To control the chip positions along x, y and z, the appropriate values are set into the camera mechanical configuration file.

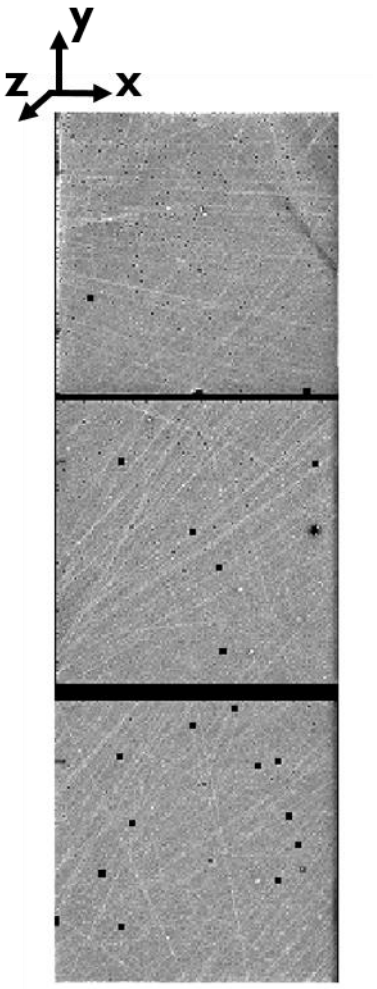

Figure 4.11 A projection image acquired from a MARS camera with three CZT-Medipix3RX chips.

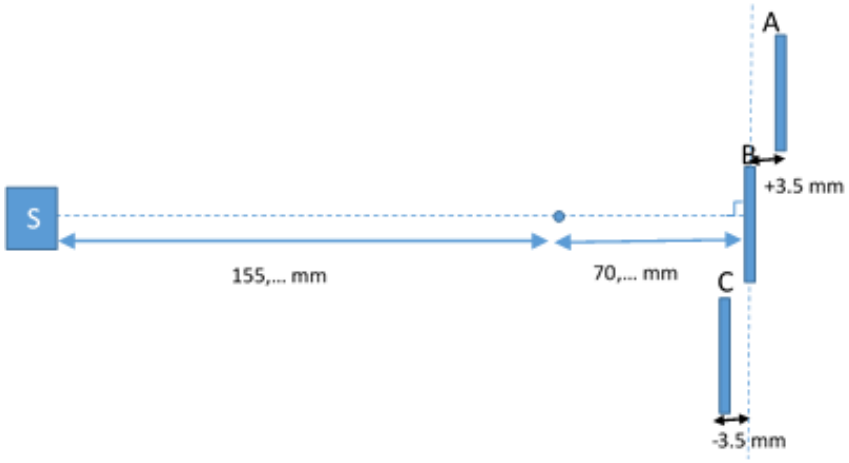

Figure 4.12 A schematic diagram of MARS camera with three chips.

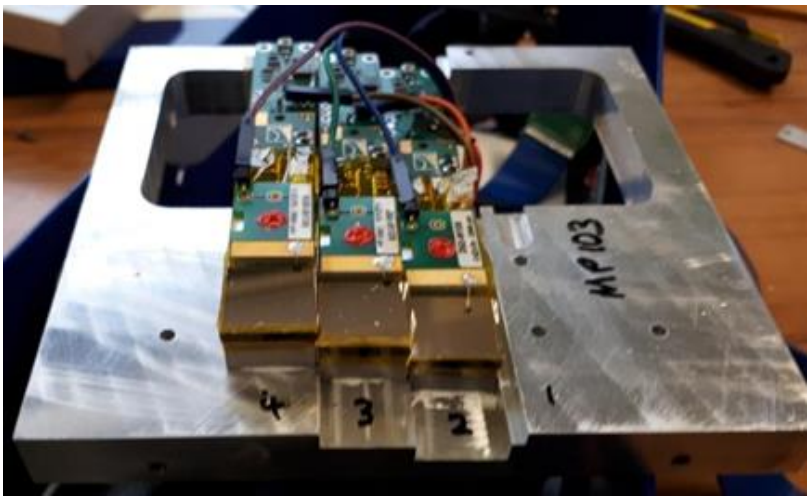

Figure 4.13 Detector mounting plate incorporates Medipix chip.

4.3.8 Detector chip coordinate system

A Cartesian coordinate system is also defined for each Medipix3RX chip with its origin assumed to be at the center of the chip Figure 4.14. In this manner, each pixel in the pixel grid of 128×128 can then be addressed with respect to the origin of the chip coordinate system. The main usage of this coordinate system is in the pixel characterization study when reference to a given pixel in a Medipix3RX chip is necessary. For instance, as a result of electric field distortion within the sensor layer, an effect occurs called “charge steering". In this case, measuring the changes in the position and the area of each pixel in the chip is required.

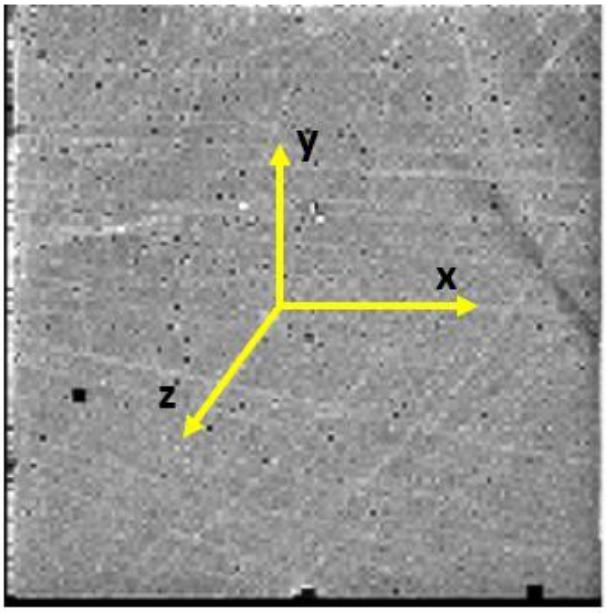

Figure 4.14 Schematic diagram of pixel array Medipix chip.

4.4 Definition of the beam geometry

The x-ray beam in MARS scanners come from polychromatic x-ray source that passes through the object and hits the pixelated Medipix3RX detector. The x-ray source has a small focal spot with a diameter of 50 μm, and the pixel is typically square with side of 110 μm. Therefore the path of the photons in a single beam can be illustrate in Figure 4.15.The geometry of the ray in MARS scanner is dependent on the position of the source and position of the pixel that goes from the geometric centre of the source to the geometric centre of the pixel. The direction of the beam and pixel position are refered to as r and p.

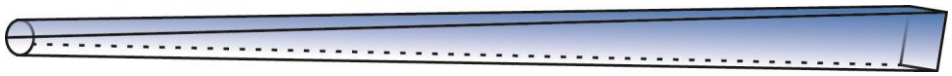

Figure 4.15 A beam from circular source to a square pixel, but where the square is, in general, at an oblique angle.(Image courtesy:MARS Bioimaging)

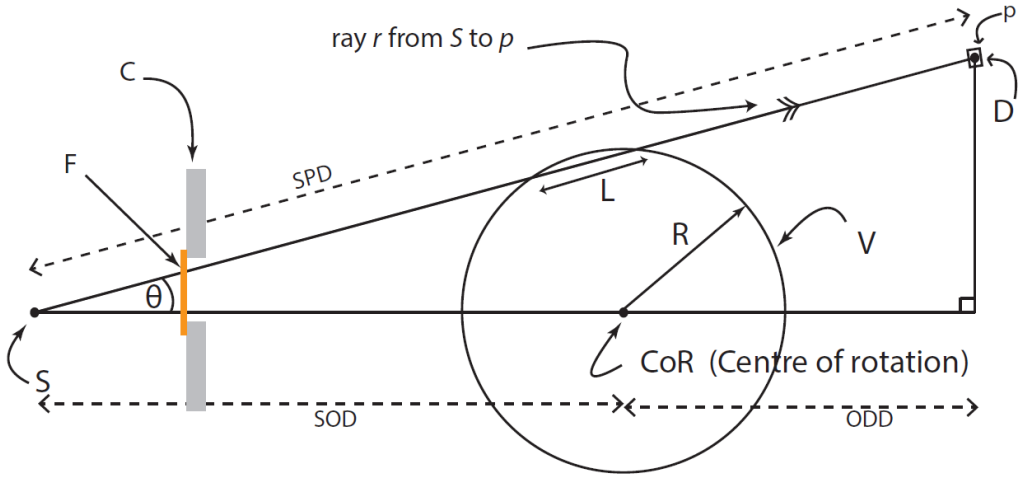

Figure 4.16 CT geometry showing source S, collimators C, filter F, volume V and a pixel p. The beam is defined as the collection of rays from the source S to the detector pixel p. The central ray r in the beam passes through length L of the volume V.(Image courtesy:MARS Bioimaging)

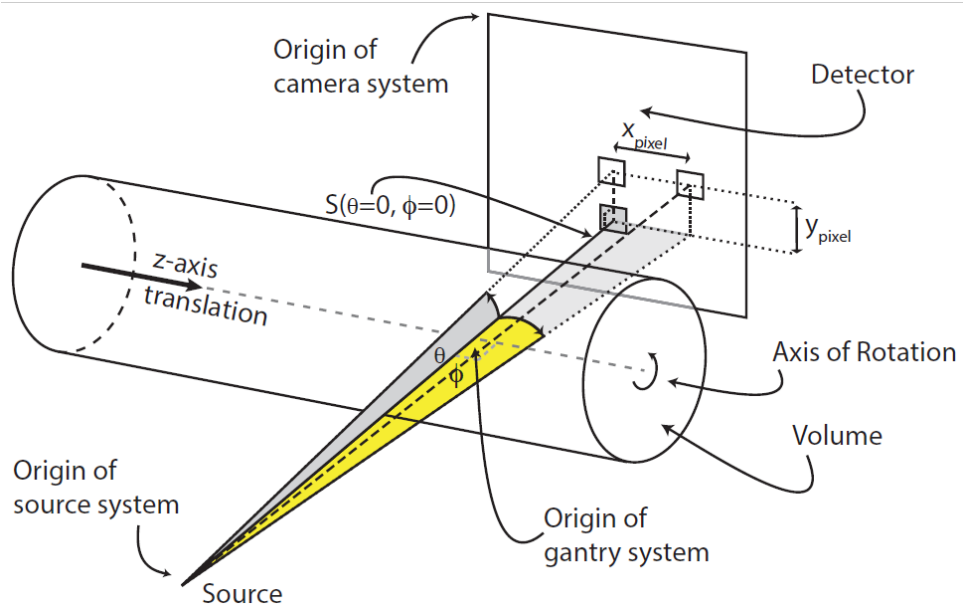

Figure 4.17 A 3D view of the CT geometry showing the source, volume and detector, the x-axis, plus the central ray r of the beam from the source to the pixel p. The ray r is described by the angles θ and ∅.(Image courtesy:MARS Bioimaging)

The ray r is at angle θ to the x-axis of the gantry frame, as shown in Figure 4.16 and at an angle ∅ towards the head end of the sample bed Figure 4.17. The rays that must be considered are those that originate at the source, and end at the centre of a pixel that is utilised in an image taken during a scan. To specify the values of θ and ∅, it is necessary to know the position of the camera, the detector chip number within the camera, and the pixel (row, column) values. The camera position is given by the motor positions, both the vertical position along the y-axis and the horizontal position (front to back) along the x-axis. The detector chip number will give a displacement for the origin of this chip relative to the camera position. Finally, the *row* and *column* values give the relative position of the pixel to the chip "origin".In a MARS scanner the source and detector are rotated by angles α around the centre of rotation of the scanner axis represented by a point CoR in the 2D Figure 4.16 and by the a line in the 3D representation Figure 4.17. In a helical scan the object is, at the same time, moved relative to the x-ray source and camera by translating the sample bed in the along to z-axis.

4.5 Path of a ray through voxels

The volume of the object being scanned is theoretically enclosed in a cuboid (a box) that has been divided into small cubes called voxels (the 3D version of a pixel). Although the gantry rotates around the object, we can view this from the perspective of the gantry, and have the object rotating around the z-axis. The specific voxels that the ray passes through and the length of the ray in each voxel will depend of the angle α that the gantry has rotated (Figure 4.18).

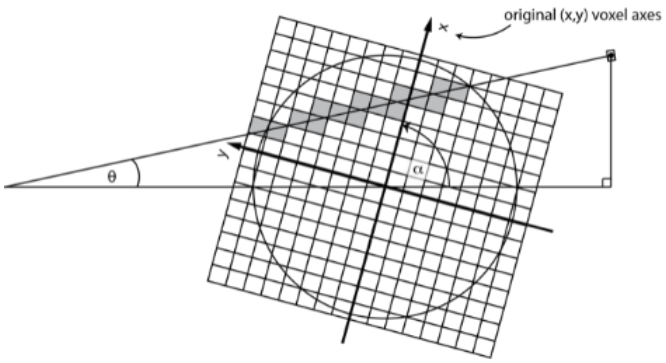

Figure 4.18 The voxels traversed by the ray, and the length within a voxel, depend on the angle of rotation α of the gantry.(Image courtesy:MARS Bioimaging)

4.6 Algebric reconstruction technique in MARS

The algebraic reconstruction techniques (ART) are a class of iterative algorithms used in computed tomography. Algebraic Reconstruction Techniques are a type of mathematical iterative algorithm used to reconstruct objects from the projection images. These reconstruct an image from a series of angular projections (a sinogram). Gordon, Bender, and Herman first showed its use in image reconstruction [48] whereas the method is known as Kaczmarz method in numerical linear algebra. ART can be considered as an iterative solution of a system of linear equations

$$Ax = b \tag{4.1}$$

The projection data is the known information, while the CT image is unknown and thus needs to be reconstructed. This technique is achieved by initializing a system of linear equations for these projections, defined by

$$-\ln\frac{I}{I_{\circ}}=\sum_{v}\mu_{v}l_{v} \tag{4.2}$$

Where, v is the voxel index and projection data is summed over all the voxels. The term l_v refers to the path-length of the projection ray passing through the voxel.This can be interpreted in the form of a linear matrix (4.1) where matrix **A** corresponds to the path-length coefficients, **x** is a vector of the linear attenuation coefficients to be reconstructed, and vector **b** contains the projection data [49].

$$\begin{pmatrix} l_{v1}^{ray1} & l_{v2}^{ray1} & l_{v_vN}^{ray1} \\ l_{v1}^{ray2} & l_{v1}^{ray2} & l_{v_vN}^{ray2} \\ l_{v1}^{ray3} & l_{v1}^{ray3} & l_{v_vN}^{ray3} \end{pmatrix}\begin{pmatrix} \mu_{v1} \\ \mu_{v2} \\ \mu_{v3} \end{pmatrix}=\begin{pmatrix} p^{ray1} \\ p^{ray2} \\ p^{rayN} \end{pmatrix} \tag{4.3}$$

To solve this system of linear equations, a single row from the path-length matrix is used at any given time. From an initial approximation of the object $x^{(k)}$, the iteration process goes through a sequence of updates, propelling the CT image toward a complete and accurate representation of the object that was scanned. The next $x^{(k+1)}$iteration is given by

$$x^{(k+1)}=x^{k}+\frac{b_j-A_jx^{(k)}}{\left\|A_j\right\|^2}A_j^T \tag{4.4}$$

4.7 Forward model

The issue with the current MARS data processing chain is that it is based on techniques which assume the polychromatic x-ray source used in MARS emits a monochromatic x-ray beam. Already this assumption has been made in conventional CT scanner that leads to beam hardening artifacts. MARS research group has been trying to solve this problem by developing a polychromatic material reconstruction algorithm. This task is still progressing through the initial development phase, with various members of the MARS team working on different components of the problem [11].

To resolve this problem, a forward model that include feature several components of the MARS scanner has been established. The reason for doing this is to transform monochromatic materials reconstruction into polychromatic reconstruction model. The actual number count in a particular measurement.

$$Q_{cr} = \int_{E_{THL}}^{E_{KVP}} F_{er} C_{er} D_{er} S_{er} \exp^{-\int_{d_{source}}^{d_{detector}} \sum_m \mu_{em} X_{vm} dd} de \tag{4.5}$$

Where, Q_{cr} is the measured photon count at the central ray. F is the filter. A scan is carried out by using a source S of x-ray photons in the energy range of 20 to 120 keV; the photons travel in a beam towards an object; some pass through the object in volume v; and these photons are detected with detector D; and then algorithms determine which materials m are within each voxel v of the object. The filter F, the collimators C, and the geometry D are currently being investigated by other team member.

The forward model not discussed in detail physics based model for estimating predicted count at the detector. The predicted count depends on the geometry of the source that directly connected to the geometry of the pixel with respect to the central ray. Reconstruction methods utilizing the forward model approach are current in development. The method depend on accurate information for scanner parameters, geometric setup and detector setting etc.

The geometry of the source need to be calibrated to know spatial photon distribution with respect to the central ray in this regard. To be successful of polychromatic forward model an appropriate assumption needs to be made that will provide the equal value of estimated and measured count with respect to the central ray for particular voxel selection.

4.8 Summary

- In computed tomography, a sufficiently accurate knowledge of the tomograph geometry is required to achieve good quality image reconstruction.

- For optimal imaging performance of the MARS spectral scanner, geometric parameters must be accurately characterized and correctly incorporated image reconstruction software.

- The camera and the source are placed on the gantry from the opposite sides and are able to move along the axis connecting each other, approaching or moving away from the sample.

- In MARS spectral CT, the x-ray source and camera can be translated radially to adjust the distance from the source to the rotational axis (SAD), and distance from the rotational axis to detector plane (ADD), respectively.

5 A preliminary workflow of the spectral image library

5.1 Introduction

This chapter describes the development of a spectral image library for MARS scanners. In this work, a preliminary workflow was developed to create an image library using multicontrast phantoms that include different materials. The reason for doing this work is to investigate the spectral image quality of the MARS in MARS scanners. In this study, also discussed the relationship between geometric information and the energy information and implication for materials reconstruction. To see the spatial error on the reconstructed image, this work is motivated to create an image library containing artifacts by perturbing selected parameters of the scanners. Initially, camera axial and tangential offset were perturbed with different values and it was observed that how spectral signal from different materials is being degraded under the effect of the geometric perturbation. This chapter will provide useful insight to develop a geometric calibration method to reduce the spatial image error (As it is discussed in chapter 6).

An important concept revealed by this study is that the image quality degradation in the energy domain is linked to that in the spatial domain, and vice versa. Consequently, if there are spatial artifacts in the reconstructed images, there will be a corresponding distortion in the energy information. The image subtraction technique was used in the study to highlight differences. Different anatomical image planes such as (axial, sagittal and coronal) of the multi-contrast phantom are illustrated to see the visual interpretation of spatial image error on the reconstructed image in a different slice at different energy bins.

5.2 Significance of image artifact

The medical diagnostic is a very complex process that sometimes biased by the different error that is related to the different sources of the scanner instability. Since the computed tomography imaging is widely used, it is a potential source of error in diagnostic imaging. Missed or delayed diagnoses often lead to patient harm and missed opportunity for treatment [50]. Although some diagnoses may be missed because of technical or physical limitations of the imaging modality, most missed radiologic diagnoses are attributable to image

interpretation errors by radiologists [51]. The retrospective error rate among radiologic examinations is approximately 30%, with real-time errors in daily radiology practice averaging 3-5% [52]. Nearly 75% of all medical malpractice claims against radiologists are related to diagnostic errors. In the case of spectral CT, image are more sensitive with respect to the different scanner components and therefore image errors like blurring or ring artifacts produces spatial and spectral distortion that degrade the quality of the signal to noise ratio. These artifacts can lead to misdiagnosis and need to be eliminated and corrected before spectral CT can be used clinically.

5.3 Sources of image error in MARS scanner

Image error or artifact are a common issue in medical imaging that can lead to problems in proper diagnosis. An error is a distortion or artifact in an image that is unrelated to the subject being imaged. The image in the MARS scanner arises from a different number of sources, including geometric misalignment, miscalibration of the detector elements, inconsistency in measurement due issue in the reconstruction process. Three types of image error in MARS were identified and investigated as part of this study.

5.3.1 Spatial image error

Spatial image errors are related to the misalignment of scanner components. The spatial resolution of the MARS scanner is very sensitive to the proper alignment of the x-ray source, object, and detector. In a MARS scanner, the x-ray beam passes through the object in multiple views and is detected by small multiple detector elements. Therefore, a small geometric misalignment between x-ray source, object and camera causes an error in the reconstructed image that limits the capability of MARS scanner in material identification and quantification. The main sources of spatial image error are produced from inaccurate camera tangential and axial offset, source tangential and axial offset, magnification, and skewness of the camera and the gantry. In this study, the impact of camera axial and tangential offset on the reconstructed images were investigated.

5.3.2 Spectral image error

The main sources of spectral image distortion are pulse pileup, charge sharing, inaccurate energy response, incomplete charge collection, and threshold dispersion. MARS scanners incorporate a photon counting detector, therefore, the energy resolution of each pixel is very important to get a high-quality image. Poor calibration of the detector elements causes ring artifacts in the reconstructed images. Threshold dispersion adversely affects spectral imaging by degrading energy resolution, which contributes to the blurring of the energy information. To improve the specificity of tissue characterization and material differentiation, an accurate selection of the energy range for measuring the difference in the attenuation of x-rays is

required. Appropriate threshold settings are important, specifically for K-edge imaging. Pulse pileup is always present in photon counting detector systems and is a function of the count rate and detector dead time. Pileup can also cause improper energy allocation; multiple events processed as one may have their energies summed, resulting in miss allocation [37, 53].

5.3.3 Spectral image contamination

Spectral image contamination occurs when information in the energy domain is distorted by errors in the spatial information. This includes effects such as charge steering in the detector, where the incident photon interaction is measured in a different position to the actual interaction position. Geometric misalignment may lead to spatial blurring in the reconstructed images giving rise to a "smearing" of energy information in adjacent voxels. Also, techniques applied in post-processing of images such as Gaussian blurring may distort the energy signal used to identify materials.

5.4 Preliminary methods of an image library

To develop a spectral image library several experiments were performed on MARS-10 that utilized a three-chip CZT-Medipix camera. A multi-contrast QA phantom was used that includes high-Z materials, lipid, and water. A protocol was created that includes tube voltage of 120kVp, tube current of 13μm, and exposure time of 300 ms and 1.96 mm aluminum filtration. Source to object distance (SOD), Object to detector distance (ODD) and the source to detector distance (SDD) was 223 mm, 45 mm and 268 mm, respectively. The energy thresholds were chosen to 19-30 keV, 30-45 keV, 45-75 keV and 75-118 keV with charge summing mode. Initially, a well-calibrated MARS scanner was used to scan a phantom (diameter of 33 mm) with different materials. Before studying the effects of geometrical parameters, a reference image was acquired with the well-calibrated MARS scanner (CTO=0 mm). The value of camera tangential offset (CTO) were chosen randomly to see the grade of edge blurring. Figure 5.1 represents the basic flowchart of image library. Figure 5.2 represent the image of the multi-contrast phantom and 3D images correspondingly. Figure 5.3 illustrates the reconstructed image of multi-contrast phantom at uncalibrated and calibrated scanner.

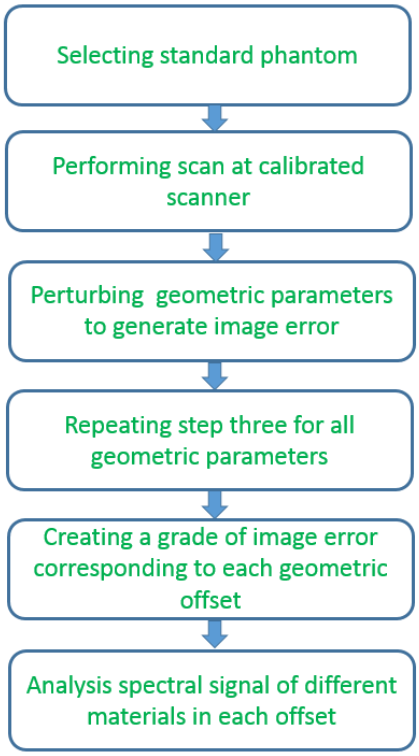

Figure 5.1 Basic flowchart for creating the image error.

(a) (b)

Figure 5.2 Multi-contrast QA calibration phantom (a) with vials filled with materials with different concentrations of lipid, water, 8 mg/ml and 2 mg/ml of gold, 8 mg/ml and 2 mg/ml of gadolinium, 18 mg/ml of iodine and 240 mg/ml of calcium.(d) representation of the 3D image of multi-contrast QA phantom.

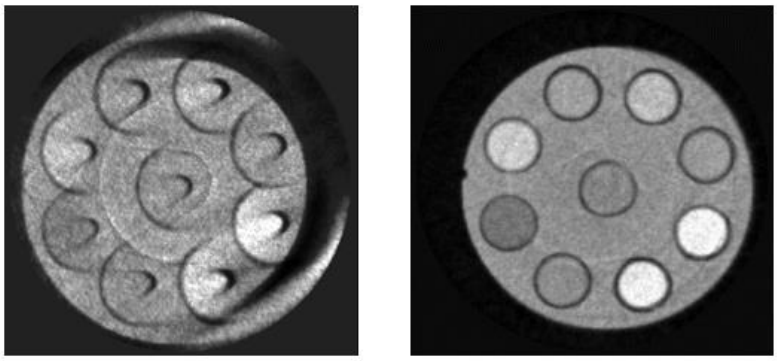

(a) (b)

Figure 5.3 (a) Edge blurring and shading due to a large tangential and axial offsets in MARS-CT on a reconstructed image obtained from a spectral phantom, and (b) clear reconstructed image after performing the geometrical calibration.

5.5 Results

In this study, the impact of the geometric parameter was investigated on the reconstructed image. Figure 5.4 shows the perturbation effect of geometric parameters in the spectral signal and higher value of geometric perturbation produces a less attenuated signal in each energy bin than the calibrated scanner (CTO=0 mm). To remove the density variation mass attenuation was calculated for each material that shown in Figure 5.5. The K-edge is not clear for all high-Z materials except iodine. It should be investigated whether there is any effect of the geometric perturbation on the K-edge properties. The linear attenuation value in Hounsfield (HU) of each material at different camera tangential offset is plotted in Figure 5.6.The value of (HU) decrease at higher energy range. The impact of geometric misalignment across the total number of voxel corresponding to (ROI) of each material is shown in Figure 5.7. Unstable attenuation response occurs in each voxel corresponding to ROI of each material at higher perturbation of geometric offset.

Figure 5.8 and Figure 5.9 shows the histogram of linear attenuation coefficients of different materials across the total number of voxels within an ROI on the calibrated and uncalibrated scanner. It can be expressed that histogram of linear attenuation of each material followed by symmetric distribution and tightly clustered about the mean whereas the histogram of linear attenuation of each material is widely dispersed and left skewed in case of an uncalibrated scanner. The histogram of relative linear attenuation of each material is plotted in Figure 5.10 and it follows the symmetric normal distribution and it is tightly clustered around the mean.

Figure 5.11 illustrate the impact of CTO on the reconstructed image of the multicontrast QA phantom and the resultant signal to noise ratio in each material correspondingly to each geometric perturbation. As it appears that increasing the value of geometric parameters decreasing the quality of the image. Edge blurring was appeared due to the impact of inaccurate camera tangential offset. Contrast to noise ratio (CNR) was also investigated for the normal and distorted image that were collected from calibrated and uncalibrated scanners. As seen in Figure 5.12, the CNR of each material is significantly higher in the normal image than the distorted image. Higher energy bin shows higher CNR except for Au:8 mg/ml.

Line profiles were measured to see the existence of edge blurring from the normal and distorted images. An oblique line was drawn across the central vial of the phantom. Figure 5.13 shows line profiles of normal and distorted images in different energy bins. The two sharp peaks represent the edge of the blurring and sharp edge is clear in each energy in case of the normal image. However, multiple peaks appear for the distorted image that indicates multiple blurring on the reconstructed image.

Subtracted and difference images were produced from the normal and distorted image. Figure 5.14 shows the line profile across the center vial for subtracted and difference images. This graph shows the difference between the normal and distorted image as well as the blurring around the central vial in the subtracted and difference image. The distorted image was differentiated from the normal image (calibrated image) to see the change between the normal and distorted image in the different slice at lower and higher energy in Figure 5.15 and Figure 5.16.

Figure 5.17 shows the axial anatomical reconstructed view of the normal image in different slices at different energy bins. All images are showing clear representation of each vial except third energy bins. Figure 5.18 shows the coronal view of the normal image of the multi-contrast QA phantom. Figure 5.19 shows the clear sagittal view of the reconstructed normal image of the QA phantom in the different slice at different energy bins.

Figure 5.20, Figure 5.21 and Figure 5.22 show the axial, coronal and saggital view of the distorted image in different slice at different energy bin to identify image blurring in different anatomical plan.

The impact of geometric misalignment on material decomposition (MD) was also investigated. The term material decomposition refers to the identification and classification of distinct materials within a volume that means it converts the spectral x-ray data into material based images. The concept that spatial distortions will lead to severe distortion in the material information is effectively demonstrated is in Figure 5.23, where the material information is shown to be almost completely obliterated due to the geometric error.

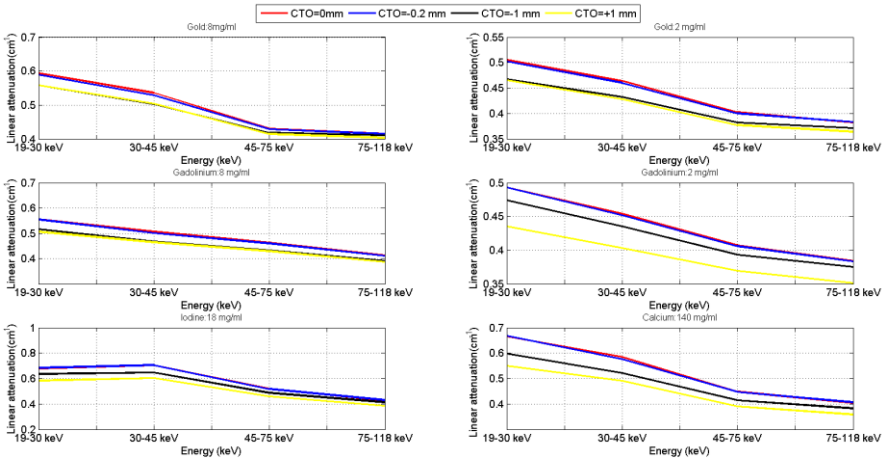

Figure 5.4 Linear attenuation of different materials at different CTOs.

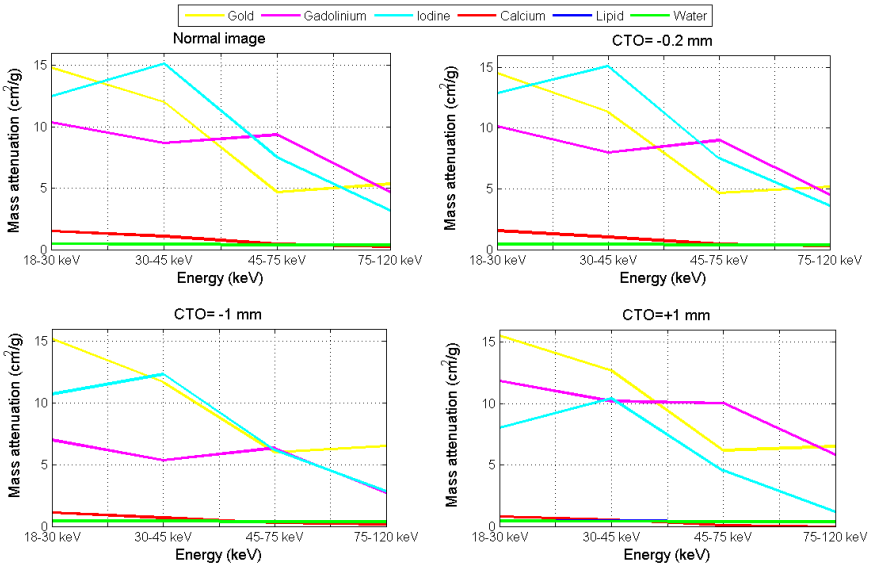

Figure 5.5 Mass attenuation profile of different materials at different energy bin under the perturbation of geometric offset.

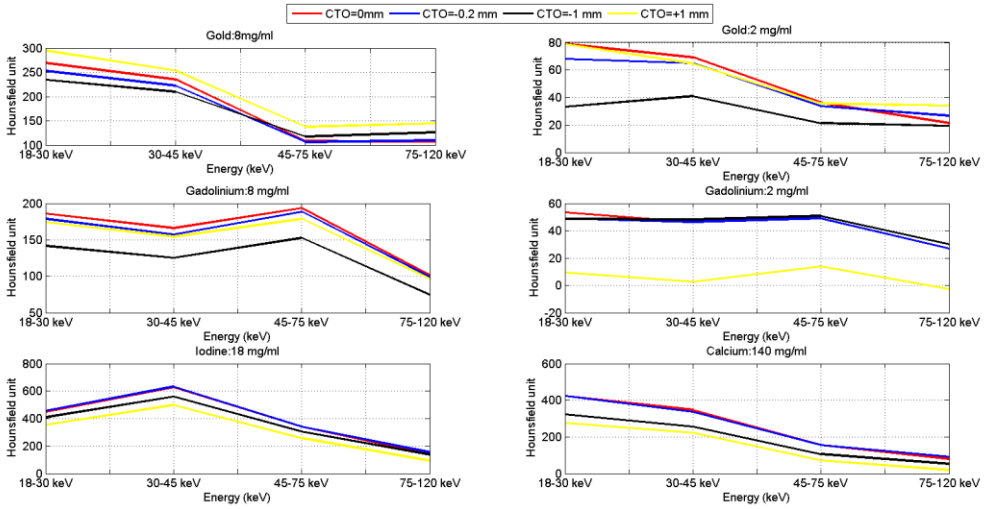

Figure 5.6 Attenuation profile of the different material in Hounsfield unit at the different value of geometric offset.

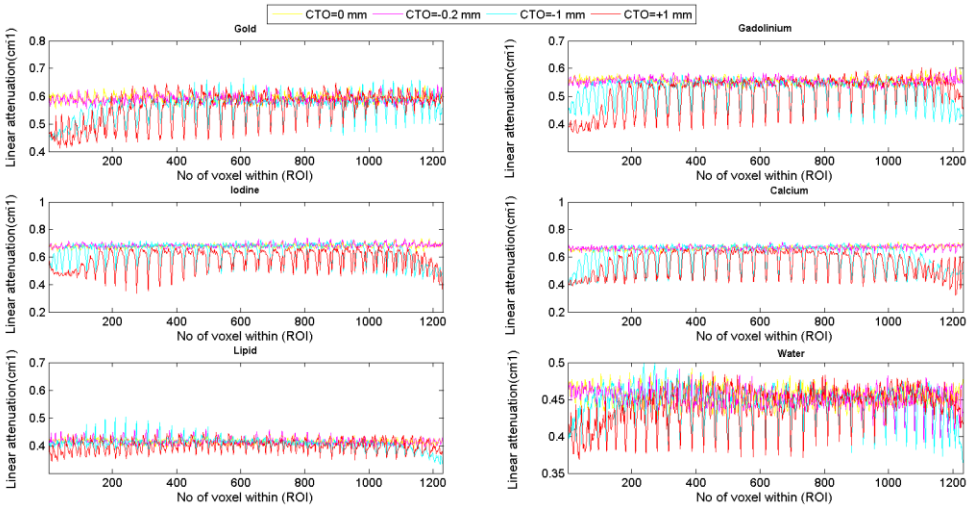

Figure 5.7 The response of linear attenuation of each material across the total number of voxel corresponding to (ROI) at the different value of geometric offset.

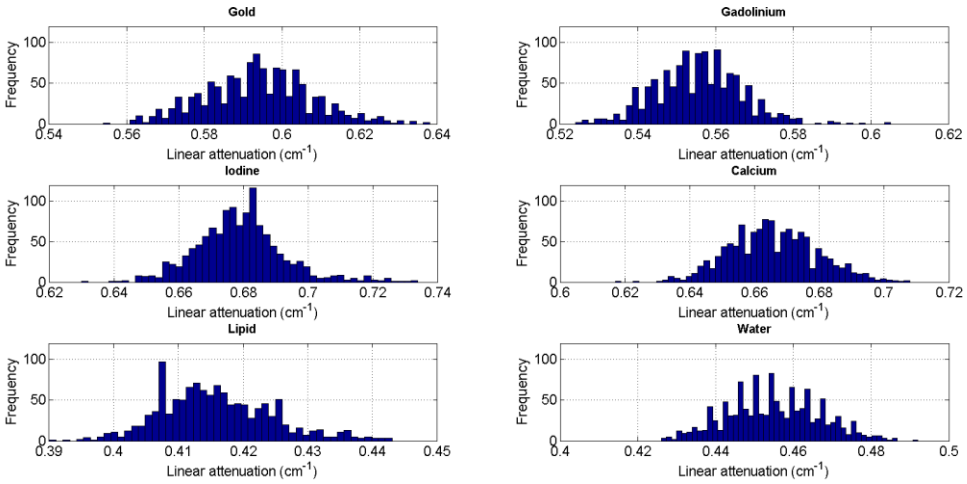

Figure 5.8 Histogram of linear attenuation of different materials across the total number of voxel within (ROI) at the calibrated scanner.

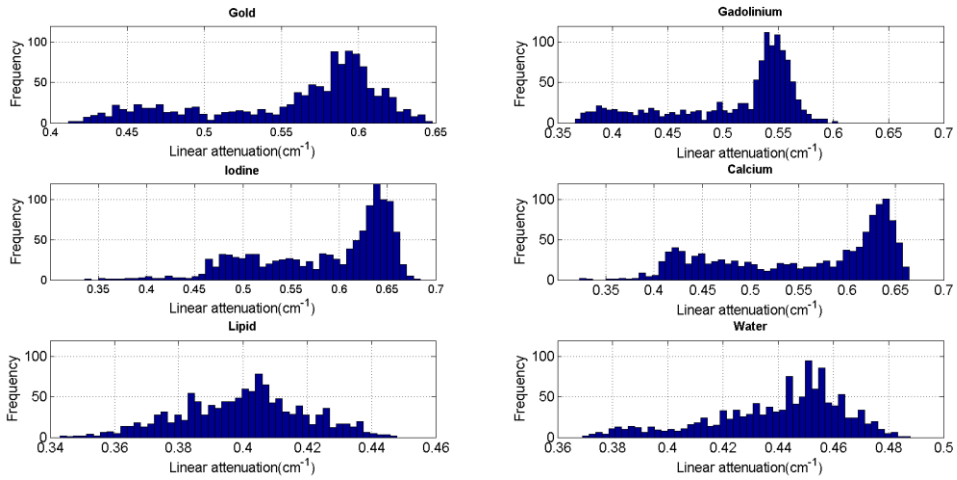

Figure 5.9 Histogram of linear attenuation of different materials across the total number of voxel within (ROI) at uncalibrated scanner

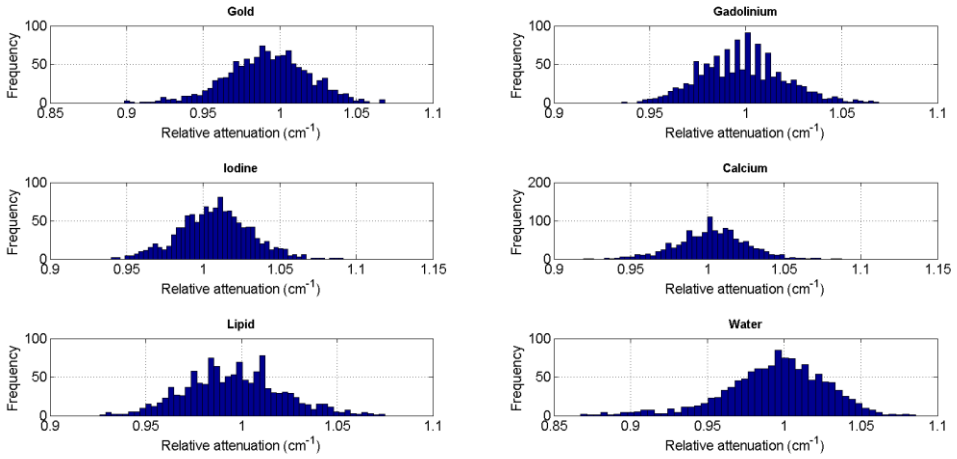

Figure 5.10 Histogram of relative attenuation of different materials across the total number of voxel within (ROI) at lower offset value.

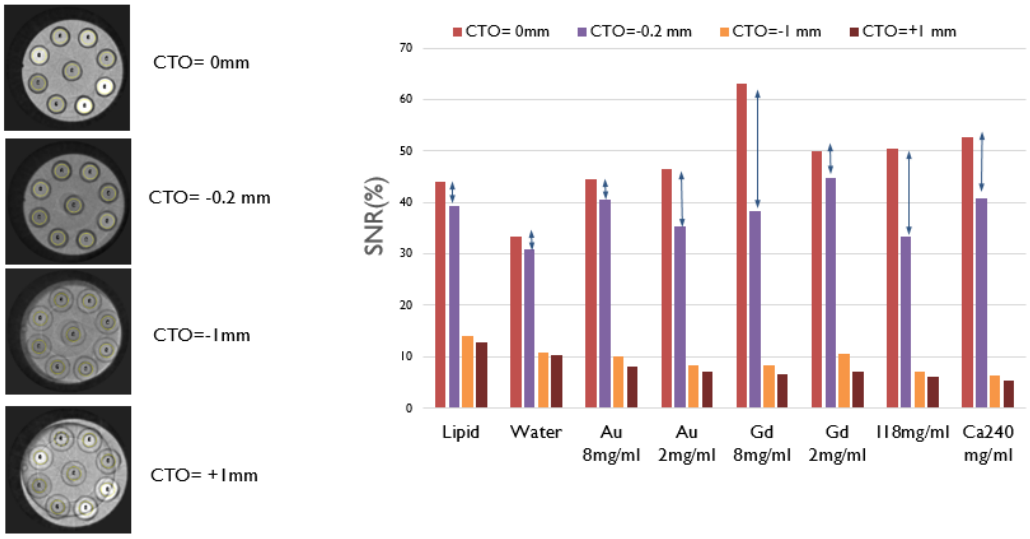

Figure 5.11 Impact of geometric misalignment in reconstructed images. Small geometric misalignment between camera and source can cause image distortion in the reconstructed images. The value of camera tangential offset were chosen randomly to see the level of spatial image error on the reconstructed image.

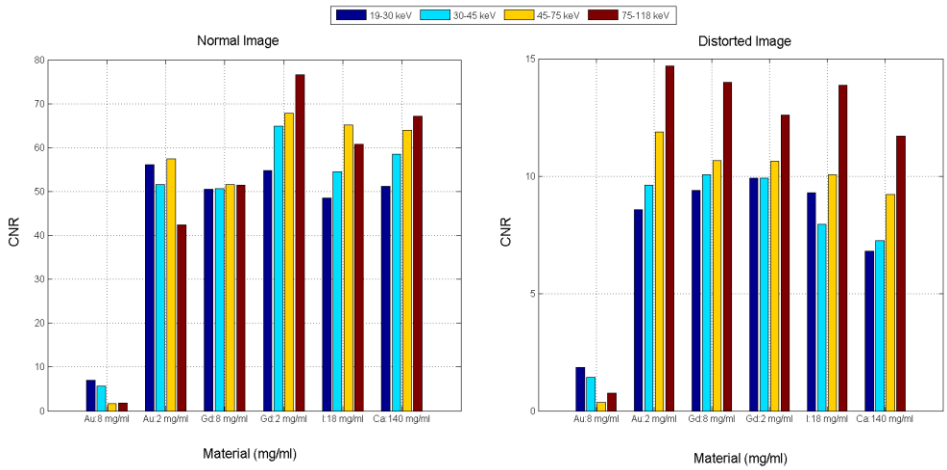

Figure 5.12 Contrast to noise ratio (CNR) of different material at different energy bin in the normal image and distorted image. CNR is significantly higher in the normal image than distorted image.

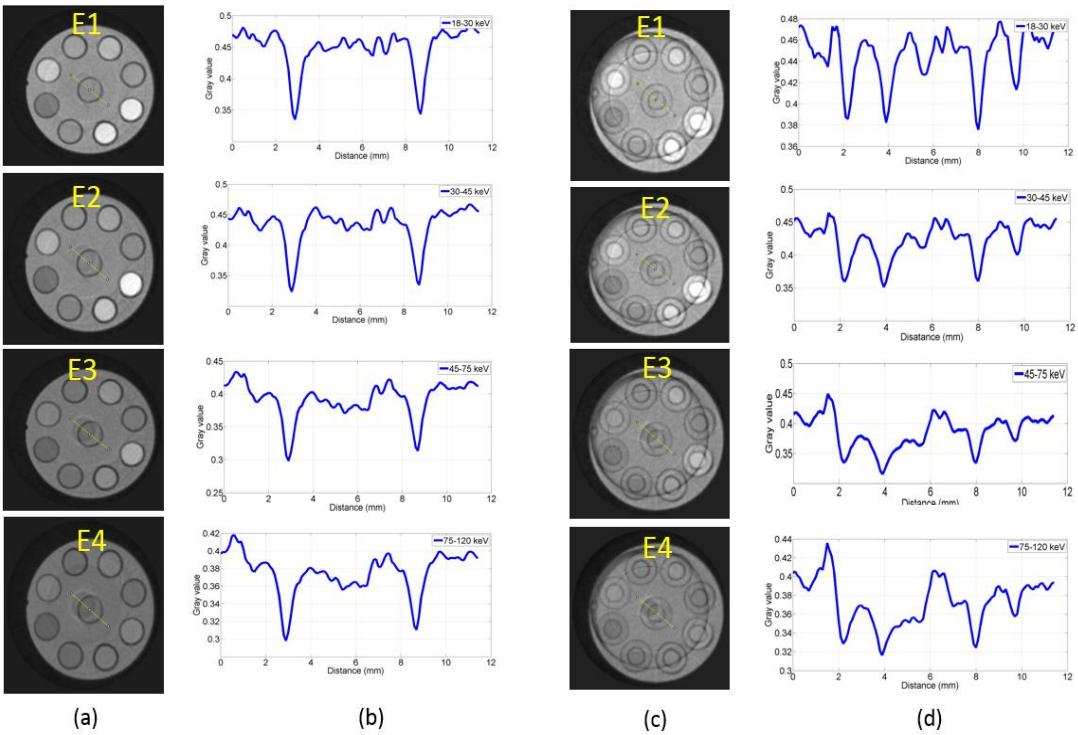

Figure 5.13 Line profile of gray value across the central vial of the normal image (a), the corresponding plot of the line profile (b) and distorted image(c) that shows multiple blurring and corresponding line profiles of the distorted image in (d) shows multiple peaks in their profile.

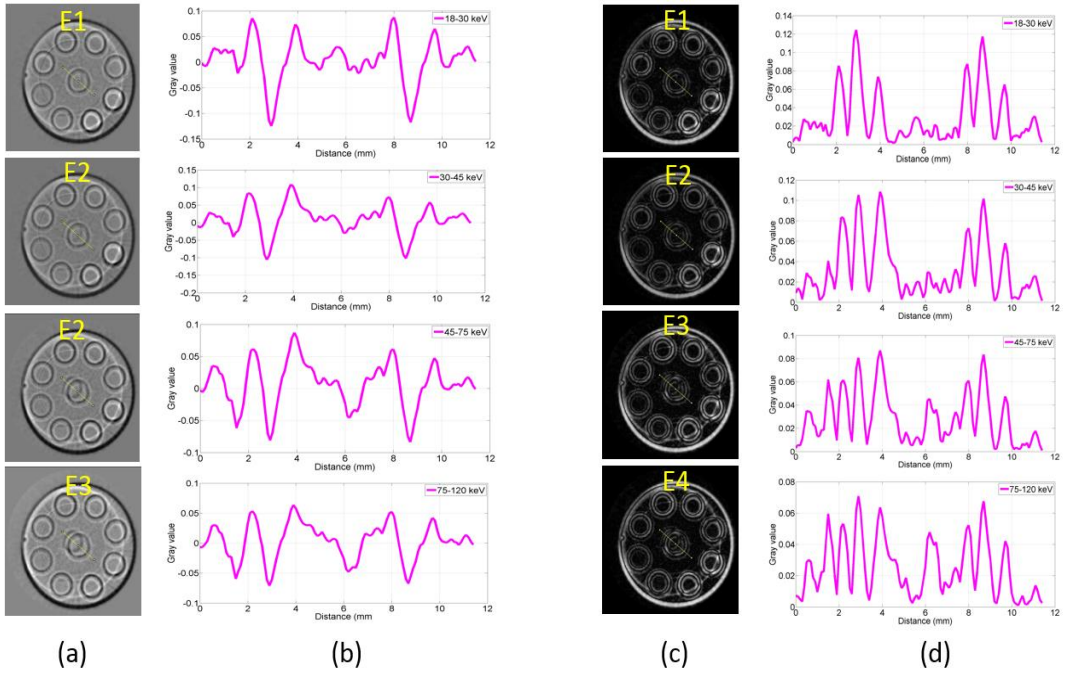

Figure 5.14 Line profile of gray value of subtracted and difference images at various energy bins.

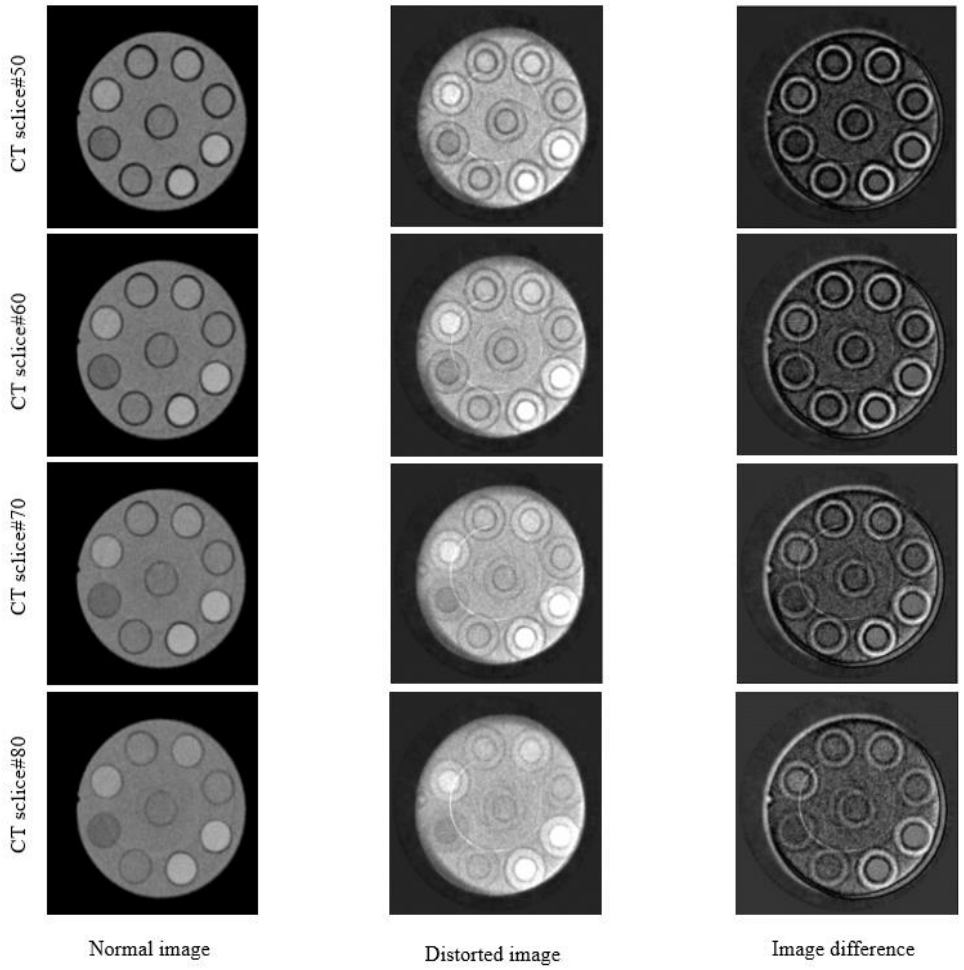

Figure 5.15 Image differencing from normal and distorted image at lower energy bin.

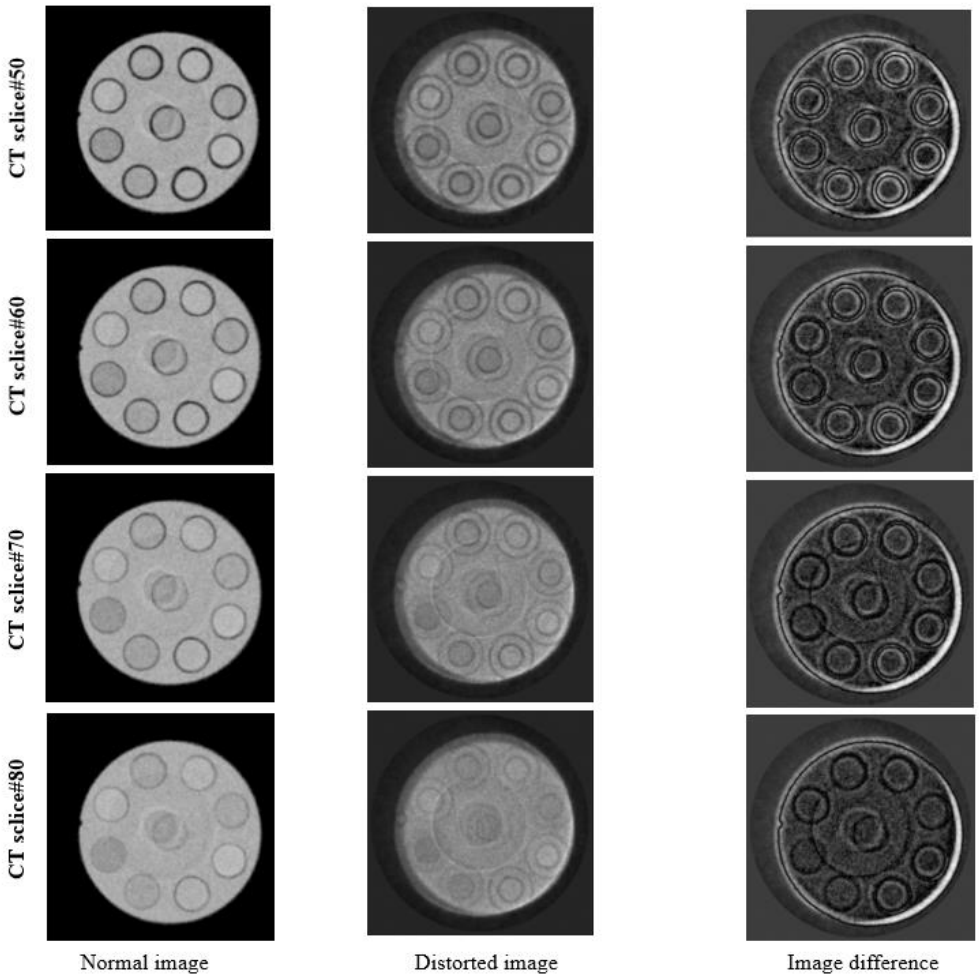

Figure 5.16 Image differencing from normal and distorted image at higher energy bin.

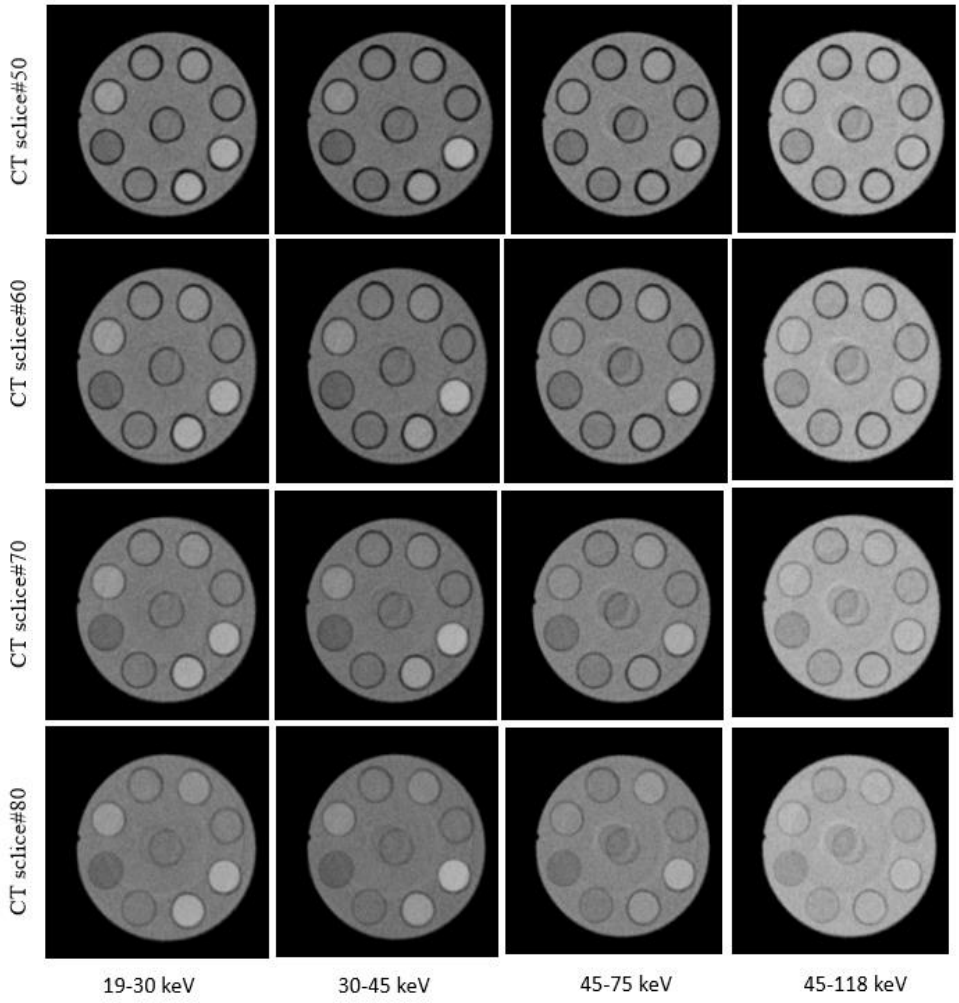

Figure 5.17 Axial reconstructed view of the normal image of multicontrast QA phantom in the different slice at different energy bins.

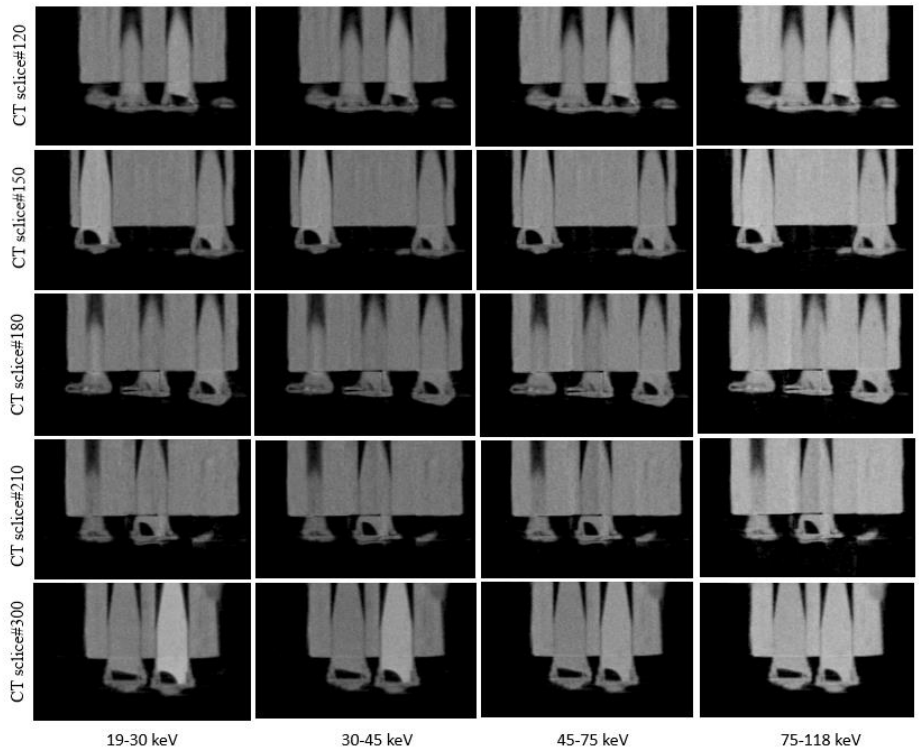

Figure 5.18 Coronal reconstructed the view of multicontrast QA phantom at in different slice at different energy bins.

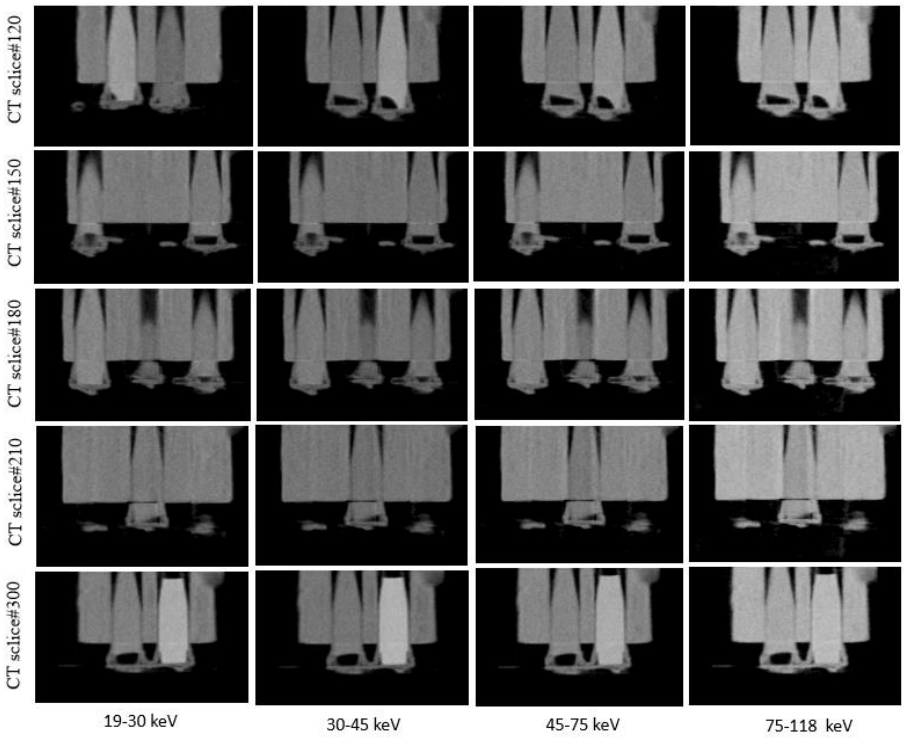

Figure 5.19 Saggital reconstructed a view of the normal image of multicontrast QA phantom in the different slice at different energy bins.

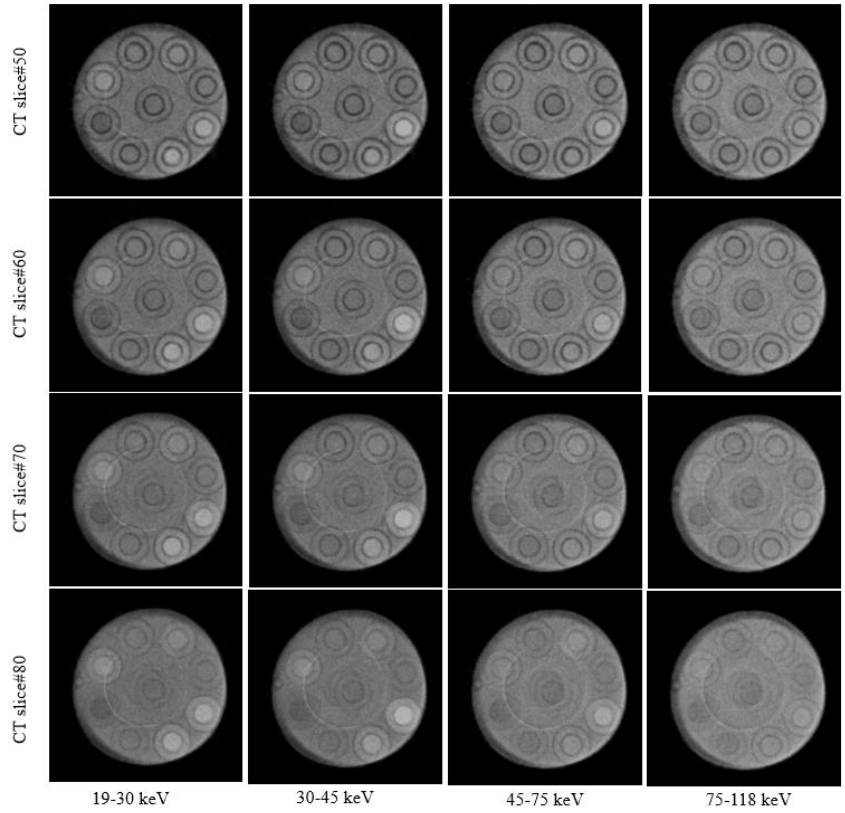

Figure 5.20 Axial reconstructed view of the distorted image in the different slice at different energy bins.

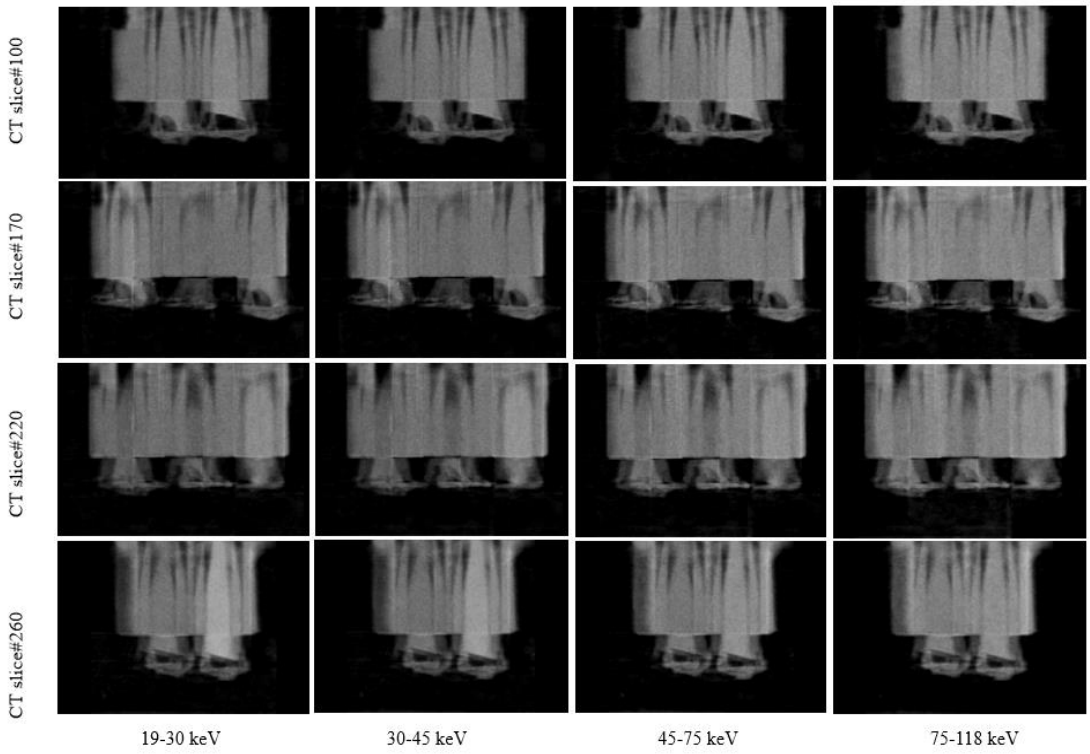

Figure 5.21 Coronal reconstructed view of multi-contrast QA phantom in the different slice at different energy bins.

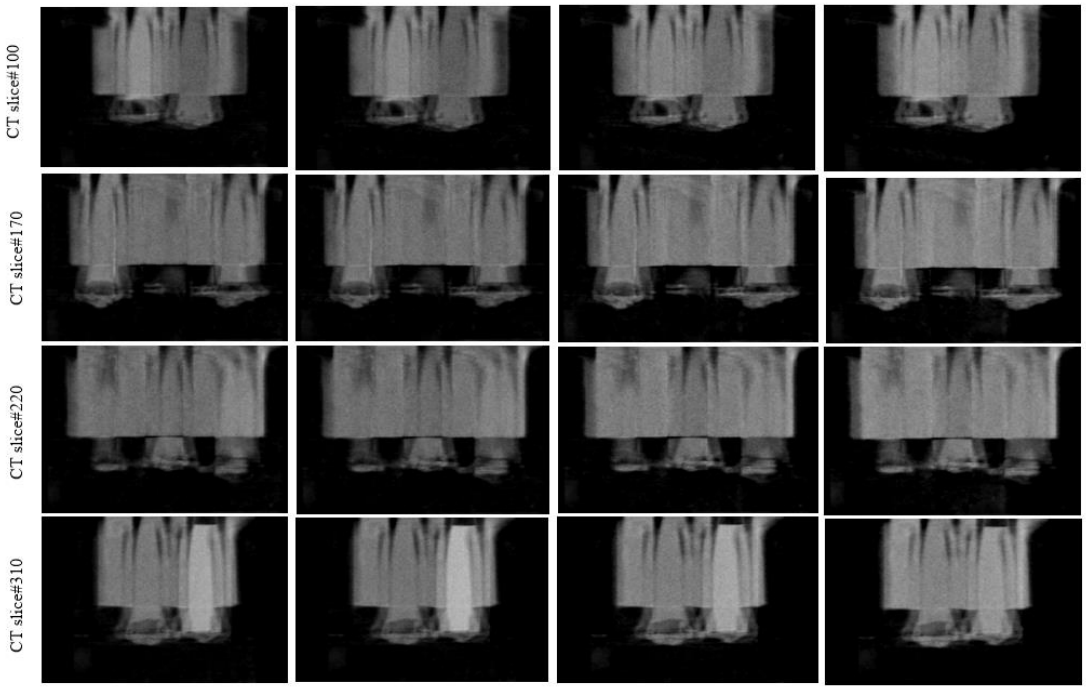

Figure 5.22 Saggital reconstructed view of multicontrast QA phantom in the different slice at different energy bins.

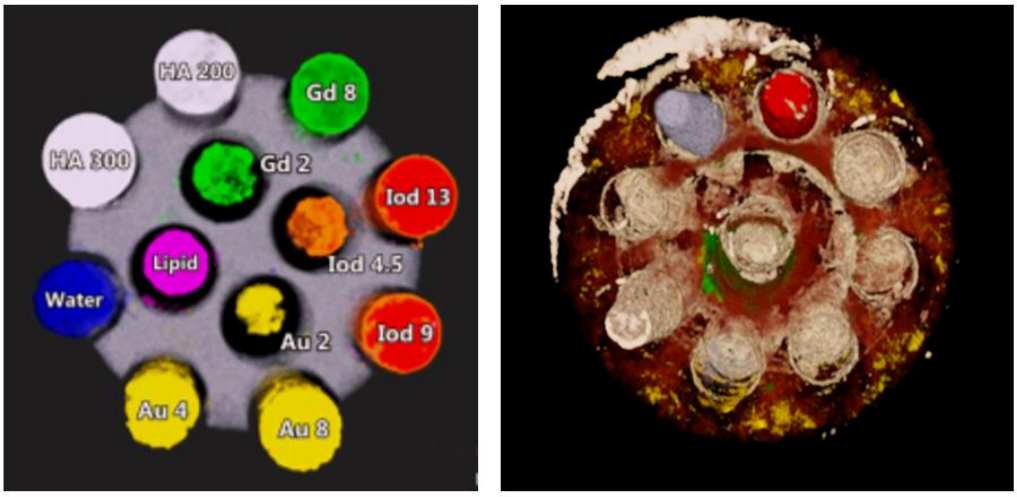

Figure 5.23 (a) Material image at calibrated scanner (Image courtesy: MARS Bioimaging) and (b) uncalibrated scanner that produce material misclasification.

5.6 Discussion

In this study, a preliminary method was developed for a spectral image library using the image of multi-contrast phantom. The impact of geometric misalignment on the reconstructed image was studied by perturbing different geometric offset parameters to investigate spatial image error.

Initially geometric parameters such as camera tangential offset were used to demonstrate the concept. To create the spectral image library a multi-contrast phantom was scanned in the calibrated and uncalibrated scanner to create the pair of normal and distorted images for each perturbation. Initially, camera axial and camera tangential offset were perturbed with different values. It was observed how the spectral signal from different materials is being degraded under the effect of the perturbation. The signal to noise ratio was degraded in an uncalibrated scanner compared to a calibrated scanner. Edge blurring appeared due to the

effect of inaccurate camera tangential offset. The blurring was measured by plotting the line profile across the central vial of the phantom. The contrast to noise ratio (CNR) in each material also degrades due to the spatial image error in case of the distorted image whereas the value of CNR is significantly higher in each material for the normal image. The image differencing technique was applied to evaluate the change between normal and distorted image. The image subtraction technique was used for evaluating the difference between normal reference images and those with the induced error. The linear attenuation response in each voxel corresponding to a region of interest (ROI) was observed. It is also found that the attenuation response is mostly skewed in the case of the distorted image, whereas the attenuation response is symmetric in case of a normal image. It was also found that how much spatial error degrade the energy information by spreading the energy information of one voxel into neighboring voxels.

The novel feature of this investigation is to find out the relationship between geometric information and the energy information and implication for material reconstruction. An important concept investigated is that the information in the energy domain of spectral CT images is linked to the spatial domain. Consequently, if there are spatial artifacts in the reconstructed images, there will be a corresponding distortion in the energy information. The spatial information can be considered to be the total linear attenuation in a given voxel, which is the information provided by conventional CT scanner. The energy information is the linear attenuation for each of the available energy channels in each voxel. It was observed that how spatial distortions create severe distortion in the material information due to the effect of camera tangential offset.

Circular ring artifact produces due to the gap between the chips, faulty chip or faulty pixels or miscalibration of the detector elements. Edge blurring was reduced by correcting camera tangential offset. Ring artifact was also reduced by changing the arbitration counter above the noise floor, proper pixel masking and performing energy calibration. The method of estimating different geometric offset of MARS scanner is discussed in chapter 6.

5.7 Summary

- A spectral image library was created to see the impact of spatial image error in the reconstructed image of the multi-contrast phantom that incorporates different high-Z materials.

- The main source of image error for MARS scanner is are spatial image and spectral image error. The spatial and spectral image error produce from geometric misalignment and poor energy calibration of the detector elements respectively. In

this study, spatial image error was investigated by perturbing the inaccurate value of the geometric parameters.

- The effect of inaccurate camera tangential offset occurs edge blurring in each vial of the reconstructed image.

- Small geometric misalignment between the camera and source cause image distortion in the reconstructed image. The small value of tangential offset can degrade the SNR value.

- The contrast to noise ratio of each material is decreased in each energy bin in case of the distorted image.

6 Geometric calibration for MARS scanner

6.1 Introduction

This chapter demonstrates a method to estimate the geometric parameters of the MARS scanner. In this study, a geometric calibration method was developed that allows measuring the offset of different geometrical parameters which can then be corrected during image reconstruction. Accurate geometric calibration through a systematic approach is necessary to minimize the image artifacts, and as a consequence enhances the capability of the MARS scanner in material identification and quantification. Geometric calibration is also important in order to minimize image error as well as achieve good image quality. The reason for doing this work was to develop a robust geometric calibration method that could be used to measure the alignment error and allow for their correction during image reconstruction.

Computed tomography has been a revolutionary contribution to medical imaging and also has been successfully used in industrial non-destructive testing. The image quality and spatial resolution of the CT scanner is affected by image blurring, ring artifacts, and beam hardening. Image artifacts are is produced due to geometric misalignment of the x-ray source, object, and detector. In an ideal cone-beam CT, the x-ray focal spot, the center of rotation of the system and the center of the detector are in a straight line. However, in practice, it is nearly impossible to avoid any misalignment in the CT system. Even a small error in the estimation of any parameter causes visibly detrimental effects on the reconstructed image, which was shown in chapter 5.

Many methods have been proposed for geometric calibration of CT scanners. Geometric calibration methods can be classified into two categories: one phantom-based offline method and another is phantom-less online method [54, 55, 56, 57] Lorenz von Smekal et al. [58] presented a high-precision method to determine the complete misalignment parameters based on Fourier analysis through multiple projection images. Yi Sun et al. [59] proposed a method to calculate geometric parameters using a ball bearing phantom.

A geometric calibration method was developed for MARS scanner that was used a line phantom to measure the magnification, chip gap, camera offset (axial and tangential) and chip orientation. While the aim was to measure all geometrical parameters as accurately as

possible, a measurement accuracy of ± 10 μm for most of the parameters was targeted. A key feature of this method is to measure the geometrical parameters from the projection images so that they are unlikely to be biased by possible errors in the reconstruction methods.

6.2 Phantom design

In this study, a line phantom that was designed and developed by MARS bioimaging that was used to perform the geometrical calibration in different MARS scanners. The line phantom incorporates fiberglass with thin copper tracks coated with a few microns of gold. This phantom consists of different diameters of copper tracks which follow a special pattern that allows measurement of the geometrical offset with the accuracy of a few microns. As shown in Figure 6.1, the plastic circuit board (PCB) is $1.5 \times 89.8 \times 120$ mm^3 with the vertical, horizontal, and diagonal patterns; and track centers are 500 μm apart. A series of projection images acquired from the line phantom is used to measure the geometric offset parameters.

Figure 6.1 PCB line phantom used for geometrical calibration of the MARS spectral scanner.

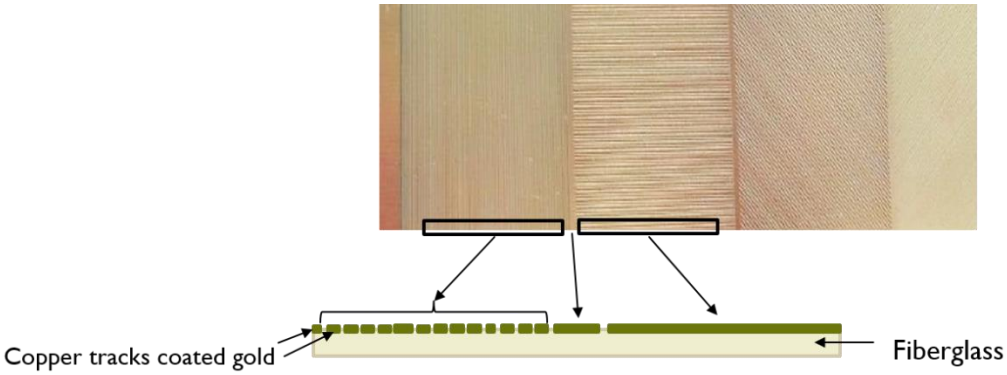

Figure 6.2 Side-view of the PCB line phantom.

6.3 Materials and method

To measure the geometrical parameters using the line phantom, the following steps are are performed: (1) measurement of the angular offset between gantry and line phantom; (2) measurement of sample x offset; (3) measurement of radial offset of the x-ray tube and detector; (4) measurement of camera x-ray tube axial and tangential offsets, chip X and chip Y, and chip rotation.

6.3.1 Measurement of angular offset between gantry and line phantom

The phantom surface was aligned parallel to the detector so that it is aligned perpendicular to the x-ray. For this purpose, the line phantom is mounted on the sample holder and then the gantry is rotated as follows:

Rotate the gantry $90^{\circ}$and cotinue changing the gantry angle by a few degrees while tracing the shadow of the edge of the line phantom on the image. In a single gantry angle, the shadow of the line phantom has minimum thickness where the gantry is perpendicular to the phantom (Figure 6.3). This angle is the relative offset between the current sample and gantry which is called θ_p.

Figure 6.3 A projection image collected in 90°shows the top view of the line phantom.

6.3.2 Measurement of sample-x offset

The sample-x in the MARS GUI needs to be adjusted to ensure that the sample (line phantom) is located at the center of the rotational axis (Figure 6.13). To do this, the gantry was rotated by $\theta_p + 90 - 90^{\circ}$ and once $\theta_p + 90 - 90^{\circ}$. It is expected that the image of the copper edge (Figure 6.2) in 90°gantry rotation, is overlapped by the shadow of the same coper edge in -90°gantry rotation as shown in the right image of (Figure 6.4). However, the image of the copper edge (copper teeth) at 90° may be displaced from the -90° due to unadjusted sample x which is shown in the left image of (Figure 6.4). The distance between these two edges in the projection images needs to be measured and corrected in the sample x offset. The corrected image is shown in (Figure 6.5).

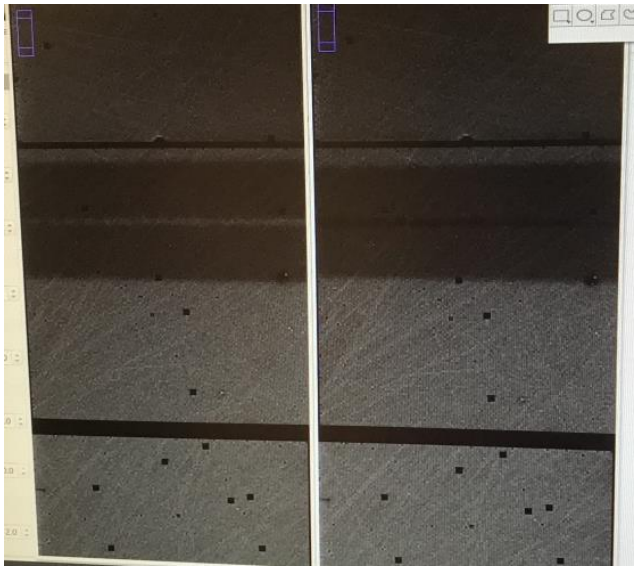

Figure 6.4Two fused projection images collected in $90^{\circ}$and -90° showing the top view of the line phantom. The gap between the two copper teeth shown in the left side image indicates the presence of a sample-x offset (-0.6 mm) which was then applied and the right side image obtained.

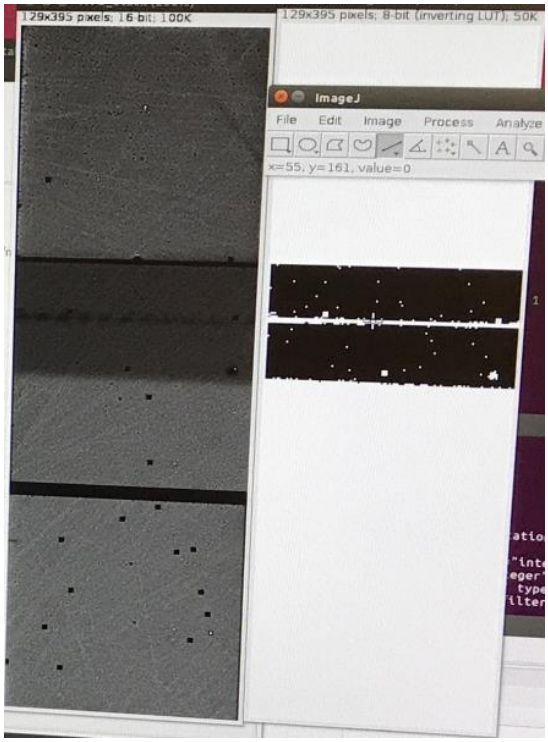

Figure 6.5 Two fused projection images collected in 90° and -90° showing the top view of the line phantom with the corrected sample-x offset.

6.3.3 Measurement of radial offset of the x-ray tube and detector

The radial offset is either in the source to object distance (SOD) or in the object to detector distance (ODD) which can be measured by varying these variables and measuring the actual magnification. Every two sets of magnification measurements are used to solve the simultaneous equations and find the radial offset with respect to the values set into the MARS UI as presented by equation (6.1).

$$M = \frac{I'}{I} = \frac{SAD + ODD}{SAD} \tag{6.1}$$

where, M is magnification. I and Í are the object size and image size, respectively.

To make each set of equation, the measured magnification (Meas. M) is used as a known item which is calculated from equation (6.2).

$$M = \frac{\text{Number of copper tracks on the image} \times 110\mu m}{\text{Number of copper track on the phantom} \times 500\mu m} \quad (6.2)$$

6.3.4 X-ray tube magnification

It is possible to change the x-ray tube magnification by setting different SODs on the MARS GUI. To obtain the highest contrast between the copper tracks and fiberglass, low tube voltages needs to be used. The exposure time and tube current need to be set to ensure that the detector is operating in the linear range as well as acquiring significant counts. To reduce the uncertainty the counts, acquiring at least 1000 frames is recommend. Four to six steps are also recommended from the minimum SOD to the maximum SOD. The gantry offset and sample-x that were calculated from the previous steps are also set into the MARS UI. A mid-range of the ODD is recommended such as 70 mm. The energy threshold of 15 keV for the first is sufficient to collect enough counts. However, the measurement of other counters in this threshold can be set later to reduce the uncertainty over the geometrical offset measurements. A series of projection images are required as listed below:

1. Projection images from the line phantom at 4 to 6 steps at 0°.
2. A series of open beam images with the same setting mentioned above for 0°.
3. Projection images from the line phantom at 4 to 6 steps at 180°.
4. A series of open beam images with the same setting mentioned above for 180°.

The x-ray tube magnification is only changed in step 4, while the detector magnification may need to be set for specifically measuring the offset parameters for each x-ray source and detector.

6.3.5 Data pre-processing

To analyze the data and measure the geometrical parameters, the projection images obtained from the line phantom are summed across all frames at each SOD and divided by the corresponding summed open beam images.

6.3.6 Magnification measurement in MARS-16

Magnification can be measured from each row of projection images obtained from the line phantom. It is expected that the measured magnification across all rows of the projection image are the same with low standard deviation. However, the magnification measured from some rows deviated greatly from the mean magnification due to the presence of unstable pixels.

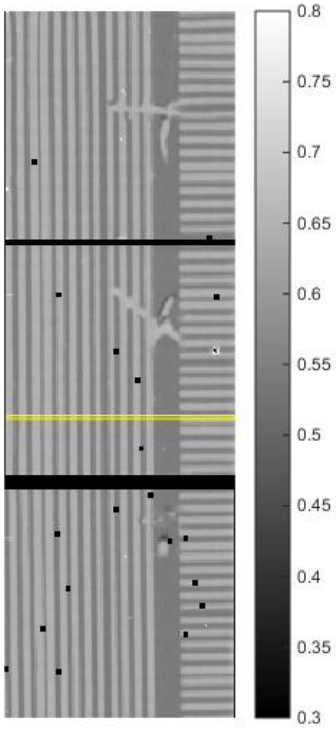

Figure 6.6 A normalized image from the line phantom acquired from MARS-16. The highlighted row is demonstrated in (Figure 6.7) to explain the magnification measurement.

A series of projection images were acquired from a line phantom using MARS-16 and normalized by corresponding open beam images. Figure 6.6 shows a normalized projection image for SOD=155 mm and ODD=70 mm. Figure 6.7 shows the response of the pixels across a single row (#228) of the image shown in Figure 6.6. The troughs show the x-rays absorbed by the copper tracks coated by gold on the fiberglass, whereas the peaks show the number of the x-rays absorbed by the fiberglass only. Magnification is calculated by the following formula:

$$\text{Magnification} = \frac{\text{Image size}}{\text{Object size}} = \frac{\text{Distance between two given copper lines}}{\text{Distance between two detected lines on the phantom}} \quad (6.3)$$

The distance from the half of a trough on the left side of the image to another trough to the right side of the image is calculated. These two troughs are marked on Figure 6.7 by two vertical dash lines which are spaced 6168 μm from each other.The pattern between two troughs is also traceable on the line phantom which indicates the distance of 4000 μm (8 × 500 μm) between them on the phantom. Using the SOD and ODD set to the MARS GUI, the expected magnification is 1.45 which is 6% less than the measured value. This discrepancy can be reduced to 0.06% if each of x-ray tube and camera radial offset is corrected by -4 mm and 12 mm, respectively.

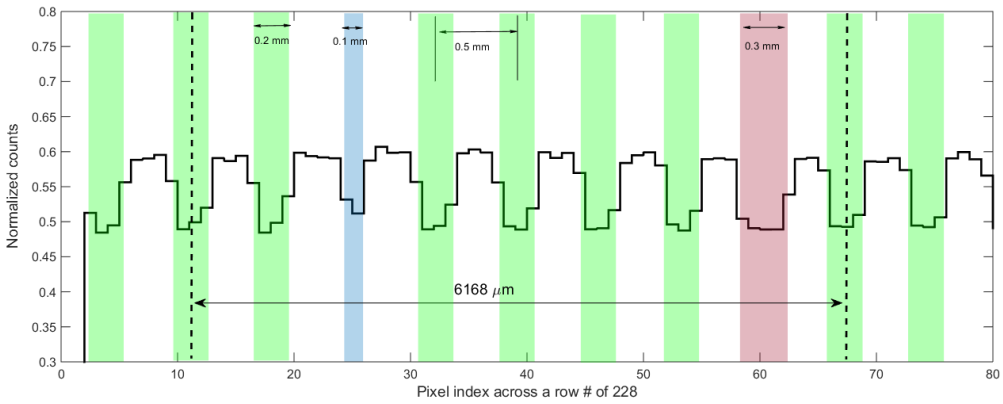

Figure 6.7 Recorded counts in one row of the normalized image (Figure 6.7). The color columns show the pattern of the copper lines.

6.3.7 Chip Y

Chip Y represents the y-axis of each chip where the origin of coordinates of the mounting plate is considered to be is at the top left corner of the first chip (Figure 6.8). The first step is to measure the gap between the top and middle chips and the middle and bottom chips by tracing the pattern of the copper tracks on the projection image and comparing with the actual pattern. Figure 6.8 demonstrates the position of the chip gap and the region of the grid image that is considered in this particular example shown in (Figure 6.9). Two parts of $a\acute{a}$ and $b\acute{b}$ are involved to calculate the gap between chip A and chip B, and two parts of $c\acute{c}$ and $d\acute{d}$ are involved to calculate the gap between B and chip C. A single column of this grid image is demonstrated in Figure 6.9 alongside the measured value for each part. The gaps between chip A and B is calculated from the following formulas.

$$\text{Gap AB} = \text{ab}' \text{ on the phantom} - \left(\frac{\text{aa}' \text{ on image}}{\text{magnification of chip A}} + \frac{\text{bb}' \text{ on image}}{\text{magnification of chip B}}\right) \quad (6.4)$$
$$= (20 \times 500) - (5162 + 4612) = 226\mu\text{m}$$

$$\text{Gap BC} = \text{cd}' \text{ on the phantom} - \left(\frac{\text{cc}' \text{ on image}}{\text{magnification of chip B}} + \frac{\text{dd}' \text{ on image}}{\text{magnification of chip C}}\right) \quad (6.5)$$
$$= (16 \times 500) - (4456 + 3040) = 504\mu\text{m}$$

Y_A (for the top chip) is zero with respect to the origin of the coordinates mentioned above. Y_B and Y_C are also calculated from the following equations:

$$Y_B = \text{chip size} + \text{gap between chip A and chip B} \quad (6.6)$$
$$= 14.08 + 0.227 = 14.307\text{mm}$$

$$Y_C = Y_B + \text{chip size} + \text{gap between chip B and chip C} \quad (6.7)$$
$$= 14.07 + 14.08 + 0.504 = 14.307\text{mm}$$

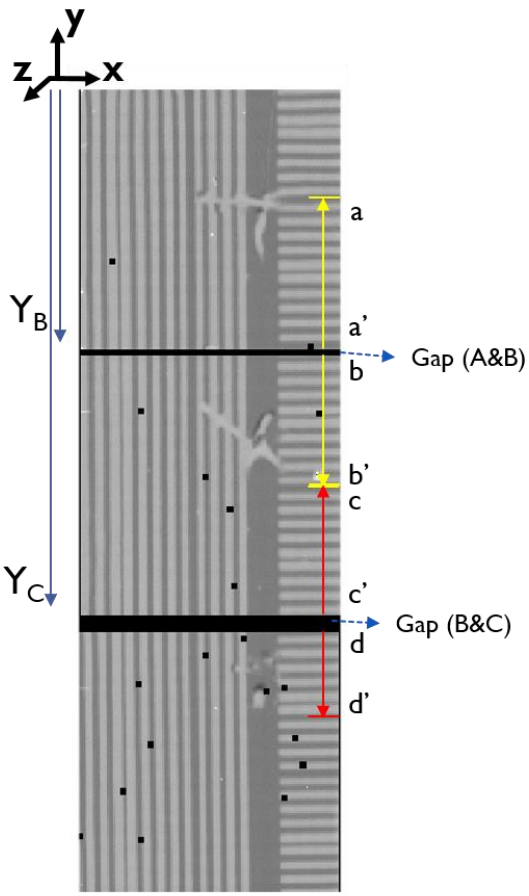

Figure 6.8 A normalized image from the line phantom with the indication of aa', bb', cc', and dd' that are used to calculate the gap between chip A and B and chip B and C, respectively.

6.3.8 Chip X

The horizontal positions of chip A and chip C are calculated with respect to the middle chip. Two approaches can be considered to calculate the chip. A single row near to the edge of each chip is selected and compared to a single row of the adjacent chip as shown in Figure 6.10. The first pair of rows from chip A and chip B are plotted in (Figure 6.11). This shows that the top chip needs to be shifted by half a pixel (55 um) towards the left. The second pair of rows from chip B and chip C are plotted in Figure 6.12 which indicates a displacement of a half pixel for the bottom chip towards the right.

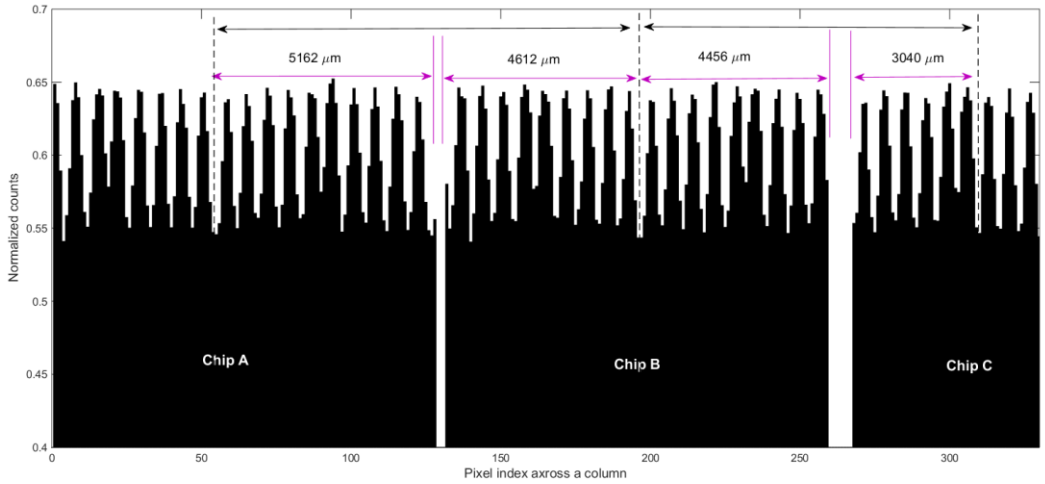

Figure 6.9 Normalized count vs. pixel index across a column between passing through the horizontal copper lines.

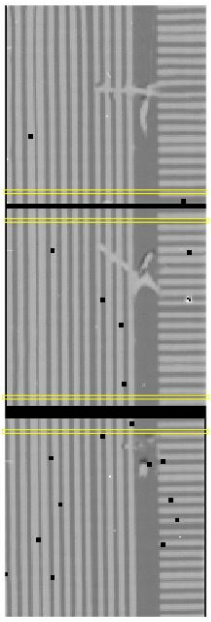

Figure 6.10 Normalized projection used to calculate the horizontal position of chip A and chip C with respect to the middle chip.

6.3.9 Tangential offset

The x-ray source and the camera may not be aligned. Performing step 3 of the measurement procedure will indicate if the center of the ray passes through the center of the camera or not. The central ray can be off tangentially or axially in a cylindrical coordinate explained in the previous chapter

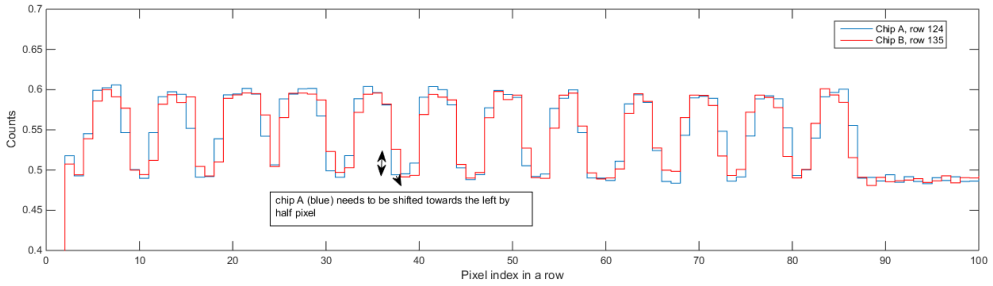

Figure 6.11 The normalized count at pixel index across the adjacent row of chip A and chip B; showing that top chip needs to be shifted by half a pixel towards the left.

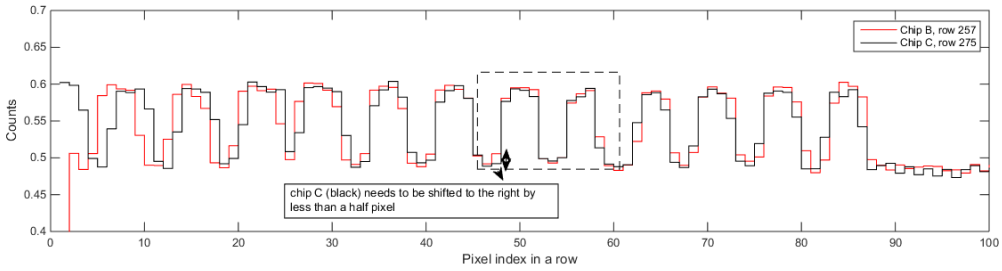

Figure 6.12 The normalized count at pixel index across the adjacent row of chip B and chip C; showing that bottom chip needs to be shifted by half a pixel towards the right.

It is worth noting that these offsets can be either from the camera or x-ray source. Currently, such relative misalignment is corrected on the camera side only. However, further measurement is required to identify the geometric offset of x-ray tube and detector. Camera tangential offset (CTO) is measured from the comparison between the projection images of the line phantom obtained at 0° and 180° as shown in Figure 6.14. Furthermore, the projection data acquired by changing the x-ray tube radial distance (SOD) can also be used for tangential offset which will be explained later. Both methods of CTO measurements are explained as follows:

- **CTO calculation using projection images of $0^{\circ}$and 180°.**

In the first method of CTO calculation, the projection image obtained from 180° is flipped up to down in order to be matched with the real camera position as demonstrated in Figure 6.13.Then, the flipped projection image shown in Figure 6.14 is compared with the projection image at 0°. There are several identification marks on the line phantom which enables the user to trace the camera displacement (D) at 180° as compared to 0. The camera tangential offset can be then obtained from the measured D using the following formula:

$$\text{CTO} = \frac{\left(\text{D} - (\text{actual image origin} - \text{image origin set to the config. file})\right)}{2} \quad (6.8)$$

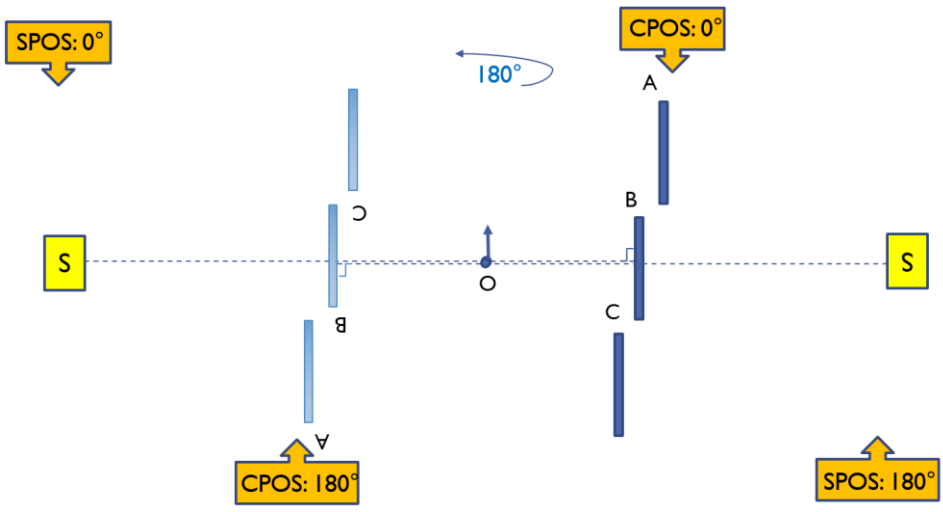

Figure 6.13 The source position (SPOS) and camera position (CPOS) at 0° and180°. In MARS scanner, the object is fixed at the rotational axis (O), while rotating the source and the detector by 180°around the object resulted in reversing up-down position of the camera.

- **Second method of CTO calculation**

The projection images obtained from different x-ray tube magnification can be used to measure the tangential offset. The idea behind this calculation is to trace the position of the straight line to the camera. By changing the magnification, sizes of the copper tracks on the image are changed except that the image of those copper tracks being formed by the perpendicular rays (or nearly perpendicular) to the phantom plane and detector.

Figure 6.15 is obtained by summing of all projection images across different x-ray source radial distances/SODs. In this figure, the horizontal lines look sharp only around a region in the right side of the central chip. To accurately calculate the tangential offset, the same column of the projection image at each SOD is selected and compared with each other. As shown in Figure 6.16, the minimum variation can be observed at pixel 176 which indicates the main horizontal perpendicular line passes through row 176. Identification of the position of this perpendicular row allows us to measure the camera tangential offset. This offset can be measured from two different reference points; either with respect to the center of the image or Identification of the position of this perpendicular row.

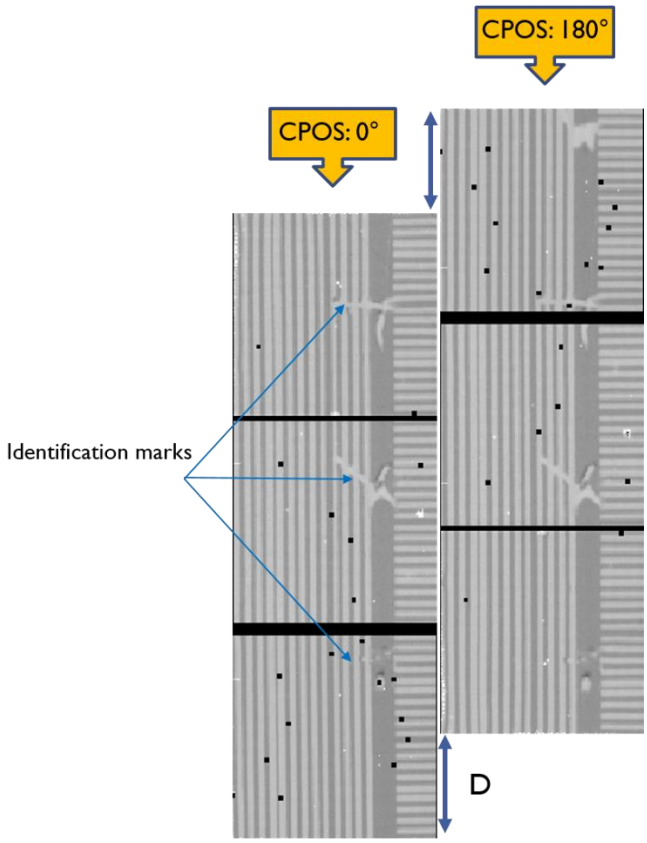

Figure 6.14 Projection images of a line phantom at 0˚and 180˚showing the displacement of the camera across the 180˚rotation (D).

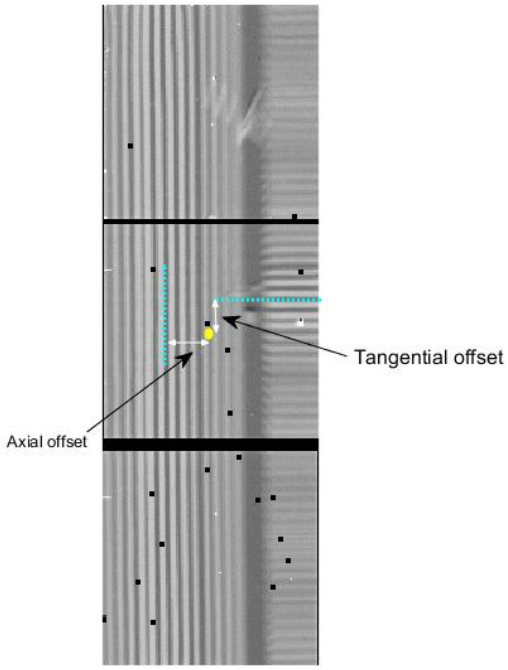

Figure 6.15 Summation of all projection images across different x-ray source radial distances.

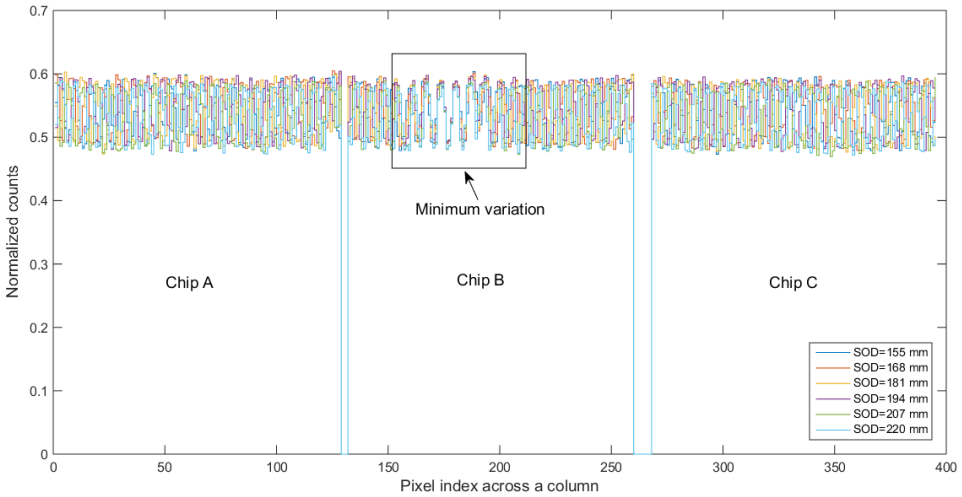

Figure 6.16 Superimposition of the normalized counts of a single pixel column across all projection images obtained in different x-ray tube magnifications.

6.3.10 Axial offset

Horizontal differences between the position of the perpendicular ray to the center of the camera (central chip) is known as the axial offset in cylindrical coordinates (Figure 6.15). As mentioned before, this offset can be due to misalignment of either x-ray tube or detector. However, this relative misalignment is currently corrected on the camera side.

To measure the camera axial offset (CAO), the row that was already labeled with minimum variation in tangential offset measurement (176 in the above example) is assessed across datasets with different x-ray tube magnifications. Figure 6.17 shows how the image of the copper tracks converged around pixel No. 38 and then diverged gradually as a result of magnification. Therefore, the most perpendicular ray pixel was detected by No. 37 so that 37 could be a good approximation for the position of the perpendicular ray. The axial offset is then calculated by the following formula:

$$\begin{aligned} \mathrm{CAO} = (&\text{Center of the width of projection image} \\ &- \text{position of perpendiculer ray}) \times \text{detector pixel size} \end{aligned} \tag{6.9}$$

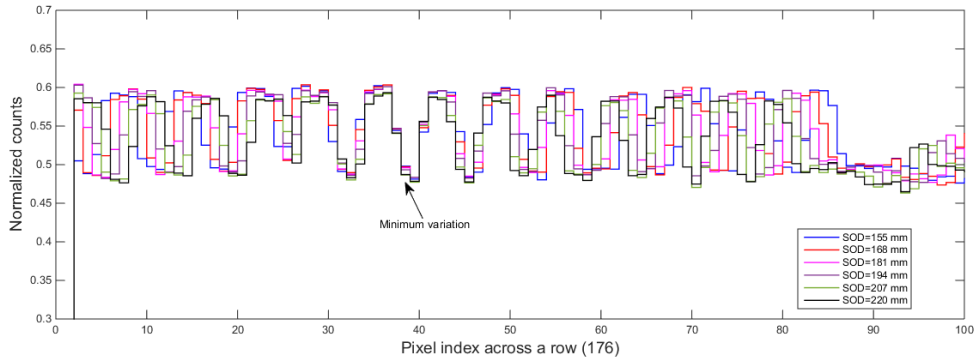

Figure 6.17 Superimposition of the normalized counts of a single pixel row across all source magnifications. The arrow pointed where the superimposed signal have less variation.

6.3.11 Chip rotation

It is likely that the chip is mounted with a slight tilt on the mounting plate. The amount of the tilt needs to be measured in the x-y plane and corrected in the mechanical configuration file of the camera.

To measure the rotation of each chip, a column of the projection image is assessed that passes through the edge of a copper line located near to the vertical stationary ray (i.e. the vertical stationary ray was identified to be matched with column 37 in the previous example). As shown in Figure 6.18, tracing the fitted line to this column at each chip enables us to identify if there is any rotational angle difference between three chips. Figure 6.18 show how the fitted lines across all three chips have less than 0.05° angle difference.

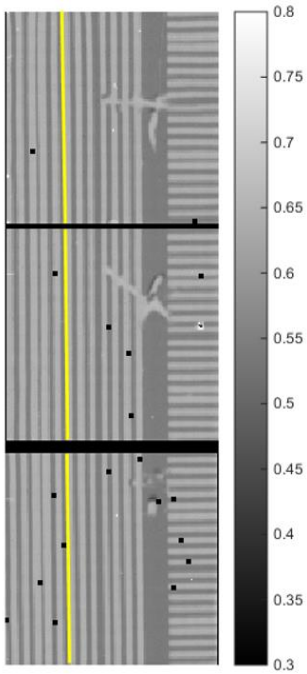

Figure 6.18 Alignment of the yellow lines across all chips are used to calculate the chip rotation.

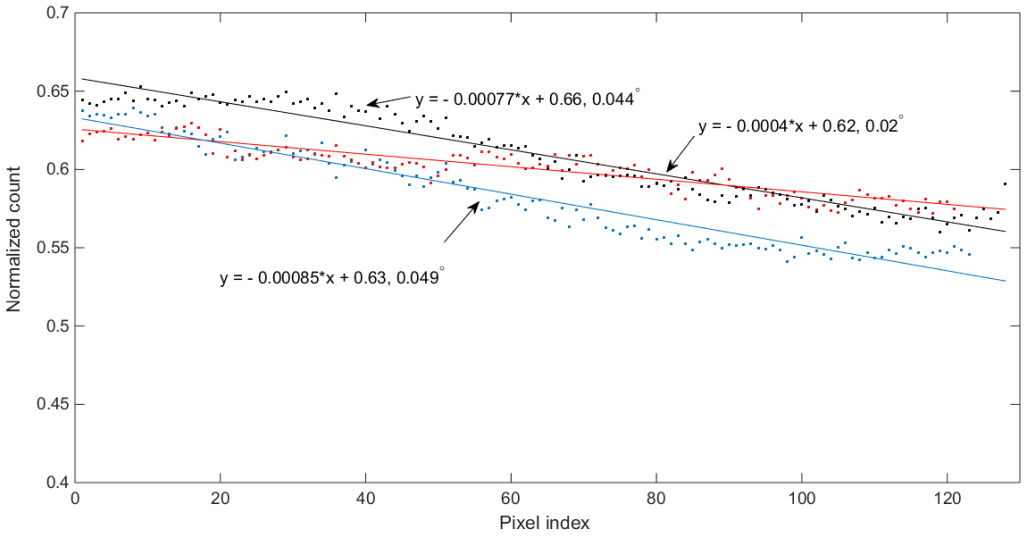

Figure 6.19 Fitted lines to the same column of projection image obtained from each chip.

6.4 Summary

- Geometric calibration of CT scanner is very important in order to achieve good image quality and spatial resolution. In this proposed method, all possible geometric parameters related to the x-ray source, object and camera were evaluated using line phantom.
- Seven geometrical parameters such as angular offset between the gantry and line phantom; sample x; radial offset of the x-ray tube and detector; camera and source axial and tangential offsets; chip x, chip y, and chip rotation were estimated using line phantom.
- Results show that the vertical position of the middle and bottom chips were off by 113 μm and 344 μm, respectively. Furthermore, there was no significant skewness for each chip. The tangential and axial offsets of all three chips (camera) need to be adjusted by 1.085 mm and 2.86 mm respectively
- The magnification varies from 4 % to 6 % with respect to the predicted value using the line phantom.
- A key feature of this method is to systematically measure the geometrical as well as speeding up the processing time.

7 Study of energy domain measurements in repeated scans

7.1 Introduction

This performance evaluation of the MARS scanner was carried out by measuring the relative count rate capability of the Medipix3RX chip in multiple counters and repeated scans. The Medipix3RX is the latest modification in the Medipix3 family of chips. It extends capabilities of the earlier detectors by including additional operating modes and configuration options. There is also an improved energy resolution and charge summing allocation algorithm that ensures the removal of the preferential summing effect. The pixels of traditional photon counting detectors, such as Medipix2, operate individually without using information from their neighbors. This is called single pixel mode (SPM). Traditional photon counting detectors suffer from charge sharing effect whereby charge dispersion during collection causes multiple pixels to simultaneously count a portion of the total input signal, thereby degrading spectroscopic performance. To mitigate this effect, Medipix3 includes pixel summing and arbitration circuitry that first sums the response from adjacent pixels and then allocates the result to the pixel contributing the largest share of the charge. This is called charge summing mode (CSM) [60, 61, 62].

Medipix3RX also provides multiple counters per pixel. In fine pitch mode, the $55\ \mu\text{m} \times 55\mu\text{m}$ pixels of the sensor and readout layers are arranged in a one-to-one mapping with two readout counters per detector pixel. In spectroscopic mode, four Medipix3 readout pixels are mapped to one $110\ \mu\text{m} \times 110\ \mu\text{m}$ sensor pixel thereby providing eight readout counters per pixel. Both modes are facilitated with (SPM) and (CSM). Each pixel cell of a Medipix3RX ASIC contains an analog section followed by the digital section. In the analog section of each pixel cell, it is possible to set the global energy threshold which is transferred via a (DAC) into a reference voltage. If the voltage pulse height of a collected charge in a pixel after amplification is higher compared to the energy threshold DACs, the counter in the digital part of the corresponding pixels gets incremented. The energy threshold DACs is adjusted to select the range of photon energies that will be counted. Counting photons with user adjustable energy threshold DACs allows the hybrid pixel detector to be used as an energy-resolving detector [1]. However, due to manufacturing variations, the counter thresholds vary from pixel to pixel and the response of the detector to a uniform flux is inconsistent across the chip.

Before acceptable images can be acquired it is necessary to equalize the counter thresholds so that each pixel is sensitive to pulses of the same minimum height. Random variations in the performance of pixel threshold detectors are a well-known characteristic of photon counting radiation detectors.

For this reason, it is normal to include adjustable corrections to each threshold detector in each pixel of these detectors [63]. One of the challenges in the development of photon counting spectral computed tomography is that the location of energy thresholds tends to vary among the detector elements. If not compensated for, this threshold variation leads to ring artifacts in the reconstructed images. Mats Pearson et al demonstrated a framework for evaluating threshold variation compensation methods in photon counting detector. They conclude that the effects of threshold variation can be countered to a large extent by the subtracting each detector element into the depth segments [43].

In this study, the relative count performance of different charge summing counter was evaluated with respect to the arbitration counter to investigate threshold drifting in repeated scans.

7.2 Materials and methods

In this section, the experimental setup for relative count measurement of the different counter with respect to the arbitration counter is discussed in details.

7.2.1 Measurement of count rate capability

To evaluate the count rate capability of different chips with respect to the arbitration counter, six back-to-back air scans were performed to collect raw images using MARS-15.

7.2.2 Experimental setup for count measurement

Six back-to-back air scans were performed in MARS-15 that utilized a polychromatic x-ray source (Model SB-120-350-GW-157, Source ray SB-125-350.SN:157) and a seven chip MARS camera (CZT-7x1-5.4-SN208-CZT:3RX-7chips) to evaluate count of each CSM mode with respect to the arbitration counter. The energy threshold was split into eight energy bins over the polychromatic x-ray spectrum (120 kVp). The chip was bonded to the CZT sensor layer and a pixel pitch of $110\ \mu m$ each with eight simultaneous threshold counters, four of which utilize real-time charge summing to significantly reduce the charge sharing between contiguous pixels. A protocol was created that included the tube voltage of 120 kVp, tube current of $25\ \mu$A, exposure time of 100 ms, and 1.96 mm aluminum filtration. Source to object distance (SOD) and Object to detector distance (ODD) were 280 mm and 200 mm respectively. Eight energy bins were set to 22.9 keV, 42.9 keV, 54.9 keV, 70 keV,74 keV, 77 keV,78 keV in spectroscopic mode. Before the actual acquisition of count rate, the x-ray

tube was activated for 20 seconds to warm up for ensuring the x-ray flux output was stable. Figure 7.1 shows the interior diagram of the MARS-15 during air scanning. The raw image of the seven chip MARS camera at different counters is presented in Figure 7.2.

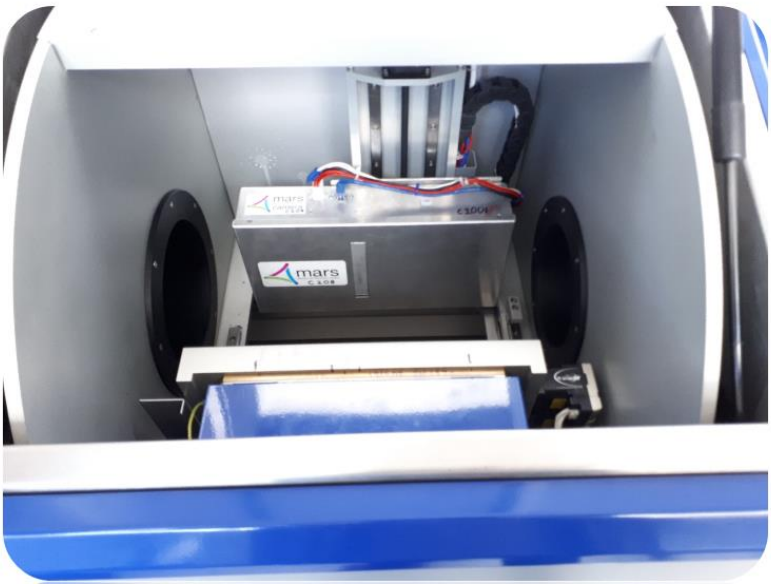

Figure 7.1 Interior diagram of MARS-15 during air scan.

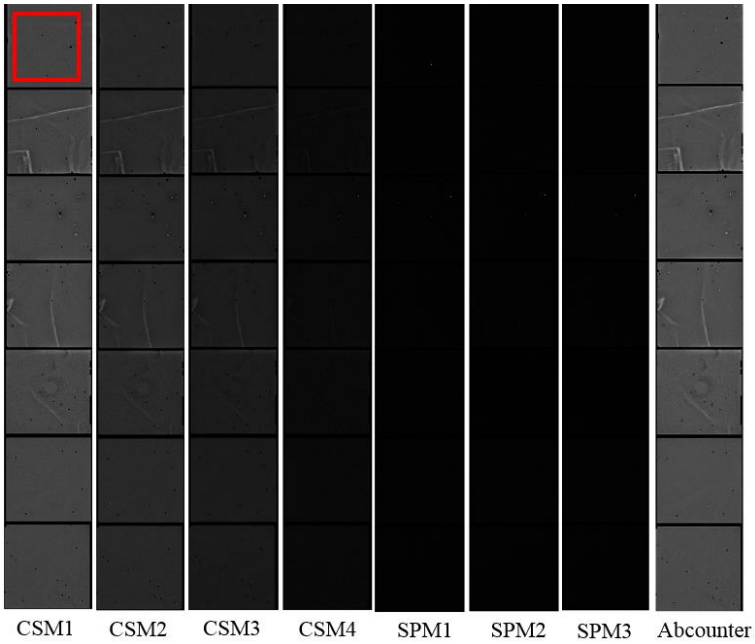

Figure 7.2 Reconstructed image of the seven chips MARS camera at different counters. The red rectangular region of interest (ROI) was chosen in each chip to calculate the count in each counter.

7.3 Results

The results of this experiment show the inter-scan count variation across the total number of the frame of the raw image. Figure 7.3 and Figure 7.4 shows the results of the relative count variation in different chips of two successive scans out of six back-to-back air scans. The relative count of each (CSM) counter was measured with respect to the arbitration counter. From both figures, it is clear that chip 4 shows the higher value of relative count in counter1, counter2, and counter3. The measured relative count rate was averaged over a selected region of interest of a chip with 110 pixels across the total number of the frame.

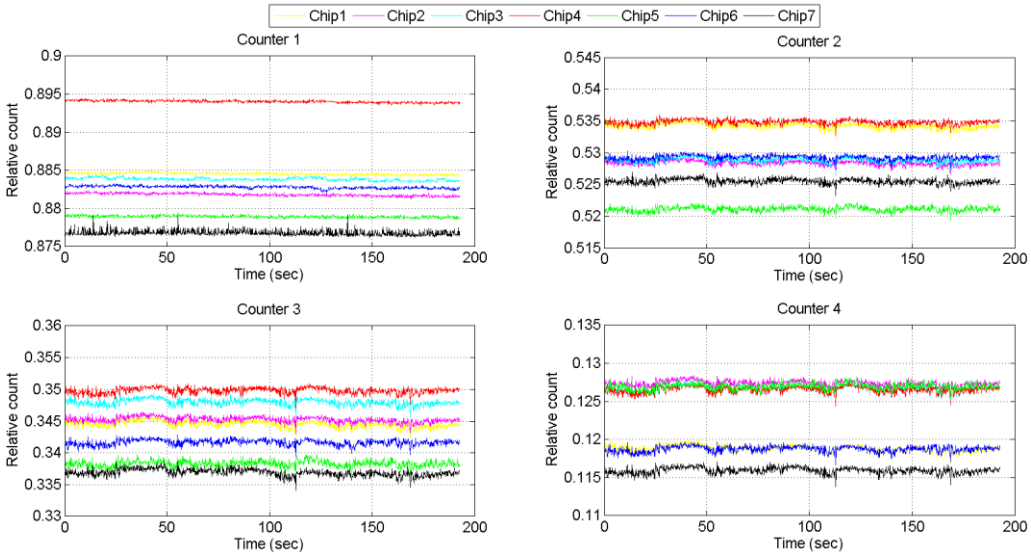

Figure 7.3 The relative count rate of the different (CSM) counters with respect to arbitration counter in each chip during the initial scan.

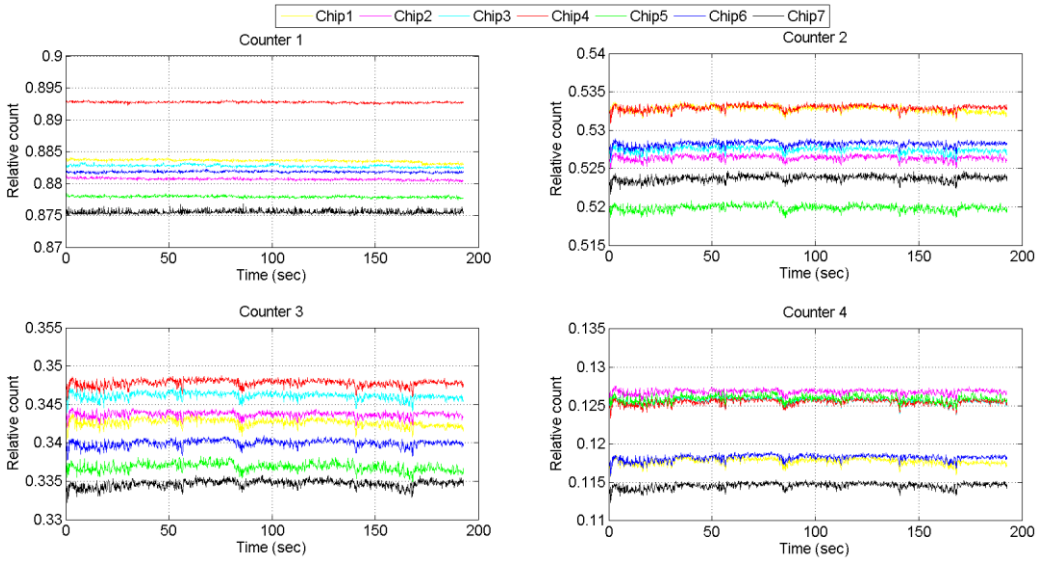

Figure 7.4 The relative count rate of the different (CSM) counters with respect to arbitration counter in each chip during the last scan.

Figure 7.5, Figure 7.6 and Figure 7.7 show the inter-scan variation of relative count in different counter at chip1, chip4 and chip7 in each scan. This results is shown to see the temporal count variation in different counters with respect to the arbitration counter. If the kVp is stable but the count of each CSM counter with respect to the arbitration counter changes over time then it indicates threshold drifting may exist over the entire x-ray spectrum. From these figures, it is clear that the relative count of each counter changes over the time during back-to-back scans and indicating the existence of threshold drifting. Figure 7.8 and Figure 7.9 show the histogram of the relative count in the top and bottom chip. All histograms were approximately normally distributed and tightly clustered about the mean and some of them are less skewed.

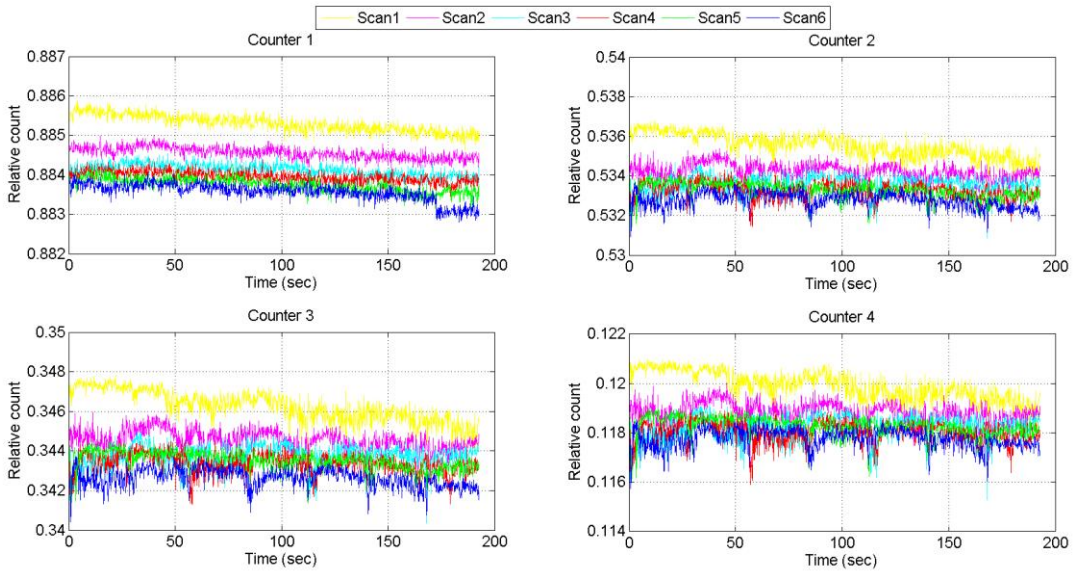

Figure 7.5 The relative count in each scan of the different counter at chip1.The variation in the ASIC temperature could be the possible reason for the variation in counts with time.

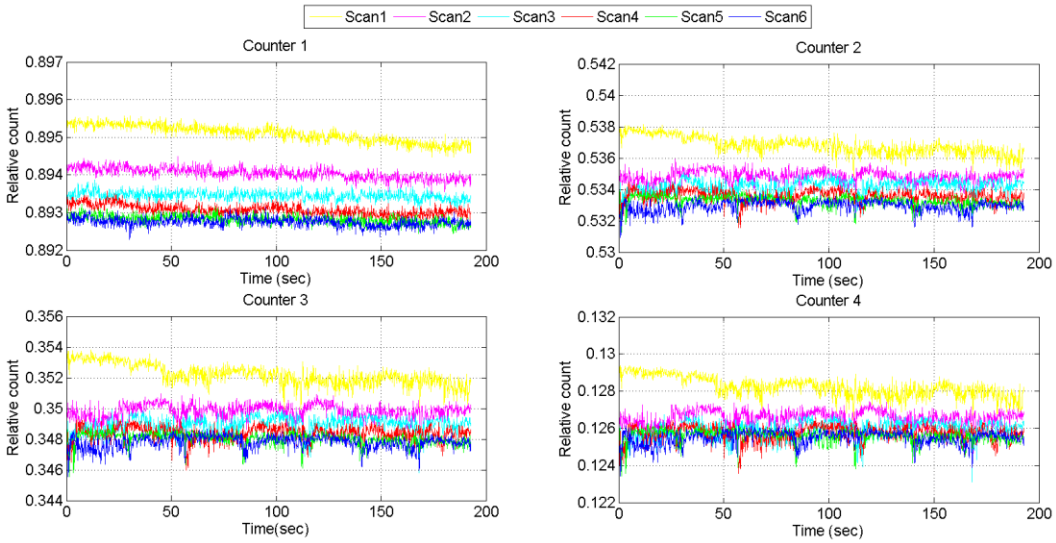

Figure 7.6 The relative count in each scan of the different counter at chip 4.The variation in the ASIC temperature could be the possible reason for the variation in counts with time.

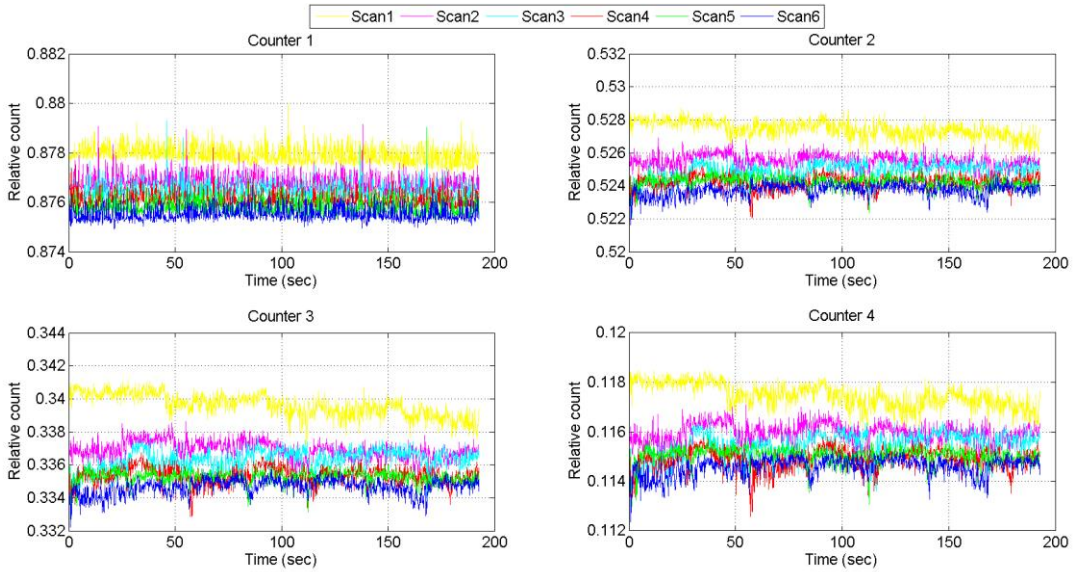

Figure 7.7 The relative count in each scan of the different counter at chip 7.The variation in the ASIC temperature could be the possible reason for the variation in counts with time.

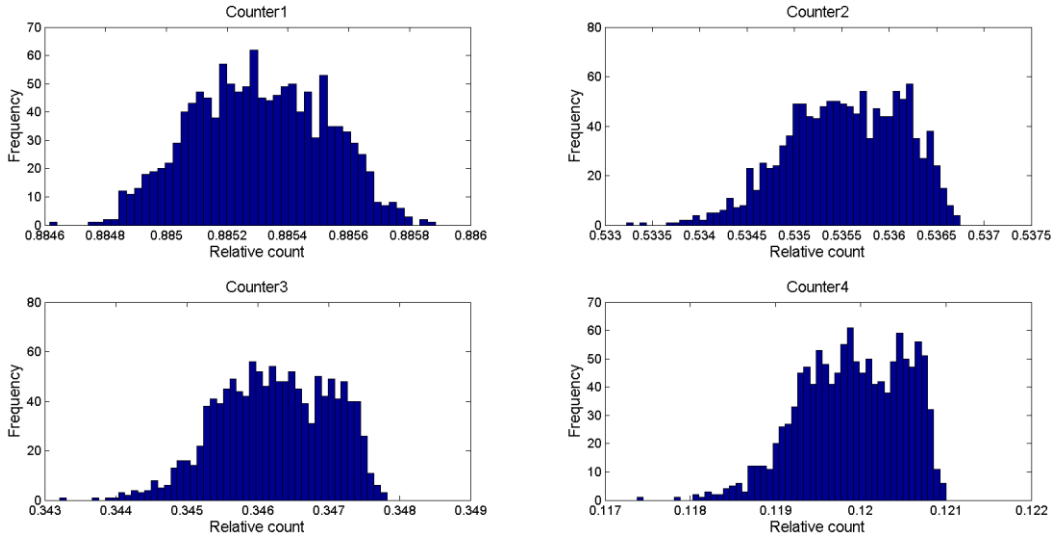

Figure 7.8 Rawimage histograms showing the distributions of relative counts in different charge summing counter in case of chip1.

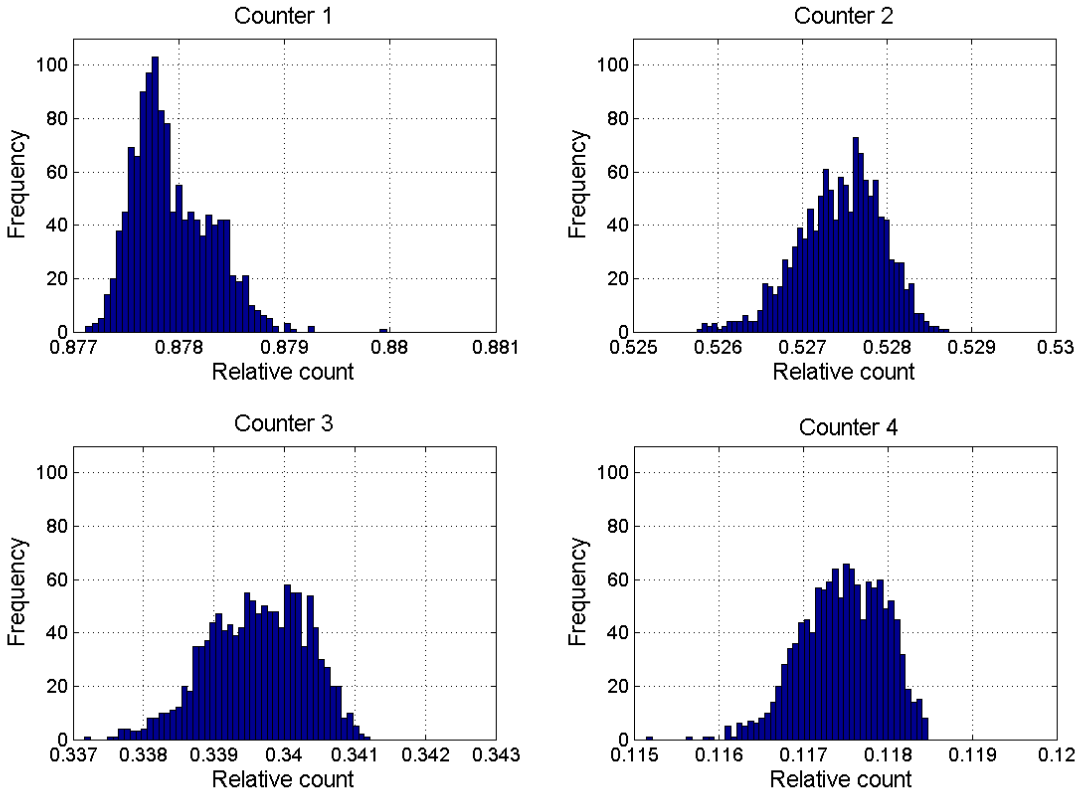

Figure 7.9 Rawimage histograms showing the distributions of relative counts in different charge summing counter in case of chip 7.

7.4 Discussion

This chapter investigate the count rate stability and uniformity of the MARS scanner. To do that, temporal stability of the Medipix3RX chip was investigated by measuring the count rate capability of each chip. The reason for doing this investigation was to see the temporal count variation in each chip and investigate count information in each energy counters. Initially, the relative counts over time of each chip and counter with respect to the arbitration counter was measured. It was noticed that there exist a significant fluctuation of the measured relative count in each chip at the different scan. The middle chip showed the higher count rate than other chips. The relative count rate in each counter is decreased by increasing the number of back-to-back air scans that indicates that temporal count variation exists in each chip in Figure 7.5 to Figure 7.7. The variation in the ASIC temperature during the first 7-10 minutes could be the possible reason for the variation in counts with time [64]. It is also expected that such temperature rises could change the energy threshold for each counter and which ultimately changes the energy response of the detector.

The relative count variation over time shows that the energy threshold is not stable and further work need to be done to eliminate this instability. It can be seen in Figure 7.3 and Figure 7.4 there is a high degree of corelation between ASIC and energy thresholds e.g. the count spikes occures simultaneously in each plot. Sources of variation consistent with this pattern include x-ray flux variation, bias voltage variation, and common mode electronic noise affecting the ASIC analogue circuits. The difference in relative counts between chips is greater than the temporal variation for a single chip. This suggests it may be possible to improve energy calibration using this type of measurements. This thesis is the first to report these measurements using a multi-sensor camera.

This study was performed at room temperature on same day with the same experimental parameters. Zuber et al [65] explained that the overall count rate fluctuation is a function of temperature instability of the spectral CT scanner. Therefore, the temperature fluctuations most probably induce a shift in the effective threshold position. This photon-counting detector is currently subject to various effects that limit its count rate capability. In general, all these effects arise either from the sensor or from the ASIC. One of those effects that rise from the sensor is polarization which is caused by insufficient charge transport properties of the sensor materials employed [53].

7.5 Summary

- The stability of the Medipix3RX photon counting detector in MARS scanner was evaluated by measuring the relative count rate with respect to the arbitration counter. It was assumed there might exist threshold drifting over the x-ray spectrum based upon this preliminary investigation.

- The count rate of each charge summing mode was evaluated across the total number of the frame with respect to the arbitration counter to investigate the threshold drifting over the entire x-ray spectrum.

- The relative count significantly decreases when increasing the number of air scans where indicates temporal instability in the MARS system.

- The effect of operating parameters of the x-ray tube such as: x-ray tube current, tube voltage, detector bias voltage, and different DACs along with ASIC temperature variation for the same time interval on the detector stability need to be investigated.

8 Discussion and Summary

The work presented in this thesis was carried out of a time when the development of MARS scanners was not yet complete and where many technical challenges had not been fully resolved. This work has investigated sources of error in images collected from MARS spectral CT scanners and has introduced several new calibration techniques to address these. Systematic procedures have been developed to characterize the variability of spectral CT images using different composite and single materials. Factors such as geometric misalignment, detector instability, temperature effects, inter-pixel variation, threshold drifting lead to the measurement variation. The optimal spectral imaging performance of the MARS scanner is achievable when its geometric parameters accurately incorporate into the image reconstruction software. Different coordinate and axis system were identified to characterize the geometric parameters of the MARS imaging system.

A spectral image library was developed to investigate the spatial image error due to the misalignment of different scanner components. The desire to interpret the effects of different types of error on image quality provided the motivation to create a library of spectral CT images containing artifacts induced by perturbing selected parameters of the scanner. The impact of setting inaccurate value of camera tangential offset (CTO) were perturbed with different values to characterize the spatial image error. The impact of wrong (CTO) value is edge blurring, not ring artifacts. Edge blurring was observed between the ranges of (CTO) value from -0.2 mm to +1 mm. An important concept was investigated throughout this thesis is that the information in the energy domain of spectral CT images is linked to the spatial domain. Consequently, if there are spatial artifacts in the reconstructed images, there will be a corresponding distortion in the energy information. The spatial information can be considered to be the total linear attenuation in a given voxel, which is the information provided by conventional CT scanner. The energy information is the linear attenuation for each of the available energy channels in each voxel. The extent and pattern of attenuation across these measurements can be used to identify specific materials and their concentration. The concept that spatial distortions will lead to severe distortion in the material information is effectively demonstrated is in Figure 5.23, where the material information is shown to be almost completely obliterated due to the geometric error. The image subtraction technique for evaluating the difference between normal reference images and those with the induced error was used in chapter 5. The line profile Figure 5.13 provides a useful graphical method to assess the severity of blurring.

Following the initial work in creating the spectral image library, Chapter 6 describes techniques developed for performing geometric calibration of several key scanner parameters. Of these parameters, the camera tangential offset and camera axial offset parameters, which describe the position of the detector within the gantry coordinate system, were associated with severe image artifacts when perturbed. This geometric calibration method was established to reduce the spatial image error. A custom build line phantom was

made to perform the geometric calibration on different MARS scanners. This phantom incorporates fiberglass with thin copper tracks coated with a few microns of gold. The copper tracks follow a special pattern that allows for measuring the geometrical offset with an accuracy of a few microns. It was found the magnification varied from 4 % to 6 % with respect to the predicted value using this method. The results also show that the vertical position of the middle and bottom chips were off by $113\ \mu$m and $344\ \mu$m, respectively. Furthermore, there was no significant skewness for each chip. The tangential and axial offsets of all three chips were adjusted by 1.085 mm and 2.86 mm, respectively. This method systematically measures the geometrical offset, as well as speeding up the processing time. The calibration methods for these have been used to calibrate several MARS scanner and found to be effective. The novel features of this geometric calibration method is to measure the all geometric parameters from the projection image at the accuracy of $\pm 10\ \mu$m level. Figure 5.3 shows a reconstructed image of a spectral phantom obtained from a poorly-calibrated MARS-CT with inaccurate tangential and axial offsets and how efficiently the blurred edges were removed from the reconstructed image after performing geometric calibration.

8.1 Final summary

- This thesis has investigated measurement errors in both spatial and energy dimensions of MARS spectral CT images.
- An important concept was investigated is that spatial information and energy information are intrinsically linked. Consequently, there are errors in the spatial domain there will be corresponding induced errors in the energy domain information. These will in turn affect the recovery of material information for scanned objects.
- During the course of this work, several new methods of calibration for MARS spectral CT scanners were developed and tested; in particular the geometric calibration of camera tangential and camera axial offset parameters.

8.2 Future work

In future work, spectral image quality can be investigated by scanning a larger object in terms of continuous development of different MARS scanners such as arm scanner, head and nick scanner. It will also observe how the size of reconstructed data related to the length of coverage, memory storage, voxel size, pitch, scan time and gantry rotation per second. Scanner calibration protocols and post-processing routines can be improved to minimize system and software related artifacts respectively. To quantify the uncertainty in MARS spectral imaging system forward and the inverse problem can be used to predict system response and parameter detection. This could be developed further to formulate a simple

quantitative metric for characterizing total error in spectral CT images. This is potentially very useful for automating the calibration process using machine learning techniques to find system parameters that minimize this total error.

9 Bibliography

[1] C. C. Onyema, An introductory manual on mars-ct imaging, MARS Bioimaging Ltd, 2016.

[2] S. G. B. OSullivan, "Plain radiograph/x-ray.," 2018. [Online]. Available: https://www.insideradiology.com.au/plain-radiograph-x-ray/ . [Accessed July 2018].

[3] "What are the technological advantages and limitations?," [Online]. Available: https://dir.nhlbi.nih.gov/labs/lce/cmri/mri-advantages-limitation.asp. [Accessed July 2018].

[4] R. A. Younis, Using MARS Spectral CT for Identifying Biomedical Nanoparticles, University of Canterbury, 2013.

[5] Symons, R, Reich, DS, Bagheri, M, Cork, TE, Krauss, B, Ulzheimer, S, Kappler, S, Bluemke, DA, Pourmorteza "A Photon-Counting Computed Tomography for Vascular Imaging of the Head and Neck: First In Vivo Human Results. *Invest Radiol*, 53, 3:135-142, 2018.

[6] "Preclinical Spectral CT System," [Online]. Available: https://www.marsbioimaging.com/mars/wp-content/uploads/2018/07/MARS_Electronic.pdf. [Accessed September 2019].

[7] "Father and son develop world -first scaner using cern tech," [Online]. Available: https://www.theengineer.co.uk/father-son-scanner-cern. [Accessed July 2018].

[8] "First human scanned with next-generation 3-d colour medical scanner," [Online]. Available: https://medicalxpress.com/news/2018-07-human-scanned-next-generation-d-colour.html. [Accessed July 2018].

[9] K. Taguchi, "Vision 20/20: Single photon counting x-ray detectors in medical imaging," *Medical Physics*, vol. 40, p. 10, 2013.

[10] B. J. Heismann, B. T. Schmidt and T. G. Flohr, Spectral computed tomography, SPIE, 2012.

[11] C. J. Bateman, Methods for Material Discrimination in MARS Multi-Energy CT, University of Otago, 2014.

[12] "Medipix," [Online]. Available: https://en.wikipedia.org/wiki/Medipix. [Accessed Friday September 2019].

[13] L. Ren, B. Zheng and H. Liu, "Tutorial on X-ray photon counting detector characterization," *J Xray Sci Technol,* vol. 26, p. 1–28, 2018.

[14] M. F. Walsh, Spectral Computed Tomography Development, University of Otago, 2014.

[15] J. T. Bushberg, J. A. Seibert, E. M. L. Jr and J. M. Boone, The Essential Physics of Medical Imaging, 4 ed., Lippincott Williams & Wilkins, 2011.

[16] E. J. Schioppa, The color of X-rays, Nikhef Amsterdam, 2014.

[17] P. Butler, "Using beer's law in mars scanners," University of Canterbury, 2015.

[18] "Mars small bore spectral scanner," [Online]. Available: https://www.marsbioimaging.com/mars/wp-content/uploads/2017/04/MARS_Small_Bore_Scanner.pdf. [Accessed Friday November 2018].

[19] A. Gongadze, A. Zhemchugov, G. Chelkov, D. Kozhevnikov, I. Potrap, M. Demichev, P. Smolyanskiy, R. Abramishvili, S. Kotov, A. Butler, P. Butler and S. Bell, "Alignment and resolution studies of a MARS CT scanner," *Physics of Particles and Nuclei Letters*, 2015.

[20] R. B. Zainon, Spectral Micro-CT Imaging of Ex Vivo Atherosclerotic Plaque, University of Canterbury, 2012.

[21] K. M and K. WA, "Presampling, algorithm factors, and and noise: considerations for CT in particular and for medical imaging in general," *Med Phys,* vol. 32, pp. 1321-34, 2005.

[22] O. M, W. S, K. M, M. T and N. K, "Imaging of small spherical structures in CT: simulation study using measured point spread function," *Med Biol Eng Comput,* vol. 46, pp. 273-282, 2008.

[23] Flohr, S. K, U. S, B. H, P. AN and M. CH, "Image reconstruction and image quality evaluation for a 64-slice CT scanner with z-flying focal spot," *Med Phys.,* vol. 32, p. 2536–2547, 2005 .

[24] Prevrhal, F. JC, S. JA and G. HK, "Accuracy of CT-based thickness measurement of thin structures: modeling of limited spatial resolution in all three dimensions," *Med Phys,* vol. 30, p. 1–8, 2003.

[25] E. Gonzalez, J.-y. Cui, G. Pratx and M. F. Bieniosek, "Point spread function for PET detectors based on the probability density function of the line segment," *IEEE,* 2011.

[26] I. H. H. SERIES, "Quality Assurance Programme for Computed Tomography: Diagnostic and Therapy Applications," IAEA, 2012.

[27] Nowik, B. R, P. G and F. A, "Quality control of CT systems by automated monitoring of key performance indicators: a two-year study," *J Appl Clin Med Phys,* vol. 16, 2015.

[28] A. Murphy, "Spatial resolution (CT)," [Online]. Available: https://radiopaedia.org/articles/spatial-resolution-ct. [Accessed September 2019].

[29] M. Moghiseh, R. Aamir, R. K. Panta, N. D. Ruiter, A. Chernoglazov, J. Healy, A. P. H. Butler and N. G. Anderson, "Discrimination of Multiple High-Z Materials by Multi- Energy Spectral CT– A Phantom Study," *JSM BiomedImaging Data Papers,* 2016.

[30] K. Rajendran, MARS Spectral CT Technology for Orthopaedic Applications, University of Otago, 2015.

[31] R. Aamir, A. Chernoglazov, C. J. Bateman, A. P. H. Butler, P. H. Butler, N. G. Anderson, S. T. Bell, R. K. Panta, J. L. Healy, J. L. Mohr, K. Rajendran, M. F. Walsh, N. d. Ruiter, S. P. Gieseg, T. Woodfield, P. F. Renaud, L. Brooke, S. Abdul-Majid and M. Clynek, "MARS spectral molecular imaging of lamb tissue: data collection and image analysis," *Journal,* vol. 9, 2014.

[32] "World’s first ever colour x-ray performed on a human," [Online]. Available: www.news18.com/news/lifestyle/health-and-fitness-worlds-first-ever-colour-x-ray-performed-on-a-human-1810229.html . [Accessed August 2018].

[33] "Nz scientists produce first 3d color x-ray on a human," [Online]. Available: https://www.gmanetwork.com/news/scitech/science/660256/nz-scientists-produce-first-3d-color-x-ray-on-a-human/story/ . [Accessed August 2018].

[34] "Christchurch father and son developing 3d scanner that could save millions," [Online]. Available: https://www.tvnz.co.nz/one-news/new-zealand/christchurch-father-and-son-developing-3d-scanner-could-save-millions . [Accessed July 2018].

[35] T. Kobayashi, K. Ogawa, F. Kaibuki and T. Yamakawa, "Accuracy of linear attenuation coefficients measured with a photon counting CT system," *Nuclear Science Symposium and Medical Imaging Conference (NSS/MIC),* 2012.

[36] C. TE and R. RK, "Quantification of multiple mixed contrast and tissue compositions using photon-counting spectral computed tomography," *J Med Imaging ,* 2019.

[37] A. Atharifard, J. Healy, B. Goulter, M. Ramyar, L. V. Broeke, M. Walsh, C. Onyema, R. Panta, R. Aamir, D. Smithies, R. Doesburg, M. Anjomrouz, D. Knight, A. Chernoglazov, H. Mandalika, S. Bell, C. Bateman, A. Butler and P. Butler, "Per-pixel energy calibration of photon counting detectors," *Journal of Instrumentation,* vol. 12, p. 03, 2017.

[38] J. Munro, "Using the MARS spectral CT scanner to image small samples," University of Canterbury, 2016.

[39] E. Tipton and J. Shuster, "A framework for the meta-analysis of BlandAltman studies based on a limits of agreement approach," *Stat Med,* vol. 36, p. 3621–3635, 2017.

[40] D. Giavarina, "Understanding bland altman analysis," *Biochemia medica,* p. 141–151, 2015.

[41] M. Bertero and M. Piana, "Inverse problems in biomedical imaging: Modeling and methods of solution," *Complex Systems in Biomedicine. Springer, Milano,* p. 1–33, 2006.

[42] "Tikhonov regularization.," [Online]. Available: https://en.wikipedia.org/wiki/Tikhonov regularization . [Accessed July 2018].

[43] M. Persson and H.Bornefalk, "A Framework for Evaluating Threshold Variation Compensation Methods in Photon Counting Spectral CT," *IEEE Trans Med Imaging,* vol. 31, pp. 1861--1874, 2012.

[44] P. He, B. Wei, W. Cong and G. Wang, "Optimization of K-edge imaging with spectral CT," *Med Phys,* vol. 39, p. 6572–6579, 2012.

[45] P. He, B. Wei, P. Feng, M. Chen and D. Mi, "Material discrimination based on K-edge characteristics," *Comput Math Methods Med,* 2013.

[46] M. Anjomrouz, Investigation of mars spectral ct: X-ray source and detector characterization, University of Otago, 2017.

[47] N. d. Ruiter, Algorithms to process data from the MARS molecular imaging system, University of Otago, 2014.

[48] R. Gordon, R. Bender and G. T. Herman, "Algebraic reconstruction techniques (ART) for three-dimensional electron microscopy and x-ray photography," *J. Theor. Biol,* vol. 29, p. 471–481, 1970.

[49] E. Searle, "Imaging small samples with mars spectral ct scanner," University of Canterbury, 2016.

[50] J. F. Barrett and N. Keat, "Artifacts in CT: recognition and avoidance," *Radiographics,* vol. 24, pp. 1679--1691, 2004.

[51] M. A. Bruno, E. A. Walker and H. H. Abujudeh, "Understanding and confronting our mistakes: the epidemiology of error in radiology and strategies," *Radiographics,* vol. 35, p. 1668–1676, Oct 2015.

[52] C. S. Lee, P. G. Nagy, S. J. Weaver and D. E. Newman Toker, "Cognitive and system factors contributing to diagnostic errors in radiology," *AJR Am J Roentgenol,* vol. 201, p. 611–617, 2013.

[53] R. K. Panta, Toward human MARS scanning: improving spectral performance for soft tissue imaging, University of Otago, 2015.

[54] V. Nguyen, "View-dependent geometric calibration for offset flat-panel cone beam computed tomography systems," *Optical Engineering,* 2016.

[55] Y. Cho, D. J. Moseley, J. H. Siewerdsen and D. A. Jaffray, "Accurate technique for complete geometric calibration of cone-beam computed tomography system," *Med Phys,* vol. 32, p. 968–983, 2005.

[56] X. Li, Z. Da and B. Liu, "A generic geometric calibration method for tomographic imaging systems with flat-panel detectors–a detailed implementation," *Med Phys,* vol. 37, p. 3844–3854, 2010.

[57] D. Panetta, N. Belcari, A. D. Guerra and S. Moehrs, "An optimizationbased method for geometrical calibration in cone-beam CT without dedicated phantoms," *Phys Med Biol,* vol. 53, p. 3841–3861, 2008.

[58] L. v. Smekal, M. Kachelriess, E. Stepina and W. A. Kalender, "Geometric misalignment and calibration in cone-beam tomography," *Med Phys,* vol. 31, p. 3242–3266, 2004.

[59] Y. Sun and Y. Hou, "A calibration method for misaligned scanner geometry in cone-beam computed tomography," *Elsevier, NDT&E International,* 2006.

[60] J. P. Ronaldson, Quantitative soft tissue imaging by spectral ct with medipix3, University of Otago, 2012.

[61] Ballabriga, G. Blaj and W. Wonga, "Characterization of the medipix3 pixel readout chip," *Journal of Instrumentation,* 2011.

[62] B. M. M. Chmeissania, "Performance limits of a single photon counting pixel system," *Elsvier,Nuclear Instruments and Methods in Physics Research,* 2001.

[63] R. M. Doesburg, The MARS Photon Processing Cameras for Spectral CT, University of Canterbury, 2012.

[64] M. Shamshad, Characterization of x-ray source and camera in MARS spectral system, University of Otago, 2016.

[65] M. Zuber, E. Hamann, R. Ballabriga, M. Campbell, M. Fiederle, T. Baumbach and T. Koenig, "An investigation into the temporal stability of CdTe-based photon counting

detectors during spectral micro-CT acquisitions," *Biomedical Physics & Engineering Express,* vol. 1, p. 025205, 2015.

[66] Anglen, J. and Marberry, K. and Gehrke, J."The clinical utility of duplicate readings for musculoskeletal radiographs," Orthopedics, vol. 20,1997.

[67] Rajendran, K, Löbker, C, Schon, BS, Bateman, CJ, Younis, RA, de Ruiter, NJ, Chernoglazov, AI, Ramyar, M, Hooper, GJ, Butler, AP, Woodfield, TB, Anderson, NG. " Quantitative imaging of excised osteoarthritic cartilage using spectral CT,". *Eur Radiol*, 27, 1:384-392, 2017.

[68] Anderson, N. G. and Butler, A. P. "Clinical applications of spectral molecular imaging: potential and challenge,s" *Contrast Media Mol Imaging*, vol.9,2014.

[69] Tipton and Shuster, "A framework for the meta-analysis of Bland-Altman studies based on a limits of agreement approach," *Stat Med,* vol. 36, pp. 3621-3635, 2017.

[70] G. D, "Understanding Bland Altman analysis," *Biochem Med,* pp. 141-51, 2015.

[71] J. Muders, Geometrical calibration and filter optimization for cone-beam, Heidelberg University, 2015.

[72] H. Meng and X. Yang, "On-line geometric calibration of cone-beam computed tomography for arbitrary imaging objects," *IEEE Trans. Med.*, 2013.